



TECHNISCHE
UNIVERSITÄT
WIEN
Vienna | Austria

Diploma Thesis

Cemented Carbides with γ/γ' Binder Microstructure

carried out for the purpose of obtaining the degree of Master of Science,

submitted at TU Wien, Faculty of Technical Chemistry,

by

Maximilian Wolf

Mat.Nr.: 1325781

Anton-Störck-Gasse 63/26, 1210 Wien

under the supervision of

Ao.Univ.Prof. Dipl.-Ing. Dr.techn. Christian Edtmaier

and

Assistant Prof. PhD MSc Raquel De Oro Calderon

Institute of Chemical Technologies and Analytics, E164

Vienna, November 2020



Die approbierte gedruckte Originalversion dieser Diplomarbeit ist an der TU Wien Bibliothek verfügbar.
The approved original version of this thesis is available in print at TU Wien Bibliothek.

Affidavit

I declare in lieu of oath, that I wrote this thesis and performed the associated research myself, using only literature cited in this volume. If text passages from sources are used literally, they are marked as such.

I confirm that this work is original and has not been submitted elsewhere for any examination, nor is it currently under consideration for a thesis elsewhere.

Signature:

Maximilian Wolf

Vienna, November 2020



Die approbierte gedruckte Originalversion dieser Diplomarbeit ist an der TU Wien Bibliothek verfügbar.
The approved original version of this thesis is available in print at TU Wien Bibliothek.

Table of Contents

Table of Contents	I
Abstract.....	IV
Kurzfassung.....	V
1 Introduction.....	1
1.1 Motivation	1
1.2 Common Phases	2
1.2.1 Superalloys.....	2
1.2.2 Influence of Carbon	4
1.2.3 Cemented Carbides	4
1.3 CALPHAD Approach.....	6
1.3.1 Literature Data	6
1.3.2 Thermodynamic Modelling.....	7
1.3.3 Modelled Phases	10
2 Experimental	11
2.1 Material and Methods	11
2.1.1 Powder Mixtures	11
2.1.2 Heating Furnaces.....	11
2.1.3 Metallographic Preparation.....	13
2.1.4 Scanning Electron Microscopy.....	13
2.1.5 Combustion Carbon Analysis	15
2.1.6 Difference Thermal Analysis	15
2.1.7 Thermo-Calc Calculations	16
2.2 Superalloys	17

2.2.1	Stability of γ' precipitation.....	17
2.2.2	Variation of Nickel	18
2.2.3	Preparation Details.....	18
2.2.4	Cold Boat and Hukin Crucible	20
2.3	Influence of Carbon.....	21
2.4	Cemented Carbides via Infiltration	22
2.5	Cemented Carbides via DTA	22
2.6	Ab Initio Calculations	24
3	Results and Discussion.....	27
3.1	Superalloys.....	27
3.1.1	Stability of γ' precipitation.....	27
3.1.2	Variation of Nickel	33
3.1.3	Cold Boat and Hukin Crucible	37
3.2	Influence of Carbon.....	39
3.3	Cemented Carbides via Infiltration	46
3.4	Cemented Carbides via DTA	54
3.4.1	Solidus Temperature	54
3.4.2	Analysis of Phases.....	57
3.4.3	Binder Composition Analysis	60
3.5	Ab Initio Calculations	63
3.5.1	Reference State Elements	63
3.5.2	L1 ₂ structures.....	63
3.5.3	E2 ₁ structures	65
3.5.4	Comparison	68

4	Summary	70
5	Conclusions	76
6	Appendix	78
6.1	Cemented Carbides via DTA	78
6.1.1	Weighed-In Compositions.....	78
6.1.2	DTA Measurements	79
6.1.3	Microstructure	87
6.2	Thermo-Calc Macros.....	94
6.2.1	γ/γ' Solvus Temperature	94
6.2.2	Phase Diagram using TCFE9 and Zhu14 Databases	95
6.2.3	Solidus Temperature VS Aluminum Concentration.....	95
6.2.4	Calculation of a Ternary Diagram	96
6.2.5	Draw a Ternary Diagram with Experimental Data.....	96
6.3	References.....	98

Abstract

Modifications of the binder phase (γ) of cemented carbides potentially increases the hardness and wear resistance of the whole material. (Partially) coherent precipitations with $L1_2$ structure (γ') promise these improved properties without sacrificing tensile strength or toughness [1]. γ' is a metastable phase in the aluminum-cobalt-tungsten ternary system in the form of $Co_3(Al,W)$ which is stabilized by the substitution of cobalt with nickel [2].

A preparation method for cemented carbides with γ/γ' binder microstructure was developed in this work and the phase equilibria in the composite material were investigated. Infiltration of preliminary produced cobalt-base and cobalt-nickel-base superalloys into tungsten carbide powder yielded the anticipated microstructure.

It was shown that nickel stabilizes the γ' phase in superalloys as well as in cemented carbides. Carbon leads to the formation of an additional phase with $E2_1$ structure (κ). DTA measurements of cemented carbides with different aluminum-cobalt-nickel mixtures as binder gave an overview of the compositional influence. The aluminum-carbon-cobalt-nickel-tungsten quinary system was thermodynamically modelled and the relevant literature data was collected. Enthalpies of formation for compounds with $L1_2$ and $E2_1$ structure were calculated using ab initio methods and discussed afterward.

Kurzfassung

Die Modifikation der Binderphase (γ) von Hartmetall kann zu einer Steigerung der Härte und Verschleißbeständigkeit des gesamten Werkstoffs führen. (Teil-)kohärente Ausscheidungen mit dem Strukturtyp $L1_2$ (γ') versprechen diese Verbesserung ohne eine Abnahme der Festigkeit und Zähigkeit [1]. Im System Aluminium-Cobalt-Wolfram ist γ' eine metastabile, intermetallische Phase der Form $Co_3(Al,W)$, deren Stabilitätsbereich durch die Substitution von Cobalt mit Nickel erweitert werden kann [2].

In dieser Arbeit wurden eine Methode zur Herstellung von Hartmetall mit γ/γ' Binder-mikrostruktur entwickelt und die Phasengleichgewichte in diesem Verbundwerkstoff untersucht. Durch Infiltration von Cobalt-Basis- und Cobalt/Nickel-Basis-Superlegierungen in Wolframkarbid-Pulverschüttungen konnte das gewünschte Gefüge reproduzierbar hergestellt werden.

Es wurde gezeigt, dass Nickel die γ' -Phase in den Superlegierungen und im Hartmetall stabilisieren kann. Kohlenstoff führt zur Bildung einer weiteren Phase mit dem Strukturtyp $E2_1$ (κ). DTA-Messungen von Hartmetallen mit unterschiedlichen Aluminium-Cobalt-Nickel-Mischungen als Binder gaben einen guten Überblick über den Einfluss der Zusammensetzung. Das System Aluminium-Kohlenstoff-Cobalt-Nickel-Wolfram wurde thermodynamisch modelliert mit Daten aus der Literatur verglichen. Für diese Modellierung relevante Bildungsenthalpien wurden durch Ab Initio Methoden berechnet und anschließend diskutiert.



Die approbierte gedruckte Originalversion dieser Diplomarbeit ist an der TU Wien Bibliothek verfügbar.
The approved original version of this thesis is available in print at TU Wien Bibliothek.

1 Introduction

1.1 Motivation

Cemented carbide is known for about 100 years and used in a broad field of industrial applications, especially as cutting tool material [3]. It is a composite usually consisting of a metal carbide as hard phase, e.g. tungsten or titanium carbide, and a metal binder phase, e.g. cobalt, nickel, iron, or alloys of these elements. This combination leads to materials with excellent hardness and toughness but with a higher fracture resistance than ceramics [4]. The microstructure highly influences the properties of cemented carbides and there are several approaches for modifications [5]. One way is toughening the binder phase through γ' precipitation hardening [6, 7].

Superalloys with γ/γ' microstructure are commonly used in gas turbines because of their unprecedented high temperature toughness [8]. The (partially) coherent γ' precipitations with $L1_2$ crystal structure are usually found in the aluminum-nickel system as Ni_3Al intermetallic phase. The aluminum-cobalt system does not give rise to an isotype of this compound but a metastable compound $Co_3(Al,W)$ can be found when tungsten is added [9]. Further addition of nickel stabilizes the γ' phase at room temperature and elevates its solvus temperature [2]. Carbon also stabilizes precipitates in the aluminum-cobalt-tungsten system, but the formed compound is Co_3AlC which has the $E2_1$ crystal structure and is denoted as κ phase [10].

Therefore, the aluminum-carbon-cobalt-nickel-tungsten system is of high interest for theoretical and experimental investigation in this work. Superalloys are produced and analyzed in regard to their preparational and compositional parameters. The influence of carbon addition to this system is studied. Cemented carbides are produced by infiltration of different superalloys and the binder regions are searched for γ/γ' microstructure. The influence of aluminum addition to cemented carbides with cobalt-nickel binder is investigated through difference thermal analysis. The precipitation phases γ' and κ are studied by means of ab initio calculations.

1.2 Common Phases

A complete list of all possible phases of the aluminum-carbon-cobalt-nickel-tungsten system is given down below in chapter 1.3.2. But the phases which are most likely to form, considering the composition ranges, will be discussed here in more detail.

1.2.1 Superalloys

The investigated superalloys without carbon are covered almost entirely by the works of Lass et. al. [11] and Shinagawa et. al. [2] where the phase equilibria and microstructures of cobalt-based and cobalt-nickel-based alloys with aluminum concentrations from 8.25 to 17.5 at% and tungsten concentrations from 2.5 to 15 at% are studied. Additionally, Zhu et. al. [12] thermodynamically assessed the quaternary system in the cobalt-rich region which also fits the experimentally prepared superalloys from this work. The stable phases which were found in this literature are the following:

Above the allotropic phase transition of hcp cobalt, a solid solution of cobalt and nickel with fcc structure is formed. This phase is usually denoted as γ and dissolves over 15 at% aluminum [13] and up to 18 at% tungsten [14] in ternary alloys. This can also be reasoned from the binary phase diagrams in Figure 1 where quite high aluminum and tungsten contents are predicted to dissolve at higher temperatures in cobalt and nickel. The solubility of these elements is heavily reduced in cobalt at lower temperatures which might happen because the hcp allotrope becomes more and more stable.

The big difference between the aluminum-cobalt and aluminum-nickel systems is that γ' is only formed in the latter one. Ni_3Al is an ordered form of the fcc crystal structure with aluminum at the corners and nickel at the face centers of the cube. The solubility of cobalt in γ' is up to 50 at% in the ternary aluminum-cobalt-nickel system at 900 °C [15] and the phase becomes stable at even higher cobalt concentrations when tungsten is added [2].

At higher aluminum concentrations, B2 phase – sometimes denoted as β – is formed which is an ordered form of the bcc crystal structure with aluminum in the body center and cobalt (AlCo) or nickel (AlNi) at the corners [16, 17]. It is easy to assume that AlCo

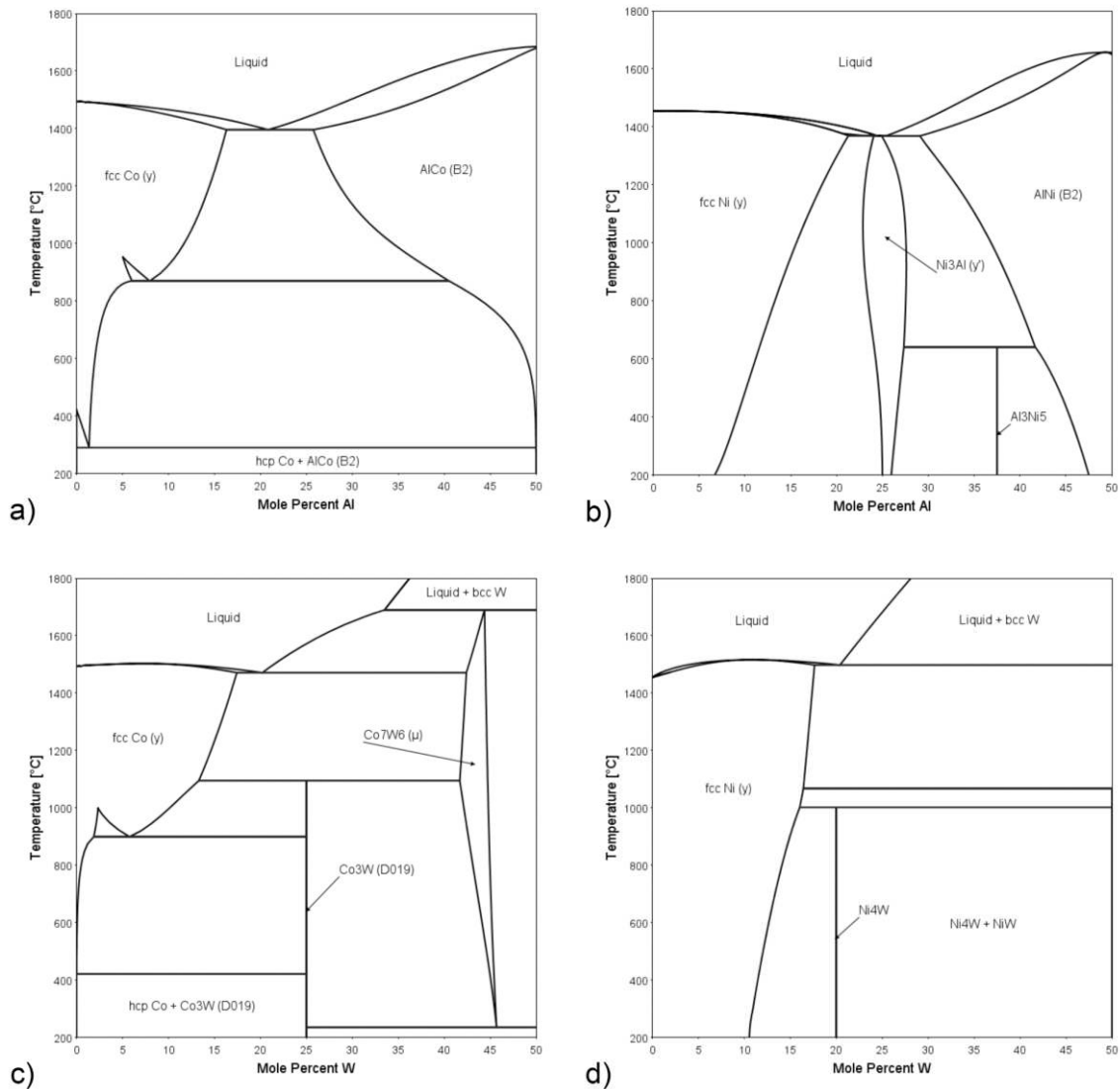


Figure 1: Calculated phase diagrams of a) cobalt-aluminum, b) nickel-aluminum, c) cobalt-tungsten, and d) nickel-tungsten binary systems. Only the cobalt and nickel rich sections are shown. The calculations were carried out using Thermo-Calc (see chapter 2.1.7) and the parameters of the binary systems (see chapter 1.3.1) in individually written databases.

and AlNi form a continuous phase field in the ternary aluminum-cobalt-nickel system because the phases have the same crystal structure and a similar composition range. The calculated ternary phase diagrams from Wang et. al. [15] and Zhu et. al. [12] confirm this assumption. In the latter work it is also shown that AlCo has high tungsten solubilities of over 10 at% but AlNi does not dissolve even 1 at% tungsten. This coincides with the findings from Shinagawa et. al. where B2 (β) phase is only found in cobalt rich alloys [2]. Cobalt forms two intermetallic phases with tungsten in the composition range from 0 to 50 at% tungsten. Both, Co_3W with D0₁₉ crystal structure and Co_7W_6 with D8₅ crystal

structure, show aluminum solubilities of 2.5 to 5 at% [11, 12]. But they are also found in nickel containing alloys where DO_{19} (Co_3W) and μ (Co_7W_6) form below and above 50 at% nickel, respectively [2]. Al_3Ni_5 , Ni_4W and NiW do not show up in the samples or calculations in [2] and [12] which can be reasoned from the fact that only cobalt rich alloys were investigated. Also, these phases might have very low cobalt solubilities.

The binary phases of the aluminum-tungsten system do not have to be considered because it is not expected that high amounts of these elements react with each other and they are not found in any of the higher order systems of the literature data.

1.2.2 Influence of Carbon

Additions of carbon to cobalt-based superalloys have already been investigated by Freund et. al. [10] and thermodynamic assessments of the aluminum-carbon-cobalt ternary and the aluminum-carbon-cobalt-nickel quaternary systems were carried out by Zheng et. al. [18] and Ohtani et. al. [19], respectively.

Cobalt and nickel do not form any carbides [20] and Al_4C_3 from the aluminum-carbon binary system [21] is not expected to be found for the same reasons as for the aluminum-tungsten compounds. The only additional phase which must be considered is κ which corresponds to Co_3AlC or Ni_3AlC . This phase has $E2_1$ crystal structure and can be constructed from $L1_2$ Co_3Al or Ni_3Al by placing a carbon atom into the body center. It is found to be stable in the aluminum-carbon-cobalt ternary system but has a quite narrow homogeneity range [18]. Experimental data for the Ni_3AlC phase is very scarce. Ohtani et. al. theoretically determined phase equilibria for the aluminum-carbon-nickel ternary system but did not calculate any phase diagrams nor discussed the results thoroughly. But from the ab initio calculated formation enthalpies one could reason that κ is not formed since γ' is more stable [19]. Also, Ni_3Al seems to dissolve high amounts of carbon with up to 10 at% [22, 23].

1.2.3 Cemented Carbides

Tungsten readily forms carbides which are very stable and only dissolve marginally in cobalt or nickel even at high temperatures. Most of the work for the thermodynamic

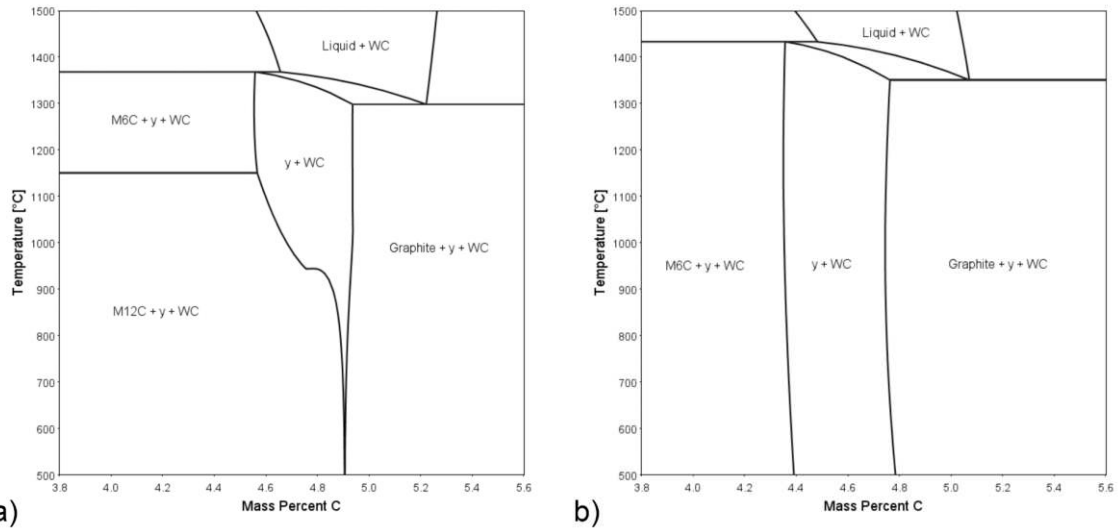


Figure 2: Calculated phase diagrams of tungsten carbide with 20 wt% a) cobalt and b) nickel. Only the important section with the carbon window is shown. The calculations were carried out using Thermo-Calc with TCFE9 database (see chapter 2.1.7).

description of cemented carbides with binder consisting of cobalt and nickel was done by Guillermet [24, 25] but has been updated many times with one recent assessment from Zhou et. al. [26].

The calculated phase diagrams of cemented carbides with 20 wt% cobalt or nickel are shown in Figure 2. The carbon window where only two phases, i.e. γ and WC, are stable is usually the targeted region when cemented carbides are produced. Excess carbon results in the formation of graphite and too little carbon leads to decomposition of WC to η carbides, which are $M_{12}C$ and M_6C . The gradual substitution of cobalt with nickel elevates the solidus temperature, widens the carbon window at lower temperatures, and causes the $M_{12}C$ phase to vanish [26]. This corresponds to a continuous transition between the phase diagrams in Figure 2.

Experimental and theoretical literature data on the effect of aluminum addition to these cemented carbides is very scarce. Wang et. al. investigated the aluminum-carbon-nickel-tungsten quaternary system but did not consider aluminum solubility in any of the carbides [22].

1.3 CALPHAD Approach

The method for CALculation of PHAse Diagrams was introduced in 1970 and provides a convenient way of predicting thermodynamic properties of multi-component systems [27, 28]. The basic approach is that the property of a system in thermodynamic equilibrium is defined by the sum of this property in the individual phases. Conventionally a minimum of Gibb's energy is approximated because most experiments are carried out with no mass change at known temperature and pressure. Also, since the system is in thermodynamic equilibrium, all other thermochemical properties can be calculated from it [29]. A simple but physically correct model is defined for each phase and deviations from it are corrected by excess energy power series. The parameters of these terms are optimized using experimental data [30].

1.3.1 Literature Data

A multi-component database for thermodynamic calculations consists of parameters from assessments of all included elements. The unary parameters are usually taken from the SGTE data where the pure elements are described in the liquid phase and all common crystal structures [31].

The most important parameters are found in the binary assessments since the majority of intermetallic phases is diatomic. For the five elements of interest in this work, there are ten binary permutations which is the number of thermodynamic assessments to consider. The aluminum-carbon system is assessed in [21] and updated in [32] and [18], the aluminum-cobalt system is taken from [16] with some updated parameters from [18] and [33] the aluminum-nickel system is assessed in [17] and [34], the most recent parameters for the aluminum-tungsten system are from [33], the carbon-cobalt system is described in [24] but the κ phase is added in [18], the carbon-nickel system is taken from [25] with updates from [35], the carbon-tungsten system is assessed in [36], the cobalt-nickel system is taken from [37] but the description of metastable phases is from [13], the cobalt-tungsten system is described in [24] and updated in [33] and [38], and the nickel-tungsten system is taken from [39].

Parameters for the solubilities of elements in binary phases and, of course, compounds which consist of three elements are found in ternary assessments. Often, when phases are metastable in the binary system and become stable in the ternary, the parameters are added there. Nine of the ten possible ternary permutations are available as assessments, only aluminum-carbon-tungsten is missing but this system is already well described by the underlying binary systems. The aluminum-carbon-cobalt system was very recently assessed in [18], the parameters of aluminum-carbon-nickel are taken from [22] but κ is only described in [19], the aluminum-cobalt-nickel system is taken from [13] but has also been assessed in [15], the parameters of the aluminum-cobalt-tungsten system are found in [33], aluminum-nickel-tungsten is assessed in [40] but some parameters are missing, carbon-cobalt-nickel and carbon-cobalt-tungsten are taken from [25] but the latter one is updated in [38], carbon-nickel-tungsten is assessed in [22], the cobalt-nickel-tungsten system is also described in [25] with some updated parameters in [26].

Quaternary parameters are quite uncommon because these systems should be described using binary and ternary parameters as much as possible [30]. They are only found for the carbon-cobalt-nickel-tungsten system which was assessed in [26]. The problem with higher order systems from ternary upwards is that many of them are overfitted and cannot easily be combined to a multi-component database without re-assessment. This is especially true for the quaternary system of aluminum-cobalt-nickel-tungsten from [12] which gives very good results for the special case of cobalt-rich alloys but cannot be combined with other systems since the underlying binary and ternary systems are massively modified to fit the experimental data.

1.3.2 Thermodynamic Modelling

The molar Gibb's energy of stoichiometric phases is simply modelled by a temperature dependent power series in the form of

$$G_m - \sum_i b_i H_i^{SER} = a_0 + a_1 T + a_2 T \ln(T) + a_3 T^2 + a_4 T^{-1} + a_5 T^3 + \dots$$

where b_i is the stoichiometric factor of element i and H_i^{SER} is the enthalpy of formation of the element i in its reference state at 298.15 K, e.g. cobalt in the hcp structure. The

coefficients a_i are the parameters which are to be optimized but they can also be related to experimental determined thermochemical data, i.e. the temperature dependency of molar enthalpy, entropy, and heat-capacity.

The substitutional-regular-solution model is used for the liquid phase and solid phases where the elements occupy any crystallographic site with the same probability, i.e. they are completely disordered. The molar Gibb's energy is given by

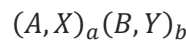
$$G_m = \sum_i x_i G_i - TS_m^{cnf} + G_m^E$$

where x_i is the molar fraction of element i and G_i is the Gibb's energy of this element in the respective phase which would be modeled by a temperature dependent power series from above. This sum is also known as the molar Gibb's energy surface of reference G_m^{srf} . S_m^{cnf} is the configurational entropy of an ideal mixture of the elements and G_m^E is the molar excess energy term. This last term is typically modelled with interaction parameters L which correspond to the reactions of the elements with each other as

$$G_m^E = \sum_{i \neq j} x_i x_j L_{ij} + \sum_{i \neq j \neq k} x_i x_j x_k L_{ijk} + \sum_{i \neq j \neq k \neq l} x_i x_j x_k x_l L_{ijkl}$$

The binary and ternary interaction parameters are further modelled by compositional dependent polynomials. Quaternary interaction parameters are quite uncommon and higher order parameters should be omitted.

When the elements undergo ordering, i.e. preferably occupy specific crystallographic sites, a sublattice model must be used. This applies to phases which are stable at composition ranges outside their stoichiometric composition. A Wagner-Schottky defect model can be used for a phase with two sublattices, i.e.



where A and B are the ideal constituents, X and Y are the defects, and a and b are the stoichiometric ratios of each sublattice. The defects can be anti-site atoms, vacancies, interstitials, or a mixture of all of them. The molar Gibb's energy of this phase would be expressed in the same way as the substitutional-regular-solution model, but the three

terms must be extended using the site fractions y_i^α and y_i^β which are the concentrations of each element i in the sublattice α and β , respectively. The Gibb's energy surface of reference is then expressed as

$$G_m^{srf} = y_A^\alpha y_B^\beta G_{A:B} + y_A^\alpha y_Y^\beta G_{A:Y} + y_X^\alpha y_B^\beta G_{X:B} + y_X^\alpha y_Y^\beta G_{X:Y}$$

where $G_{i:j}$ is the Gibb's energy of formation of a (theoretical) compound $i_a j_b$, which is also known as endmember. These parameters are very important for the correct description of a phase in the sublattice model because they define the range of stability which can hardly be altered by using interaction parameters. If the endmembers are unknown, they have to be guessed or might be determined by ab initio calculations (see chapter 2.6). The configurational entropy and excess energy terms are analogous extended using the site fractions. The Wagner-Schottky defect model could be further simplified when one considers the small anti-site fractions but is generally applicable in this form. Phases with more than three sublattices need very large numbers of parameters which often have to be reduced using crystallographic information.

Phases which undergo a second-order transition, e.g. γ to γ' or bcc to B2, must be modeled using the same Gibb's energy expression. This is achieved by a partitioning of the contributions from the disordered and ordered state of the phase in the form of

$$G_m = G^{dis}(x_i) + \Delta G^{ord}(y_i) - \Delta G^{ord}(y_i = x_i)$$

where $G^{dis}(x_i)$ is the Gibb's energy of the phase in the disordered state. $\Delta G^{ord}(y_i)$ is the energy difference which is obtained if the phase is in the ordered crystal structure with the elements occupying the sites in an ordered state and $\Delta G^{ord}(y_i = x_i)$ is this energy difference but with the elements occupying the sites randomly, i.e. disordered. If there is no stabilizing effect through the ordering, the last two terms cancel out and the phase stays in the disordered state.

The above described models and terminologies are a simplified summary of the relevant sections of the book *Computational thermodynamics: the Calphad method* [30].

1.3.3 Modelled Phases

Table 1: Phases in the aluminum-carbon-cobalt-nickel-tungsten system which were collected from the literature sources which are mentioned in chapter 1.3.1. The lattices are omitted for stoichiometric phases (SP). The other models are substitutional-regular-solution model (SRS), sublattice model (SL) and interstitial solution model (IS), which is a special case of the Wagner-Schottky model (WS).

Phase	Lattice	Model	Ref.
Liquid	(Al,C,Co,Ni,W)	SRS	-
γ	(Al,Co,Ni,W)(C,Va)	IS	-
γ'	(Al,Co,Ni,W) _{0.75} (Al,Co,Ni,W) _{0.25} (C,Va)	2SL + IS, ordered γ	-
κ	(Al,Co,Ni) _{0.75} (Al,Co,Ni) _{0.25} (C,Va)	2SL + IS	-
bcc	(Al,Co,Ni,W,Va) ₁ (C,Va) ₃	IS	-
B2	(Al,Co,Ni,W,Va) _{0.5} (Al,Co,Ni,W,Va) _{0.5} (C,Va) ₃	2SL + IS, ordered bcc	-
hcp	(Al,Co,Ni,W,Va) ₁ (C,Va) _{0.5}	IS	-
μ	(Al,Co,Ni) ₇ W ₂ (Co,Ni,W) ₄	3SL	-
D0 ₁₉	(Co,Ni) ₃ (Al,W)	2SL	-
M ₆ C	(Co,Ni) ₂ W ₂ (Co,Ni,W) ₂ C	4SL	-
M ₁₂ C	(Co,Ni) ₆ W ₆ C	4SL	-
Al ₄ C ₃	-	SP	[21]
Al ₃ Co	-	SP	
Al ₅ Co ₂	-	SP	
Al ₉ Co ₂	-	SP	[16]
oAl ₁₃ Co ₄	-	SP	
yAl ₁₃ Co ₄	-	SP	
mAl ₁₃ Co ₄	-	SP	
Al ₃ Ni	-	SP	
Al ₃ Ni ₂	(Al) ₃ (Al,Ni) ₂ (Ni,Va)	2SL + WS	[17]
Al ₃ Ni ₅	-	SP	
Al ₂ W	-	SP	
Al ₄ W	-	SP	
Al ₅ W	-	SP	[33]
Al ₇ W ₃	-	SP	
Al ₁₂ W	-	SP	
Al ₇₇ W ₂₃	-	SP	
NiW	-	SP	
Ni ₄ W	-	SP	[39]
NiW ₂	-	SP	
WC	-	SP	[36]

2 Experimental

2.1 Material and Methods

2.1.1 Powder Mixtures

The powders used for all experiments are specified in Table 2 and were weighed using a balance with readability, repeatability and linearity of 0.1, 0.1 and 0.2 mg respectively. The weighing error was always below 1 % from target weight but exact measurements were not recorded since compositional accuracy of 0.1 wt% was sufficient. After weighing the powder mixtures into PP bottles, homogenization was carried out in a 3D shaker mixer (TURBULA®, Willy A. Bachofen AG) for at least 1 h.

Table 2: Specification of powders which were used for all experiments.

Compound	Purity	Particle size	Supplier	Package Label
C	> 99 %	unknown	unknown	Graphit
Al	99.7 %	< 400 μm	MEPURA	Al-Pulver
Co	> 99 %	< 1 μm	Ceratizit	Co S160/505
Ni	> 99 %	3–6 μm	Hart Materials	Vale Ni 123
Ta	> 99 %	unknown	unknown	Tantal
W	> 99 %	0.99 μm	wolfram	W05-10
WC	> 99 %	5.65 μm	wolfram	WC50-90

2.1.2 Heating Furnaces

Induction heated Furnace

Melting, smelting and infiltration was carried out in an induction heated vertical tube furnace (IT-GRV-40-80-2150, Linn High Therm GmbH). The powder mixture was put into an alumina crucible which was placed inside a graphite cylinder. This setup was transferred into the heating zone of the furnace which was layered with graphite felt on the inside and surrounded by a water-cooled copper coil. The temperature was measured using a type C thermocouple with a protective molybdenum coating (Nanmac Inc.) with

its tip positioned just above the alumina crucible. A constant flow of 160 l/h argon with a purity of 99.999 % was applied for 15 min to replace most of the air before the aggregate was heated up. With the argon flow kept constant, the sample was heated up to the desired temperature in 20 min which was held for different dwell times depending on the preparation step. After that, the power generator was turned off and without active cooling the sample reached below 50 °C after 40 min where it was removed from the oven.

Vacuum Furnace

For solution heat treatment a custom-built vacuum furnace with silicon carbide heating elements was utilized. Multiple samples were placed inside an alumina boat onto a layer of alumina sand and covered with an yttria coated graphite plate. A pressure below 0.1 mbar was obtained inside the ceramic tube with a rotary vane pump and the temperature was measured by three type R thermocouples and controlled by a Eurotherm 2418 (EMSR Eurotherm GmbH). After evacuation for at least 15 min, the temperature was usually raised to 1250–1300 °C within 3 h and held there for 12 h. No active cooling was applied, and the oven reached manageable temperatures below 100 °C after 8–10 h. The rotary vane pump was turned off and the samples were removed after ventilation of the ceramic tube.

Compact Tube Furnace

A Nabertherm RD 30/200/11 (Nabertherm GmbH) was used for precipitation heat treatment. The samples were placed into a quartz boat and transferred to the heating zone. The quartz tube was flushed with 20 l/h argon (99.999 % purity) for at least 15 min. After reducing the argon flow to 3–5 l/h, the oven was heated to 950 °C within 1 h and the temperature was held for 48 h. Without active cooling the temperature dropped below 700 °C after 30 min. At this point, the quartz boat was moved from the heating zone to the cooler end of the quartz tube for 1 h and removed from the aggregate entirely afterwards.

2.1.3 Metallographic Preparation

Cutting of samples was carried out in a high precision cut-off machine (Accutom-5, Struers GmbH) using a diamond plated steel wheel at 2700 rpm with a feed of 20-35 $\mu\text{m/s}$. The samples were embedded in bakelite (DuroFast, Struers GmbH) which was compacted for 7 min at 180 °C and 250 bar using a CitoPress-1 (Struers GmbH).

A TegraPol-31 (Struers GmbH) equipped with a TegraDoser-5 (Struers GmbH) was used for grinding and polishing the surface of the embedded samples according to the scheme in Table 3. The samples were rinsed under water, cleaned in an ultrasonic bath suspended in isopropyl alcohol for 5 min, rinsed under fresh isopropyl alcohol and dried with a blow-drier after each step. Step 4 was repeated if the outcome was not satisfactory.

Table 3: Metallographic preparation steps for grinding and polishing the embedded samples. * Struers GmbH.

Step	Duration (min)	Grinding Disc	Grit/Suspension	Coolant
1	4	MD-Piano*	120	Water
2	4	MD-Allegro*	DiaDuo-2 9 μm^*	DP-Lubricant Blue*
3	4	MD-Dac*	DiaDuo-2 3 μm^*	DP-Lubricant Blue*
4	6	MD-Nap*	DiaDuo-2 1 μm^*	DP-Lubricant Blue*

2.1.4 Scanning Electron Microscopy

Instrumental

The microstructure of the samples was analyzed using a FEI Quanta 200 SEM (Thermo Fisher Scientific Inc.) equipped with a backscattered electron detector (BSE). The instrument was operated in high vacuum mode (HV) at cathode acceleration voltages of 15–20 kV with the beam focused to a spot size of 3–5 nm.

For compositional analysis (EDS), an energy dispersive x-ray detector (EDAX Octane Pro, Ametek Inc.) was mounted into the sample chamber at an angle of 45 °.

Quantification

The algorithms of the instrument's software EDAX TEAM™ delivered severely wrong results for the standardless quantification of sample compositions. Particularly, tungsten concentrations were underestimated in the order of 20–30 %. Unfortunately, this was resolved quite late into the work where most of the evaluations have been completed and cannot be repeated due to lack of time. Only the binder compositions of cemented carbides which were synthesized via DTA were reevaluated using a workaround as described in chapter 2.5.

Quantification results for two alloys from chapter 2.2.4 analyzed with different instruments are compared in Table 4. The best agreement with the targeted composition is expectedly achieved by wet chemical decomposition and atomic emission spectroscopy measurement. As mentioned above, the EDAX TEAM™ software underestimates the tungsten concentration by 20.8 and 24.6 % for the cold boat and Hukin crucible sample, respectively. All other quantification methods also lead to underestimated tungsten concentrations, but the error is well below 10 %.

Table 4: Difference in quantification results for two alloys analyzed using the instrument described in chapter 2.1.4 (TEAM™), wet chemical decomposition and atomic emission spectroscopy measurement (ICP-OES), another SEM instrument from the Federal Monuments Authority Austria which utilizes a Bruker detector and quantification software (FMAA), a PANalytical PW4025 MiniPal desktop x-ray fluorescence spectrometer (XRF) and the workaround described in chapter 2.5 (WA). Compositions are given in wt%.

Sample	Element	Target	TEAM™	ICP-OES	FMAA	XRF	WA
Cold boat	Co	60.3	64.1	59.1	61.6	61.5	61.8
	Ni	13.7	15.4	14.2	13.8	13.6	14.0
	W	26.0	20.6	26.7	24.5	24.8	24.2
Hukin crucible	Al	4.5	4.9	4.4	–	–	5.1
	Co	57.5	62.6	56.9	–	–	58.7
	Ni	13.2	13.8	13.4	–	–	12.8
	W	24.8	18.7	25.3	–	–	23.4

Z-Contrast

The contrast of phases in BSE micrographs depends on the average atomic number of participating elements because heavy elements scatter electrons at a higher rate than light elements. This dependency is approximated for measurements at 20 kV in [41] by the mathematical expression

$$\eta = -0.0254 + 0.016 * Z_{av} - 1.86 * 10^{-4} * Z_{av}^2 + 8.3 * 10^{-7} * Z_{av}^3$$

where η is the backscattered electron coefficient and Z_{av} is the average atomic number which is calculated with the mass fraction w_i of each element i by

$$Z_{av} = \sum_i Z_i * w_i$$

The Z-contrast between two phases is derived as the relative difference between their backscattered electron coefficients, i.e. $(\eta_1 - \eta_2) / \eta_1$.

2.1.5 Combustion Carbon Analysis

Measurements of the carbon concentration were carried out with a carbon/sulfur combustion analyzer (LECO GmbH). At the beginning of each analysis, the drift of the instrument was corrected by five blank measurements. The results were corrected through one-point calibration with three measurements each of following standards: 0.11 wt% C (LECO® 501-676), 0.82 wt% C (LECO® 501-679) and 3.32 wt% C (LECO® 501-024). 3–5 pieces with similar mass (150–500 mg) of each sample were measured.

2.1.6 Difference Thermal Analysis

A TG-DTA/DSC apparatus (STA 449 C, NETZSCH Holding) was used for determination of γ' solvus temperature in superalloys and for synthesis and subsequent thermal analysis of cemented carbides. Two alumina crucibles, one filled with the sample and the other one as reference material, were placed onto the temperature sensors, which were both type S thermocouples. The furnace was equipped with a rhodium heating element and its temperature was also measured with a type S thermocouple. The balance system was protected from sample out-gassing products by a constant flow of 10 ml/min argon (99.999 % purity) and the sample room was purged with the same gas at 50 ml/min.

Some pieces of titanium foil were placed into the sample room to remove most of the remaining oxygen from the purge gas. Before the start of each measurement, the sample room was evacuated and backfilled with argon three times.

The measurements were evaluated using Proteus Thermal Analysis software (NETZSCH Holding). Phase transformation temperatures were only determined from DSC heating curves to rule out undercooling. First, the reactions were identified in the cooling curves where the temperature differences are more pronounced since the effects elapse faster. Then in heating curves, the temperature was determined as the extrapolated onset and the extrapolated end of peaks for solidus and solvus reactions, respectively.

2.1.7 Thermo-Calc Calculations

Thermodynamic calculations were carried out for comparison with experimental results using Thermo-Calc Version 2020a (Thermo-Calc Software AB). The utilized databases are listed in Table 5 and some of the calculation scripts can be found in the appendix.

Table 5: List of used databases, the relevant defined elements, and their sources.

Database	Elements	Source
TCCC1	C, Co, Ni, W	[42]
TCFE9	C, Al, Co, Ni, W	[43]
Wang17	Al, Co, W	[33]
Zhou16	C, Co, Ni, W	[26]
Zhu14	Al, Co, Ni, W	[12]

2.2 Superalloys

2.2.1 Stability of γ' precipitation

Four compositional different alloys were initially chosen for gaining experience in working with superalloys and finding the right heat treatment parameters and other variables that can influence the formation of the γ' phase. Table 6 lists the target compositions of the alloys and their literature sources. All of them form cuboidal γ' precipitates and were composed of similar elements.

Table 6: Target compositions in at% of selected superalloys for an assessment of how compositional and preparational parameters influence the results. Including literature sources.

Sample	Al	Co	Ni	Ta	W
CoA1 [44, 45]	9.0	81.0	–	2.0	8.0
CoA2 [9]	9.0	83.0	–	–	8.0
CoNiA1 [46]	11.0	49.0	30.0	3.0	7.0
CoNiA2 [2]	12.5	52.5	30.0	–	5.0

Chronologically, alloys CoA1 and CoNiA1 were prepared first and the results of their compositional analysis was used to adjust the preparation parameters for alloys CoA2 and CoNiA2. Since 10 % aluminum and 20 % tungsten seemed to be lost throughout the preparation, the weighed-in quantity was elevated by these numbers to compensate for the loss. However, as described in chapter 2.1.4, the quantification results are not reliable and the change in composition is most probably not as drastic as assumed. The weighed-in compositions given in Table 7 will be considered true values and the alloys will be renamed after their composition to facilitate reading in the results section.

Two batches each of Co₉Al₈W₂Ta and Co₃₀Ni₁₁Al₇W₃Ta were produced because they were used for a heat treatment assessment. Preparation of Co₁₀Al₁₀W and Co₃₀Ni₁₄Al₆W was done only once. Details are described in chapter 2.2.3.

Table 7: Weighed-in compositions in at% of alloys from Table 6 with their new compositional name in the first row.

Sample	Compositional Name	Al	Co	Ni	Ta	W
CoA1	Co9Al8W2Ta	9.0	81.0	–	2.0	8.0
CoA2	Co10Al10W	9.9	80.5	–	–	9.6
CoNiA1	Co30Ni11Al7W3Ta	11.0	49.0	30.0	3.0	7.0
CoNiA2	Co30Ni14Al6W	13.7	50.3	30.0	–	6.0

2.2.2 Variation of Nickel

For an assessment of the influence of nickel on the formation of γ' , especially in cemented carbides, another four samples were prepared. The weighed-in compositions and their compositional names are given in Table 8. Details of the preparation and analysis of these samples are described in chapter 2.2.3.

Table 8: Weighed-in compositions in at% of alloys from the assessment of nickel variation.

Sample	Al	Co	Ni	W
Co12Al11W	12.1	77.1	–	10.8
Co15Ni12Al11W	12.1	62.1	15.0	10.8
Co30Ni12Al11W	12.1	47.1	30.0	10.8
Co45Ni12Al11W	12.1	32.1	45.0	10.8

2.2.3 Preparation Details

The preparation of powder mixtures from samples of chapters 2.2.1 and 2.2.2 was done according to chapter 2.1.1 but instead of mixing all elements at once, aluminum and double its weight of cobalt were held back for the first melting step. For example, Co10Al10W has a composition of 4 wt% aluminum, 70 wt% cobalt and 26 wt% tungsten. So, for 10 g of this first-step powder only 6.2 g cobalt and 2.6 g tungsten were mixed. The remaining 0.4 g aluminum and 0.8 g cobalt were added later, as described below. This had to be done to suppress the loss of aluminum during the first melting step which was carried out in the induction furnace (see chapter 2.1.2) at 1550 °C for a dwell time of 25 min. The remaining aluminum and cobalt were added in form of a 1:2 powder mixture which was weighed into the alumina crucible and the ingot of the first step was

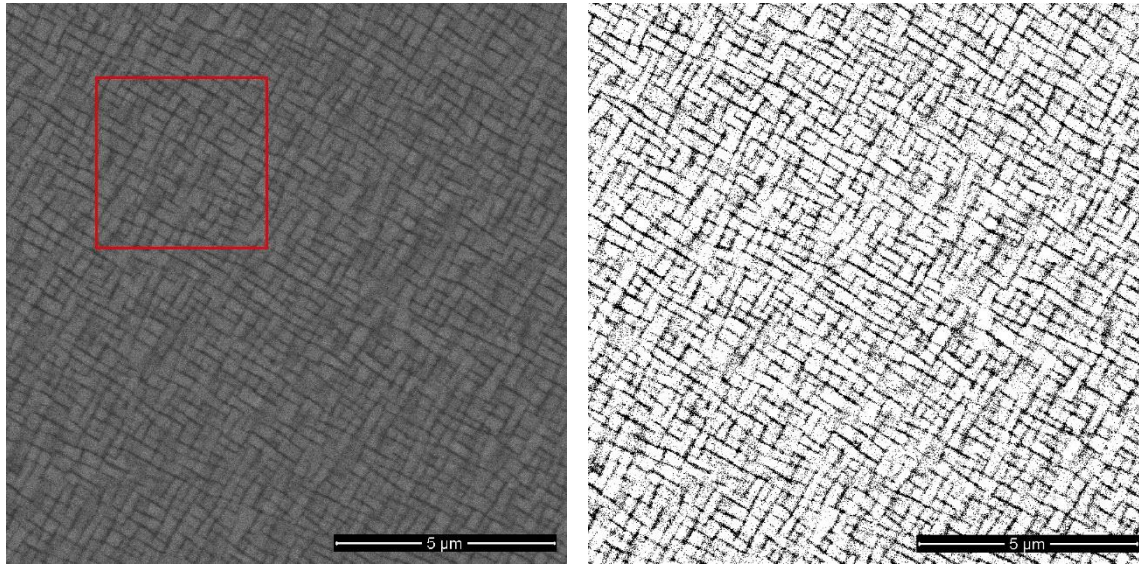


Figure 3: BSE micrograph of a superalloy which was analyzed using ImageJ. The original image (left) was transformed into a monochrome image (right) with a visually determined grayscale threshold where the white areas are γ' phase. Cutout regions as indicated with the red square were used for measurement of the γ' particle size with the polygon selection tool.

placed on top of it. Again, the induction furnace was used for melting at 1500 °C for a dwell time of 15 min. Finally, the sample was homogenized three times through flipping and smelting it in the induction furnace at 1450 °C for a dwell time of 20 min. Every sample had a final mass of approximately 4 g. Heat treatments were carried out as described in chapter 2.1.2, the different variations will be discussed in the results section. The samples were metallographically prepared (see chapter 2.1.3) and characterized using SEM and EDS (see chapter 2.1.4). DTA was also carried out (see chapter 2.1.6). A zig-zag temperature profile with two heating ramps to 1400 °C and intermediate cooling to 600 °C at a rate of 10 K/min was applied.

The samples were metallographically analyzed using ImageJ (National Institute of Health, version 1.53e) which is exemplarily shown in Figure 3. The grayscale threshold of SEM images was determined visually, so that the γ' phase has a greyscale value of 255 (white). The volume fraction of γ' was derived as the number of white pixels divided by the total number of pixels. The particle size was determined using the same software. The scale was set to the inserted scale of the SEM image and γ' particles were measured using the polygon selection tool. Five cutout regions each consisting of 30–70 particles were analyzed that way for every sample.

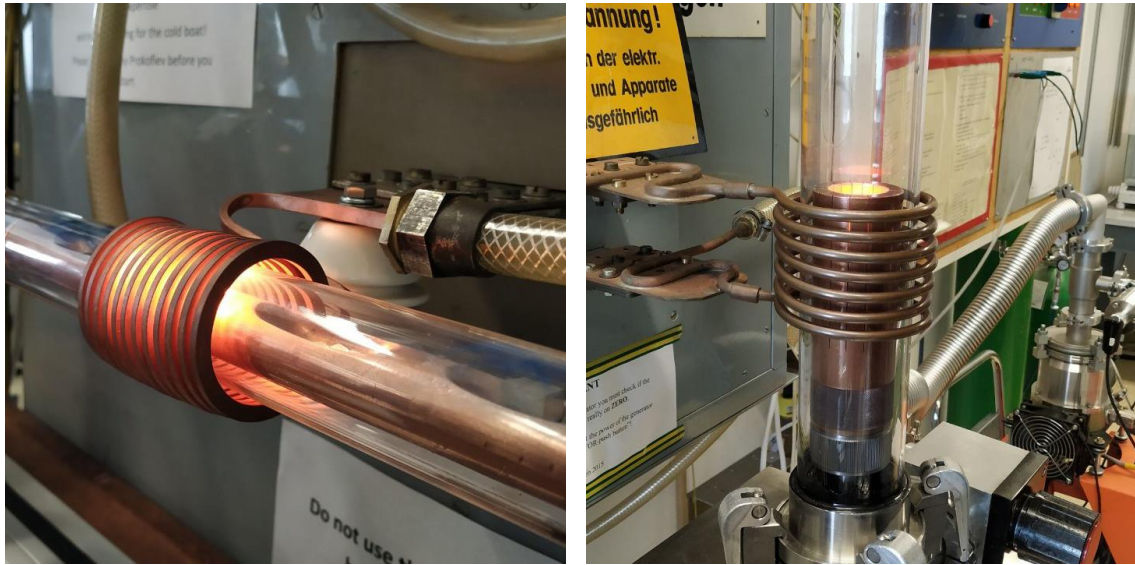


Figure 4: Photographs of the cold boat induction furnace (left) and the Hukin crucible aggregate (right) which were used for producing bigger batches (approximately 20 g) of Co₁₅Ni₁₁Al₉W.

2.2.4 Cold Boat and Hukin Crucible

A bigger sized batch of 50 g superalloy with a weighed-in composition of 65 at% cobalt, 15 at% nickel, 11 at% aluminum and 9 at% tungsten was prepared in an alternative way. Using the same compositional naming scheme as before (see chapter 2.2.1, Table 7), the sample will be called Co₁₅Ni₁₁Al₉W. A powder mixture of 60.2 wt% cobalt, 13.8 wt% nickel and 26.0 wt% tungsten was prepared according to chapter 2.1.1 first. It was pressed into bars approximately 5 cm x 0.5 cm x 0.5 cm in size using a uniaxial press with a force of 2.2 t. These bars were sintered at 1100 °C under hydrogen (99.999 % purity) in the compact tube furnace (see chapter 2.1.2) for 3 h. Afterwards, each of them was broken into four pieces using a pendulum impact test machine.

A cold boat induction furnace was used for melting and homogenizing the sintered bar pieces (see Figure 4). It consisted of a water-cooled copper tube with four dents for sample placement which was encased in a gastight quartz tube. This setup was movable in the horizontal direction, so that a fixed water-cooled copper coil would surround each sample individually. After placement of the sintered bar pieces, the quartz tube was evacuated for 20 min and backfilled with argon (99.999 % purity) four times before the power generator was turned on. The power output was tuned using a potentiometer and

raised until the sample was melted and homogenized thoroughly, approximately for 1 min. The whole process was repeated for each sample.

8–9 pieces were weighed and the remaining 4.5 wt% aluminum were cut from an aluminum wire (99.99 % purity) for a total mass of approximately 20 g. The material was transferred into a water-cooled Hukin crucible which was encased in a gastight quartz tube and surrounded by a water-cooled copper coil (see Figure 4). The remaining steps of the procedure were like for the cold boat induction furnace, but the sample was homogenized even longer, approximately 3 min. This melting process was repeated two times and the ingot was flipped each time. Another batch of 20 g was prepared the same way.

2.3 Influence of Carbon

Samples with different carbon content were prepared for the connecting link between superalloys and cemented carbides. The effect of an increasing carbon concentration on the formation of γ' , κ and other phases was studied. Two series of six samples were prepared, one without nickel and the other with a nickel concentration of 30 at%. Aluminum and tungsten concentrations were kept constant for all samples at 11 and 9 at%, respectively. The weighed-in carbon concentrations were 0, 1, 2, 5, 10 and 15 at% but changed drastically through the preparation process which was shown with combustion carbon analysis (see chapter 2.1.5) afterwards. Compositional changes of the other elements were not quantified since the results from EDS are wrong (see chapter 2.1.4) and quantification of carbon containing samples with this method is unreliable anyway. The alloys were prepared as described in chapters 2.1.1 and 2.1.2 with only one melting step in the induction furnace at 1550 °C for a dwell time of 25 min and subsequent solution and precipitation heat treatment. The compositional names of the samples are similar to the ones from chapter 2.2, where concentrations for nickel, aluminum, tungsten and carbon are given in at% before the name of the element and the rest is cobalt. For example, Co9Al7W is an alloy of 9 at% aluminum, 7 at% tungsten and 84 at% cobalt to balance it out.

Additionally, two cemented carbide samples with slightly different carbon contents were prepared. Their weighed-in compositions are given in Table 9. They were designed to equal cemented carbides with 30 wt% Co9Al7W as binder phase. The powders were mixed as described in chapter 2.1.1 and liquid phase sintering was carried out in the vacuum furnace (see chapter 2.1.2) at 1460 °C for 1 h. The sample 70WC-Co9Al7W-0.6C was solution heat treated at 1300 °C for dwell times of 3 and 24 h.

Table 9: Weighed-in compositions in wt% of two cemented carbides with slightly different carbon content. They are compositional equal to a mixture of 30 wt% Co9Al7W, 0.4 or 0.6 wt% carbon and tungsten carbide to balance.

Sample	C	Al	Co	W
70WC-Co9Al7W-0.4C	4.7	1.1	22.9	71.3
70WC-Co9Al7W-0.6C	4.9	1.1	22.9	71.1

2.4 Cemented Carbides via Infiltration

Pieces of the superalloys which are described in chapter 2.2 were weighed and four times this mass of a mixture of tungsten carbide with additional 0.6 wt% carbon was poured into an alumina crucible. The superalloy was placed on top of it and the samples were infiltrated in the induction furnace (see chapter 2.1.2) at 1500 °C for a dwell time of 10 min. The samples were solution and precipitation heat treated according to chapter 2.1.2, metallographically prepared (see chapter 2.1.3) and analyzed using the SEM with EDS (see chapter 2.1.4). Measurements of binder compositions and their distribution throughout the sample were carried out after each preparation step. The absolute results are not reliable as described in chapter 2.1.4 but they will be compared among each other.

2.5 Cemented Carbides via DTA

Cemented carbides with constant binder contents but different binder compositions were synthesized and analyzed using DTA as described in chapter 2.1.6. Four binder series with 0.0, 2.5, 5.0 and 7.5 wt% aluminum, each with cobalt to nickel ratios of 100:0, 85:15, 50:50, 15:85 and 0:100, were prepared according to chapter 2.1.1. Two samples of each binder composition were needed, one with carbon deficit and the other with

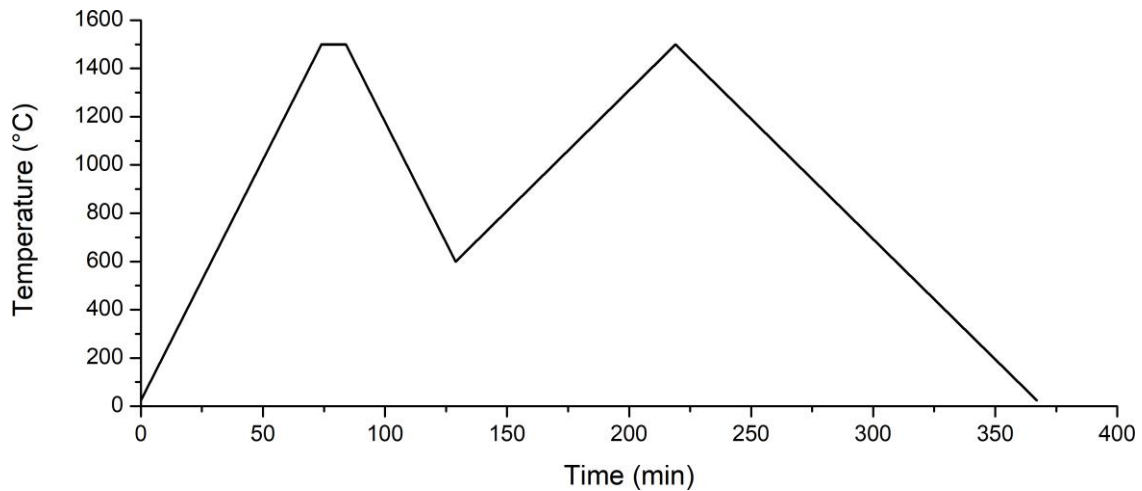


Figure 5: Zig-zag temperature profile for synthesis and measurement of cemented carbides with the difference thermal analyzer. The first heating and cooling ramps were carried out at a temperature change rate of 20 K/min and the second ramps at 10 K/min. The dwell time for the synthesis at 1500 °C was 10 min.

excess carbon, for measurements left and right outside the carbon window. The prepared powders had a total mass of 5 g and were composed of 20 wt% binder, 69 wt% tungsten carbide for samples with carbon deficit and 11 wt% tungsten or 20 wt% binder, 79 wt% tungsten carbide and 1 wt% carbon for samples with excess carbon, respectively. This corresponds to 4.23 and 5.84 wt% carbon, respectively. The weighed-in compositions are given in the appendix in chapter 6.1.1. The nomenclature of samples works as follows: The binder composition is given by the six characters after “WC”, where the first two and the second two characters represent the cobalt and nickel proportion of the cobalt-nickel ratio, respectively. “Co” means 100 % cobalt and “Ni” means 100 % nickel of the cobalt-nickel-ratio. The last two digits give the aluminum concentration of the binder in 10 x wt%. The “W” and “C” at the end indicates if it is tungsten- or carbon-rich, respectively. For example, “WC851525W” represents a mixture of 69 wt% tungsten carbide, 11 wt% tungsten and 20 wt% binder with a composition of 82.9 wt% cobalt, 14.6 wt% nickel and 2.5 wt% aluminum. 500–700 mg of these powders were used for each experiment and some of them were repeated to check for reproducibility.

A zig-zag temperature profile (see Figure 5) with two heating and cooling ramps was applied. The first step was considered synthesis of the cemented carbide and the sample was heated to 1500 °C and cooled to 600 °C with a rate of 20 K/min including an additional 10 min dwell at the maximum temperature. The second step was the actual measurement with heating to 1500 °C and cooling to room temperature at a rate of 10 K/min.

The samples were metallographically prepared (see chapter 2.1.3) and characterized using SEM and EDS (see chapter 2.1.4). The main goal was the identification of present phases. Therefore, pictures were recorded at two magnifications, a lower one for a common section of the sample and a higher one for analysis of the binder microstructure. Visually unrecognizable phases were further investigated through compositional analysis. Additionally, the composition of the binder phase was measured as well.

Since valid results for the binder composition were highly demanded, quantification with the default evaluation software was not feasible. Instead, spectrum files were converted into a file format which is readable by another evaluation software Quantax (Bruker Nano GmbH). But the characteristics of the detector have a strong influence on the quantification result and must be delivered through the spectrum file. The necessary parameters were lost through the export process and had to be recovered with the available information. The position of the detector was at 35 ° elevation angle and at 45 ° azimuth angle. The detector is a conventional lithium-drifted silicon detector with a thickness of 4 μm and the dead layer was estimated with 0.1 μm. The window is a super ultrathin window (Super UTW) with a thickness of 0.3 μm and an aluminum layer of 0.04 μm thickness. The Fano factor was determined from the peak widths of one spectrum interactively using the Quantax software. Validation of this parameter set was done using spectra of two samples with known composition. The quantification yielded errors well below 10 % (see chapter 2.1.4, Table 4, WA).

2.6 Ab Initio Calculations

Ground-state energies of elements in their reference state structure and compounds with L_{12} (γ') and E_{21} (κ) structure were calculated using the projector-augmented wave (PAW) method [47, 48] as implemented in the ABINIT software package [49-51]. The exchange-correlation functional was the Perdew-Burke-Ernzerhof form of the generalized gradient approximation [52] and PAW atomic data was taken from the JTH v1.1 dataset [53]. The structures were calculated with full spin polarization and the cell parameters were fully relaxed using the Broyden-Fletcher-Goldfarb-Shanno minimization [54]. A non-shifted Monkhorst-Pack [55] scheme (MP) was used for the automatic generation of

k-points in the irreducible Brillouin zone. The number of bands and their occupation numbers were determined in respect to the Gaussian smearing scheme [56] with a broadening parameter of 0.001 hartree. Part of the computational results have been achieved using the Vienna Scientific Cluster (VSC).

The total energy of each structure was calculated in three steps: First, an estimate of the cell parameters was obtained through a fast calculation with a MP of $8 \times 8 \times 8$ and relatively large convergence parameters for the total energy (toldfe) and for the force during structural optimization (tolmxf) with $1\text{E-}6$ hartree and $5\text{E-}4$ hartree/bohr, respectively. The maximum kinetic energy for the allowed plane waves (ecut) was set to 40 hartree. With the approximate value for the cell parameter, a convergence study for the optimal value of ecut was conducted with values from 30 to 110 hartree or in some cases even up to 150 hartree. The final sized MP of $20 \times 20 \times 20$ was used but toldfe and tol mxf were not changed. The convergence criterium for the value of ecut was set to $1\text{E-}4$ hartree difference to the lowest calculated total energy. Finally, another calculation with the converged ecut, a much smaller toldfe of $3.675\text{E-}8$ hartree and a slightly smaller tol mxf of $1\text{E-}4$ hartree/bohr completed the search for the total energy.

The enthalpy of formation $\Delta_f H$ for the various structures was calculated according to [18] as the difference between the total energy of the structure and the total energies of the reference state elements it is composed of. For example, the enthalpy of formation of Co_3AlC was derived as

$$\Delta_f H_{\text{Co}_3\text{AlC}} = E_{\text{Co}_3\text{AlC}}^{E2_1} - \left[\frac{3}{5} E_{\text{Co}}^{\text{hcp}} + \frac{1}{5} E_{\text{Al}}^{\text{fcc}} + \frac{1}{5} (E_{\text{C}}^{\text{d}} - 1.895 \text{ kJ}) \right]$$

where $E_{\text{Co}_3\text{AlC}}^{E2_1}$ is the total energy of Co_3AlC in $E2_1$ structure and $E_{\text{Co}}^{\text{hcp}}$, $E_{\text{Al}}^{\text{fcc}}$ and E_{C}^{d} are the total energies of hcp cobalt, fcc aluminum and diamond, respectively. The total energy of carbon in its reference state, i.e. graphite, cannot be calculated easily and instead, the total energy of diamond is corrected by the energy difference in respect to graphite (1.895 kJ). All energy values are scaled per mole and atom.

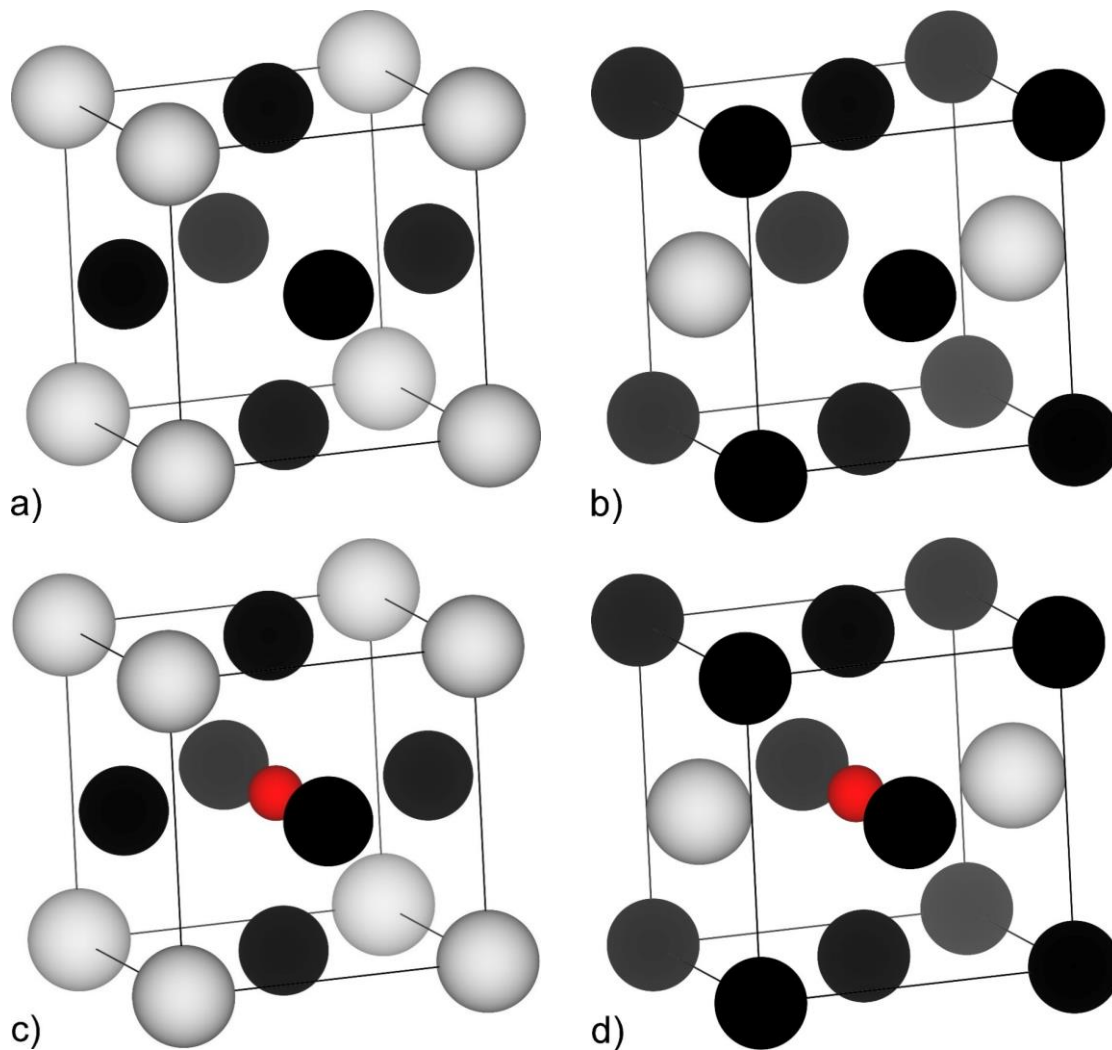


Figure 6: $L1_2$ (a and b), $E2_1$ -I (c) and $E2_1$ -II (d) structure types with two possibilities of atom placement. Either the B atom (a and c) or one of the three A atoms (b and d) occupies the corners. The structures in a) and b) are crystallographically equivalent. The spheres are colored black, lightgray and red representing A, B and C, respectively.

There are two possible ways how the atoms occupy the positions in each structure type which are shown in Figure 6. The compounds may be denoted as A_3B or A_2BA and A_3BC or A_2BAC for the $L1_2$ and $E2_1$ structures, respectively. The corners are occupied by the B atom in the former compound of each structure type and by one A atom in the latter one. But the structures in Figure 6 a) and b) are crystallographically equivalent because they can be converted into each other through translation operations. Thus, only one compound A_3B with $L1_2$ structure must be considered. This equivalence is lost through the insertion of a carbon atom into the octahedral void of the face atoms and the structures in Figure 6 c) and d) will be called $E2_1$ -I and $E2_1$ -II, respectively.

3 Results and Discussion

3.1 Superalloys

3.1.1 Stability of γ' precipitation

Heat Treatment Assessment

The samples Co9Al8W2Ta and Co30Ni11Al7W3Ta were metallographically analyzed in six different heat treatment conditions: as cast, precipitation heat treated for 48 h at 950 °C, solution heat treated for 12 h at 1215 and 1290 °C plus each one precipitation heat treated for 48 h at 950 °C. The images in Figure 7 show a common section of both alloys after precipitation heat treatment. Besides γ/γ' , a white phase can be seen which seems to occupy the grain boundaries of Co9Al8W2Ta but is found inside of grains in Co30Ni11Al7W3Ta. The phases differ in shape in each alloy and the compositions given in Table 10 confirm their difference. In Co9Al8W2Ta the existence of D0₁₉ is very likely since this phase appears to be stable in cobalt-rich ternary alloys with aluminum and tungsten [11, 57]. The sample L03 from [11] quite resembles this alloy if one assumes that tungsten and tantalum react similarly and the compositions of D0₁₉ match almost perfectly (see Table 10). Solution heat treatment seems to reduce the amount of D0₁₉, and precipitation heat treatment promotes its formation. This becomes clear if one considers the cobalt-tungsten-binary system to simplify matters. There, the upper limit temperature of D0₁₉ – usually denoted as Co₃W – is at around 1100 °C [33]. No D0₁₉ phase was found in Co30Ni11Al7W3Ta which seems reasonable since nickel tends to extend the γ/γ' two-phase region [2]. Instead, a tantalum-rich phase is observed which is not affected by heat treatments. The ratio between refractory elements and the rest is almost 2:1 so an intermetallic phase like (Al,Co,Ni)(Ta,W)₂ might be considered. CoTa₂ and NiTa₂ can be found in the underlying binary systems and they form a homogeneity region in the ternary system [58]. The upper limit temperature for these intermetallic compounds is around 1800 °C, so the phase probably was formed during preparation and could not be dissolved anymore. It is not clear if the higher tantalum concentration or the nickel is the reason why it does form in this alloy but does not in Co9Al8W2Ta.

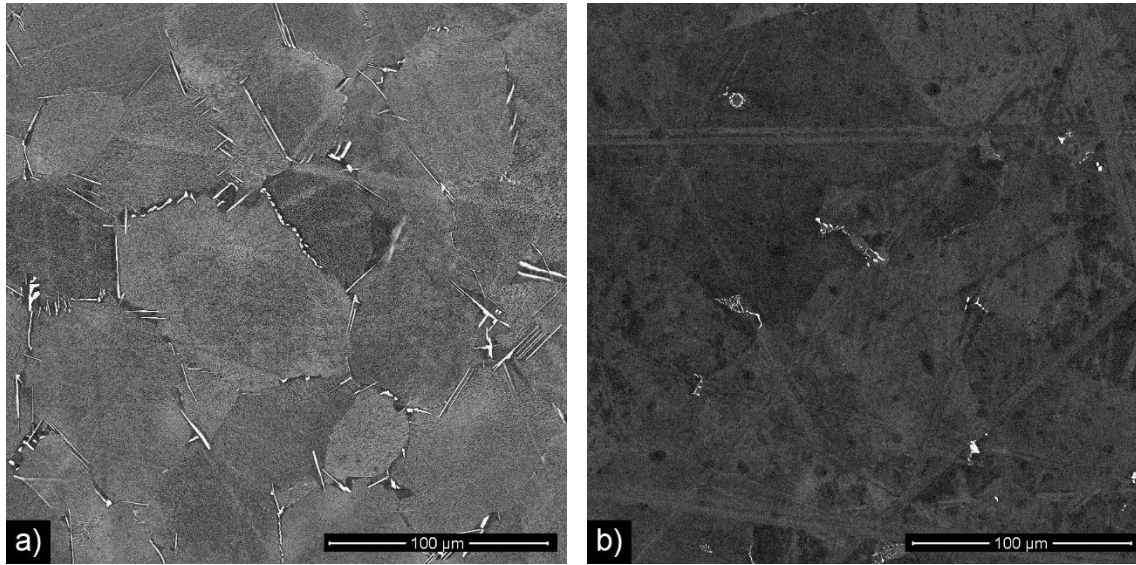


Figure 7: BSE micrographs of precipitation heat treated (950 °C, 48 h) a) Co9Al8W2Ta and b) Co30Ni11Al7W3Ta show an additional phase at grain boundaries and inside grains, respectively.

Table 10: EDS measured composition (TEAM™ quantification) in at% of the additional phases in alloys from heat treatment assessment after precipitation heat treatment (950 °C, 48 h) and of D0₁₉ in alloy L03 from [11].

Sample	Al	Co	Ni	Ta	W
Co9Al8W2Ta	2.1 ± 0.8	78.6 ± 0.3	–	3.0 ± 0.3	16.2 ± 0.7
L03 (Co8Al10W)	2.3 ± 0.4	75.8 (bal.)	–	–	21.9 ± 0.6
Co30Ni11Al7W3Ta	3.2 ± 1.0	16.3 ± 3.9	9.9 ± 2.8	70.4 ± 6.7	2.9 ± 0.3

Figure 8 shows the microstructure of Co9Al8W2Ta in all heat treatment conditions. When no solution heat treatment is applied, no regular pattern of γ/γ' phases is formed. Instead, the web-like structure as seen in the as-cast condition can be observed. After solution heat treatment for 12 h at 1215 or 1290 °C, similar microstructures of very fine γ' grains are visible in both samples. These are most probably formed during furnace cooling. But after additional precipitation heat treatment for 48 h at 950 °C, the microstructures are quite different and the sample in Figure 8, f) seems to have a more regular γ/γ' structure.

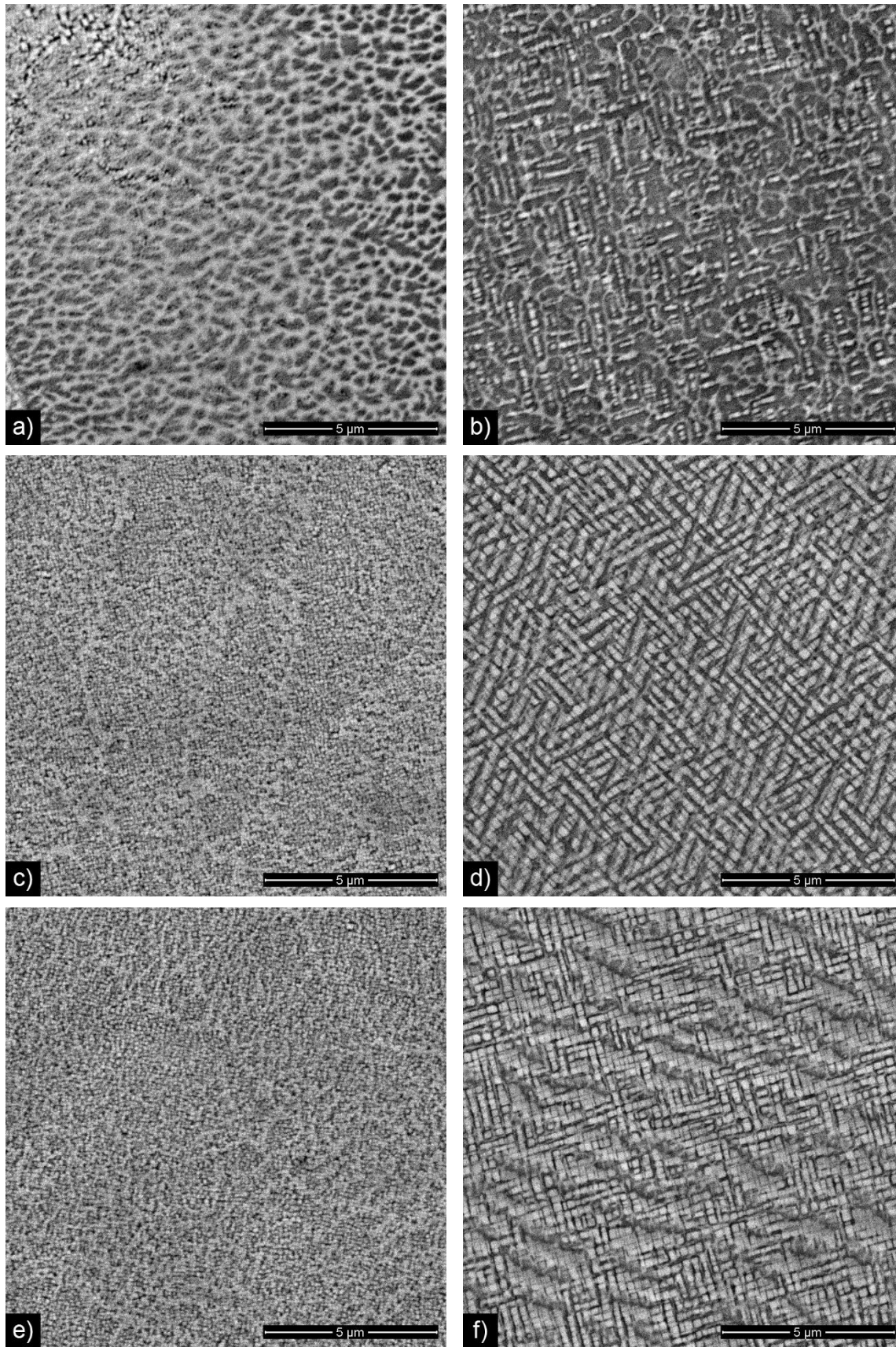


Figure 8: BSE micrographs of Co₉Al₈W₂Ta after different heat treatments. a) as cast, b) after precipitation heat treatment for 48 h at 950 °C, c) and e) after solution heat treatment for 12 h at 1215 and 1290 °C, respectively. d) and f) are like c) and e) but with additional precipitation heat treatment for 48 h at 950 °C.

The addition of nickel readily stabilizes the γ' phase which is known from literature [2, 12] and can also be observed by comparing Figure 9 with Figure 8. The micrographs of Co30Ni11Al7W3Ta show a higher amount of γ' in all heat treatment conditions compared to Co9Al8W2Ta. The shape of the precipitates is more regular, and they are bigger in size when nickel is added to the alloy. Again, solution heat treatment is necessary for a more regular shaped microstructure. But this time, the outcome is equal for the samples which were solution heat treated at 1215 and 1290 °C. The higher amount of aluminum may also be at least partially responsible for these observations.

Compositional Assessment

The reproduced samples from the heat treatment assessment and two additional alloys Co10Al10W and Co30Ni14Al6W are discussed here. The preparational parameters differ slightly from the samples above, for solution heat treatment a temperature of 1300 °C was held for 12 h but precipitation heat treatment was the same with 48 h at 950 °C. The measured compositions for all six superalloys are given in Table 11 but are only shown for comparison reasons since the absolute values are probably wrong (see chapter 2.1.4). Reproducibility between the samples from heat treatment and compositional assessments is very good considering the error margins.

Table 11: EDS measured composition (TEAM™ quantification) in at% of superalloys from heat treatment assessment (h.a.) and compositional assessment (c.a.) after solution heat treatment for 12 h at 1290/1300 °C and precipitation heat treatment for 48 h at 950 °C.

Sample	Al	Co	Ni	Ta	W
Co9Al8W2Ta (h.a.)	8.0 ± 0.5	84.3 ± 0.5	-	1.2 ± 0.3	6.5 ± 0.3
Co9Al8W2Ta (c.a.)	8.4 ± 0.4	84.0 ± 0.4	-	0.9 ± 0.1	6.7 ± 0.2
Co10Al10W	9.2 ± 0.2	83.9 ± 0.2	-	-	7.0 ± 0.1
Co30Ni11Al7W3Ta (h.a.)	10.3 ± 0.3	50.5 ± 0.1	31.8 ± 0.4	1.8 ± 0.2	5.6 ± 0.2
Co30Ni11Al7W3Ta (c.a.)	10.9 ± 0.5	50.8 ± 0.2	30.6 ± 0.4	1.5 ± 0.1	6.2 ± 0.1
Co30Ni14Al6W	12.0 ± 0.4	52.7 ± 0.4	30.9 ± 0.3	-	4.3 ± 0.1

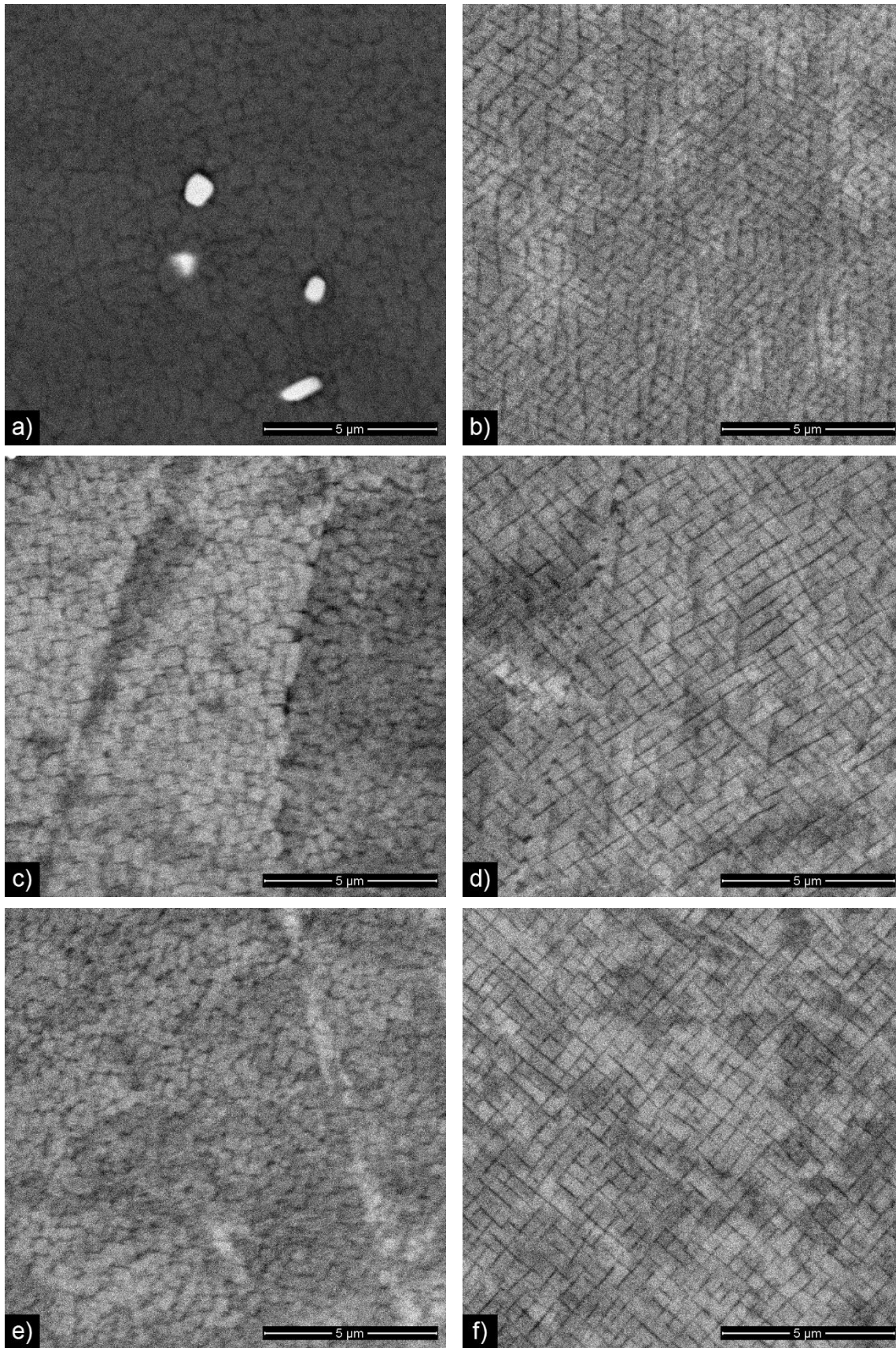


Figure 9: BSE micrographs of Co₃₀Ni₁₁Al₇W₃Ta after different heat treatments. a) as cast, b) after precipitation heat treatment for 48 h at 950 °C, c) and e) after solution heat treatment for 12 h at 1215 and 1290 °C, respectively. d) and f) are like c) and e) but with additional precipitation heat treatment for 48 h at 950 °C.

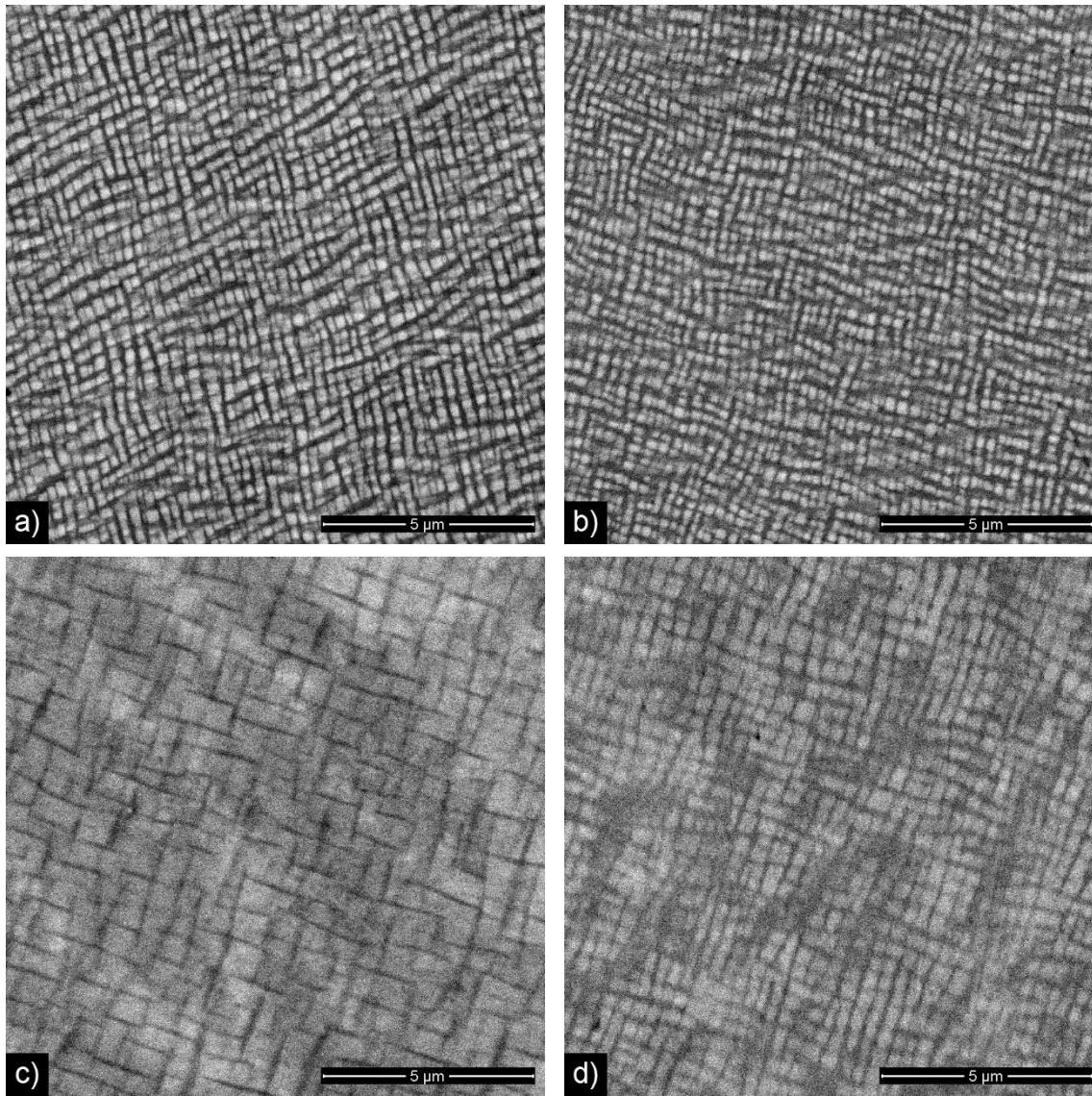


Figure 10: BSE micrographs of compositionally different superalloys after solution heat treatment for 12 h at 1300 °C and precipitation heat treatment for 48 h at 950 °C. a) Co₉Al₈W₂Ta, b) Co₁₀Al₁₀W, c) Co₃₀Ni₁₁Al₇W₃Ta and d) Co₃₀Ni₁₄Al₆W.

Figure 10 shows the microstructure of the four compositionally different alloys. Co₁₀Al₁₀W and Co₃₀Ni₁₄Al₆W do not show any additional phases besides γ and γ' , so the two-phase regions of the systems were hit quite exactly. As expected [59, 60], tantalum stabilizes γ' and leads to a higher particle size, volume fraction and solvus temperature of this phase. This can be seen by comparing Figure 10 a) with b) or Figure 10 c) with d) qualitatively and quantitatively by looking at the results in Table 12. These findings are straightforward in the case of the nickel-free alloys because the amount of refractory elements is the same and, although the aluminum content is higher in Co₁₀Al₁₀W, the stability of γ' is increased in Co₉Al₈W₂Ta. This conclusion is not so clear for the nickel-

containing alloys because the compositional differences between Co₃₀Ni₁₁Al₇W₃Ta and Co₃₀Ni₁₄Al₆W are quite pronounced. But still, a tendency of tantalum stabilizing γ' is not unlikely. The most drastic effect is observed between nickel-free and nickel-containing alloys as already discussed in the heat treatment assessment. However, the added amount of nickel is quite high which should be considered as well.

Table 12: Results of microstructural and difference thermal analysis of compositional different alloys. Calculations of solvus temperatures using Thermo-Calc were not carried out because the Zhu14 database is the only reliable source for this but does not include tantalum in its description.

Sample	γ' particle size (nm ²)	γ' volume fraction	γ' solvus (°C)
Co ₉ Al ₈ W ₂ Ta	53 ± 4	0.62 ± 0.02	1038
Co ₁₀ Al ₁₀ W	39 ± 4	0.56 ± 0.02	1009
Co ₃₀ Ni ₁₁ Al ₇ W ₃ Ta	452 ± 107	0.76 ± 0.05	1184
Co ₃₀ Ni ₁₄ Al ₆ W	128 ± 15	0.69 ± 0.04	1073

3.1.2 Variation of Nickel

All four samples are outside the two-phase region as can be seen in the common sections of the microstructures in Figure 11. There are three additional phases besides γ/γ' , mainly located at the grain boundaries and surrounded by a precipitation-free matrix which indicates the transformation of γ' into other phases at some stage of heat treatment. It is not surprising that these phases appear to be formed in the analyzed alloys because a higher tungsten content tends to promote the formation of D0₁₉ (Co₃W) and μ (C₇W₆) and too much aluminum leads to the formation of B2 (AlCo) [2, 12]. The alloys are certainly not in thermodynamic equilibrium because observing more phases than compounds in an alloy would obey the Gibb's phase rule. Focusing on the simplest case of Co₁₂Al₁₁W, the alloy could be compared to L04 and L05 from [11] because they have the same aluminum content and the tungsten concentration lies between 7.5 and 15 at% from L04 and L05, respectively. The μ phase is not stable at 950 °C in either literature sample, so the observed phase should originate from cooling the liquid phase too slowly. Solution heat treatment for 12 h at 1300 °C could not dissolve it which is reasonable because the upper limit temperature for μ is 1688 °C in the cobalt-tungsten system [33]. The compositions of D0₁₉ and B2 at 950 °C for L04 and L05 compare quite well to

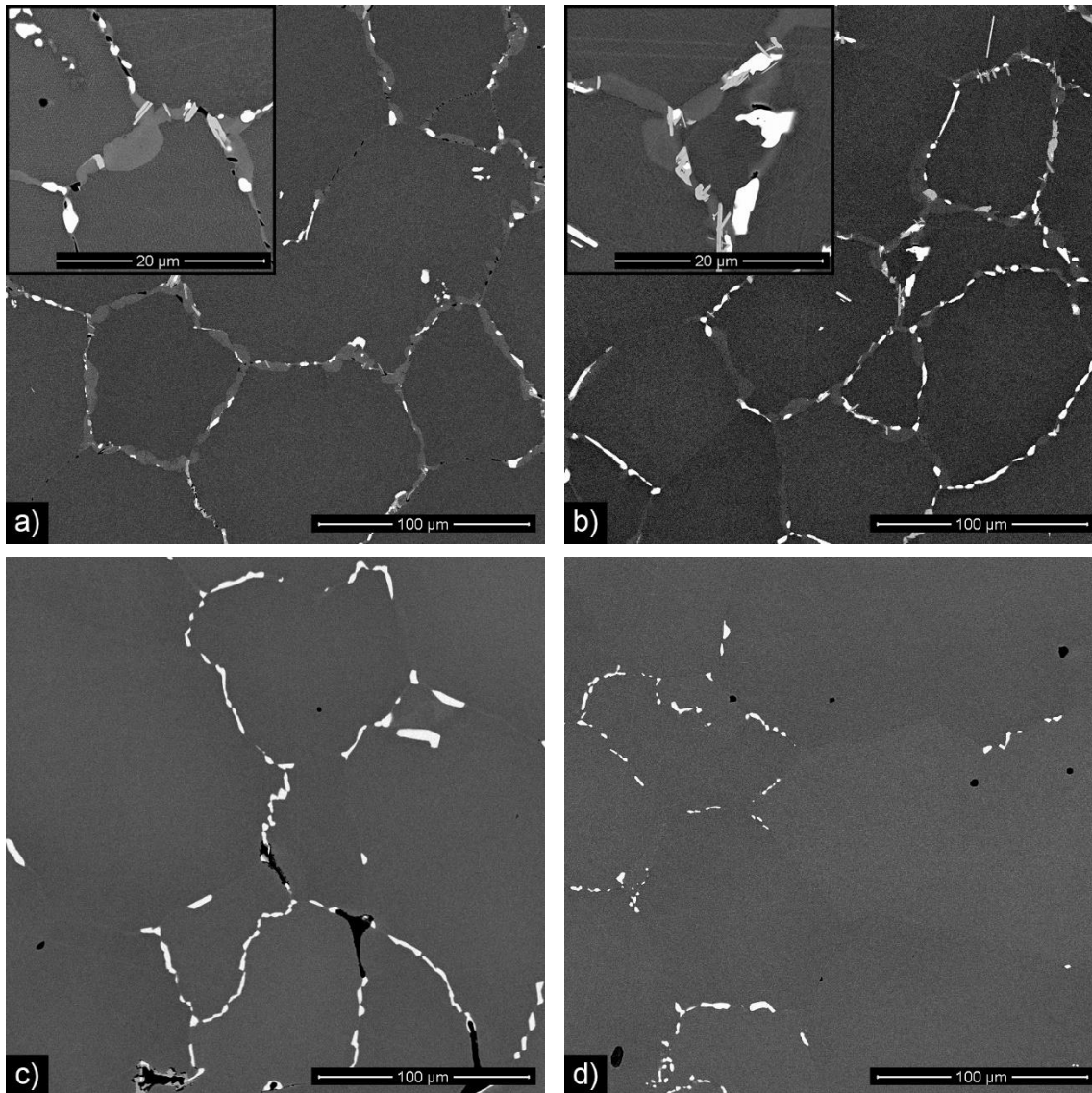


Figure 11: BSE micrographs of common sections from a) Co₁₂Al₁₁W, b) Co₁₅Ni₁₂Al₁₁W, c) Co₃₀Ni₁₂Al₁₁W and d) Co₄₅Ni₁₂Al₁₁W. The phases μ (Co₇W₆), D₀₁₉ (Co₃W) and B₂ (AlCo) are white, light gray and black, respectively.

Table 13: EDS measured composition (TEAM™ quantification) of additional phases in at% compared to values from literature samples with the same aluminum content and 7.5 or 15 at% tungsten in L04 or L05, respectively [11].

Phase	Sample	Al	Co	W
D ₀ ₁₉	Co ₁₂ Al ₁₁ W	3.5 ± 1.3	79.4 ± 0.4	17.1 ± 1.4
	L05 (Co ₁₂ Al ₁₅ W)	2.6 ± 0.4	75.4 (bal.)	22.0 ± 1.2
B ₂	Co ₁₂ Al ₁₁ W	27.9 ± 4.1	67.6 ± 3.0	4.43 ± 1.1
	L04 (Co ₁₂ Al _{7.5} W)	32.4 ± 0.8	63.7 (bal.)	3.9 ± 0.5
	L05 (Co ₁₂ Al ₁₅ W)	32.7 ± 1.7	63.2 (bal.)	4.1 ± 0.5

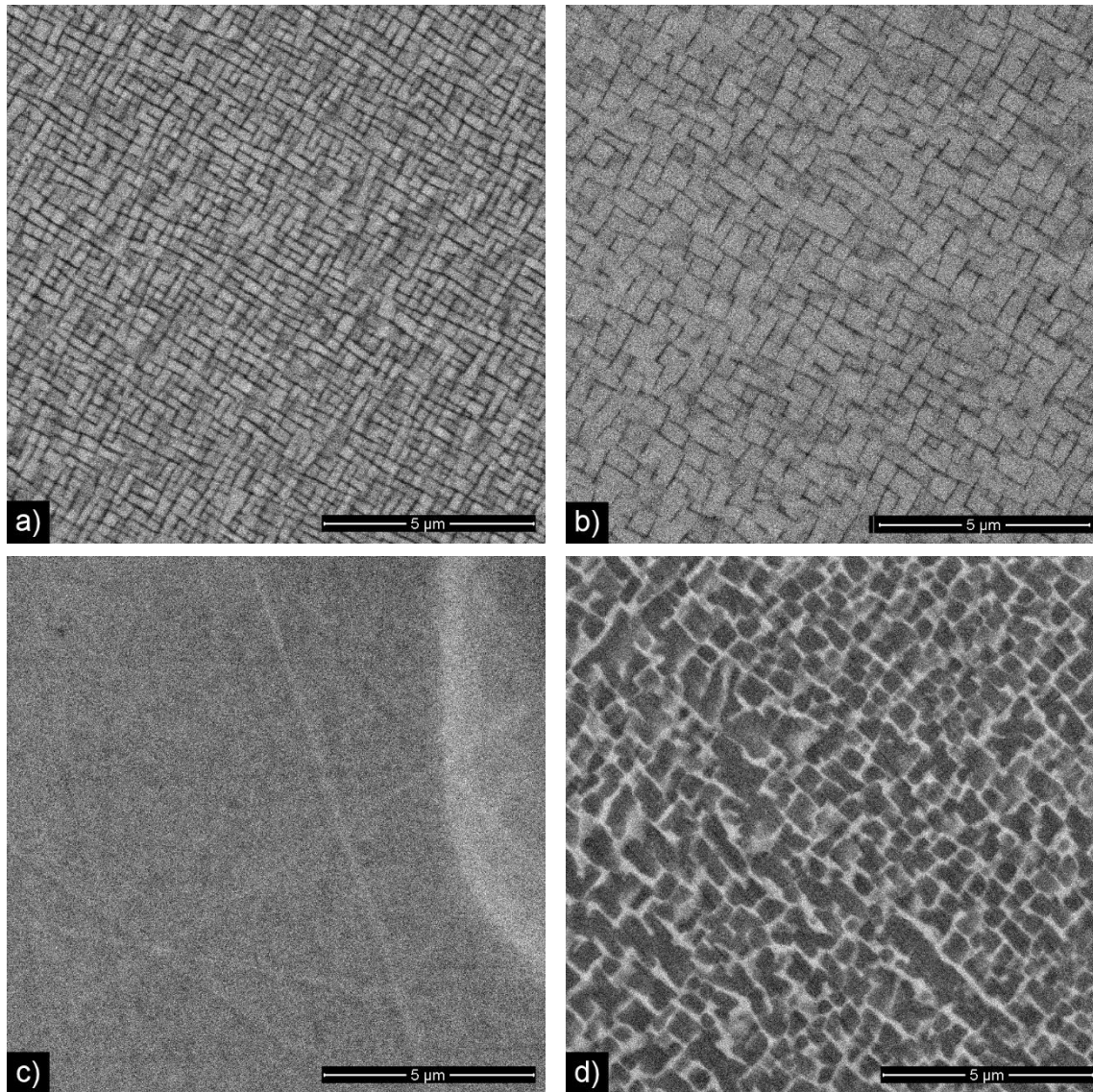


Figure 12: BSE micrographs of γ/γ' microstructure from a) Co12Al11W, b) Co15Ni12Al11W, c) Co30Ni12Al11W and d) Co45Ni12Al11W. In Co30Ni12Al11W only a single phase is observable.

the measured compositions of these phases in Co12Al11W (see Table 13). The amount of D0₁₉ and B2 qualitatively decreases with increasing nickel content which coincides with the results from [2] where these phases vanish at nickel concentrations above 50 at%.

The γ/γ' microstructure changes heavily by the substitution of cobalt with nickel which can be seen in Figure 12. Quantification of particle size does not work with this series because of the unregular shapes of γ' precipitates. But qualitatively, there is an increase in size from Co12Al11W to Co15Ni12Al11W, as expected. In Co30Ni12Al11W only a single phase can be observed, besides the additional phases in grain boundaries which

were discussed above. So, the composition probably hit near the γ' single-phase region. Another explanation could be a change of the partition coefficients which is described in [2]. As the nickel concentration increases, aluminum and tungsten increase their tendency to partition to γ' and γ , respectively. The contrast between phases depends on the average atomic number of the partitioning elements in back scattered electron micrographs which was already discussed in chapter 2.1.4. Therefore, there might be a nickel concentration where aluminum and tungsten partition in such a way that γ and γ' have the same average atomic number and cannot be distinguished visually. This theory is supported by the microstructure of Co₄₅Ni₁₂Al₁₁W where this effect might lead to an inversion of the contrast between γ and γ' .

Quantitative evaluation and comparison of γ' particle size and volume fraction does not make much sense as mentioned above. But the γ' solvus temperatures of the samples were determined and are compared to Thermo-Calc calculations in Figure 13. The expected trend of an increased solvus with higher nickel content can be seen in the experimental results but the actual values are off from the calculations by 50 to 100 °C. To verify the Thermo-Calc results which were obtained using the Zhu14 database, the γ' solvus temperature of an alloy with the same aluminum and tungsten concentrations of 12 at% and 11 at%, respectively, was calculated using the Wang17 database. The results for the nickel-free alloy differ only by 4 °C and thus are quite reliable. Nickel-containing alloys could not be calculated using the Wang17 database because only the aluminum-cobalt-tungsten system is defined in it. Two additional alloy series were calculated using the Zhu14 database which represent the upper and lower boundaries of the experimental results. The experimentally prepared samples match alloys with aluminum concentrations between 10 and 11 at% and tungsten concentrations between 9 and 10 at%. Lower aluminum and tungsten contents are reasonable since some of it is lost during the preparation and the rest might be chemically bound in stable phases like μ . From comparing the calculated results alone, it is obvious that both elements stabilize γ' .

The series with 10 at% aluminum and 10 at% tungsten was also used in calculations of the partition coefficients at 950 °C using the Zhu14 database. This composition was

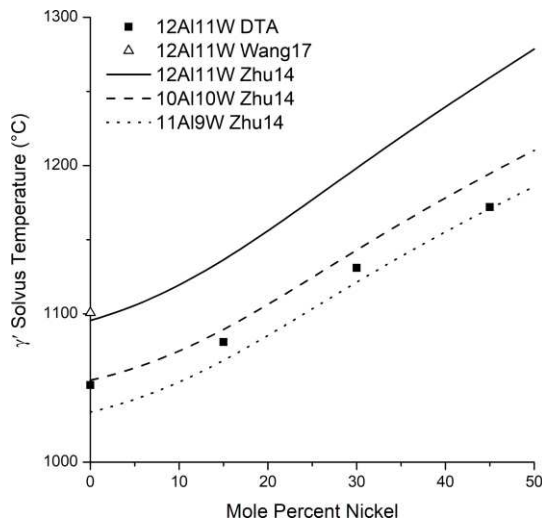


Figure 13: Measured γ' solvus temperatures of nickel variation samples (12Al11W DTA) compared to calculated results from Thermo-Calc using two databases Wang17 and Zhu14 from [33] and [12], respectively. Results from two additional alloy series are shown as well.

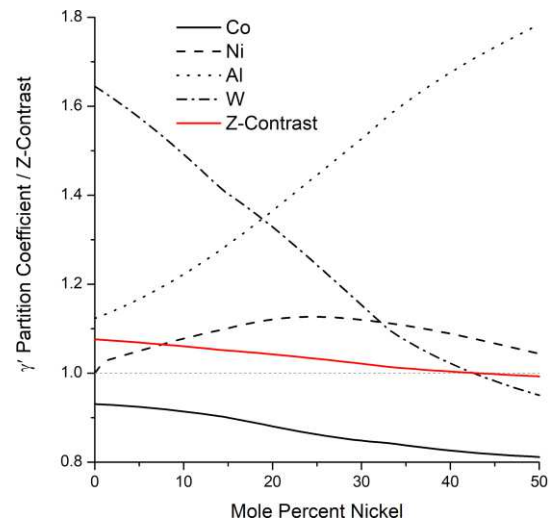


Figure 14: γ' partition coefficients from equilibrium calculations at 950 °C of a cobalt alloy with 10 at% aluminum, 10 at% tungsten and increasing nickel concentration. The Z-contrast (red) was calculated using the same calculation results.

selected because it is the best fit to the experimental results for γ' solvus temperatures. The element concentrations in γ' were divided by the element concentrations in γ and are plotted against the overall nickel concentration in Figure 14. The γ' partition coefficients for cobalt and nickel are almost constant over the calculated composition range. Aluminum tends to partition more in γ' with increasing nickel concentration and for tungsten it is the other way around. This result complies with the qualitative discussion above. The Z-contrast of γ' and γ was also derived from the calculated elemental compositions at 950 °C according to chapter 2.1.4. The expected trend of a decreasing contrast between the two phases is clearly observed and there is even an inversion by hitting below unity at around 44 at% nickel. This does not perfectly match with the experimental results since a contrast inversion is observed at around 30 at% nickel. But the model alloy with 10 at% aluminum and 10 % tungsten does not resemble the actual samples exactly which is clear from the results in Figure 13 already.

3.1.3 Cold Boat and Hukin Crucible

Figure 15 shows a common section and the γ/γ' microstructure of Co15Ni11Al9W which was prepared in a bigger batch in the cold boat and Hukin induction furnaces. Almost

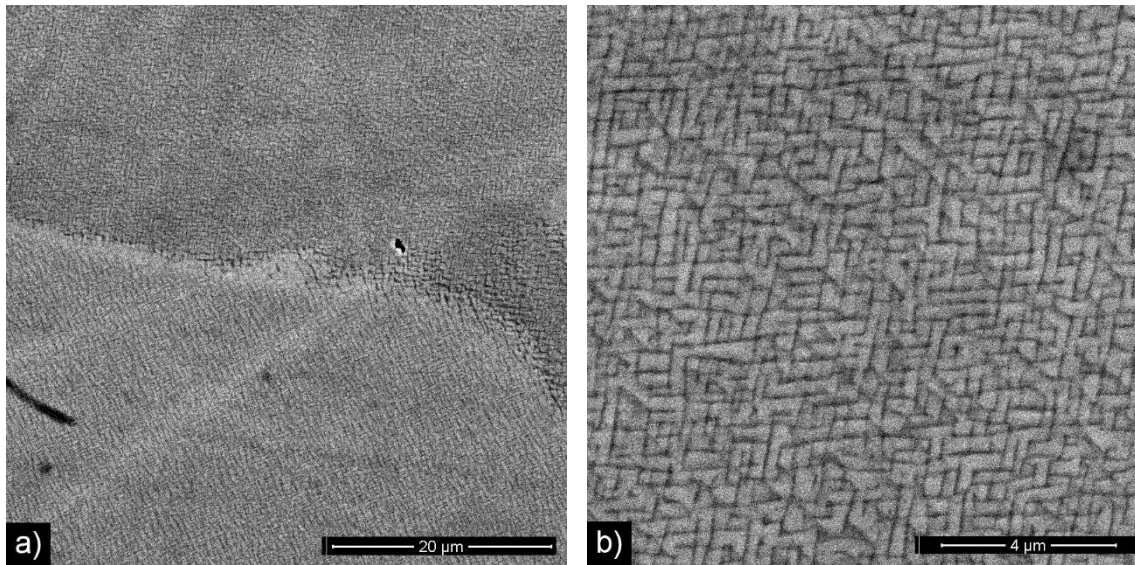


Figure 15: BSE micrographs of a) a common section and b) the γ/γ' microstructure of Co15Ni11Al9W. The black spot right from the center could be B2 (AlCo) phase.

no additional phases were observed besides small amounts of a phase with low Z-contrast which is most probably B2 phase. The microstructure very much resembles the one from Co15Ni12Al11W (see Figure 12 b)) but with slightly smaller particle size and less γ' volume fraction since the γ channels seem a little thicker. This fits the previously discussed effect of aluminum und tungsten stabilizing the γ' phase. The γ' solvus temperature was measured to be 1068 °C which almost perfectly fits the calculated result of 1066 °C in Figure 13 (11Al9W Zhu14 database at 15 at% nickel). This indicates that the composition of the sample is much less changed due to the greater batch size and it is also a sign for the correctness of the calculations.

Table 14: Carbon concentrations in wt% of nickel-free and nickel-containing alloys measured with combustion carbon analysis. The weighed-in carbon concentrations are given as table headers in wt%.

Sample	0	1	2	5	10	15	at%
	0.00	0.19	0.38	0.96	2.00	3.12	wt%
Co9Al7WxC	0.01 ± 0.00	0.03 ± 0.02	0.09 ± 0.04	0.49 ± 0.05	1.38 ± 0.19	2.12 ± 0.44	
Co30Ni9Al7WxC	0.01 ± 0.00	0.04 ± 0.01	0.15 ± 0.02	0.71 ± 0.04	1.88 ± 0.24	2.91 ± 0.20	

3.2 Influence of Carbon

The carbon concentrations of the alloys from the carbon series with and without 30 at% nickel are given in Table 14. As expected, quite a lot of carbon is lost during preparation. However, the composition of the other elements should not be affected too much from this loss because the absolute mass of carbon is quite low. The compositions of the alloys in at% (Table 15) were derived from the weighed-in amounts and the carbon concentrations from Table 14. The aluminum and tungsten concentrations did not change very much if only the carbon loss is considered. But still, more pronounced compositional changes are expected from the experience of the already-discussed alloys.

Table 15: Composition in at% of nickel-free and nickel-containing alloys derived from weighed in amounts and carbon concentrations from combustion carbon analysis.

Sample	C target	C	Al	Co	Ni	W
Co9Al7W _x C	0	0.1	9.0	84.0	–	7.0
	1	0.2	9.1	83.7	–	7.1
	2	0.5	9.1	83.3	–	7.1
	5	2.6	9.2	81.0	–	7.2
	10	7.1	9.3	76.4	–	7.2
	15	10.7	9.5	72.5	–	7.4
Co30Ni9Al7W _x C	0	0.1	9.0	54.0	30.0	7.0
	1	0.2	9.1	53.8	29.9	7.1
	2	0.8	9.1	53.4	29.6	7.1
	5	3.7	9.1	51.5	28.6	7.1
	10	9.5	9.1	47.9	26.6	7.0
	15	14.1	9.1	44.8	24.9	7.1

Micrographs of the nickel-free alloys of the carbon series are shown in Figure 16 with a common section and an inlet with the γ/γ' or γ/κ microstructure. The sample with 0.2 at% carbon already consists of small amounts of an additional white phase which becomes more with increasing carbon concentration. EDS identified the phase as η (M_6C or $M_{12}C$) or tungsten carbide (WC) because of the high carbon and tungsten concentrations (see Table 16). Graphite is observed in the sample with 10.7 at% carbon.

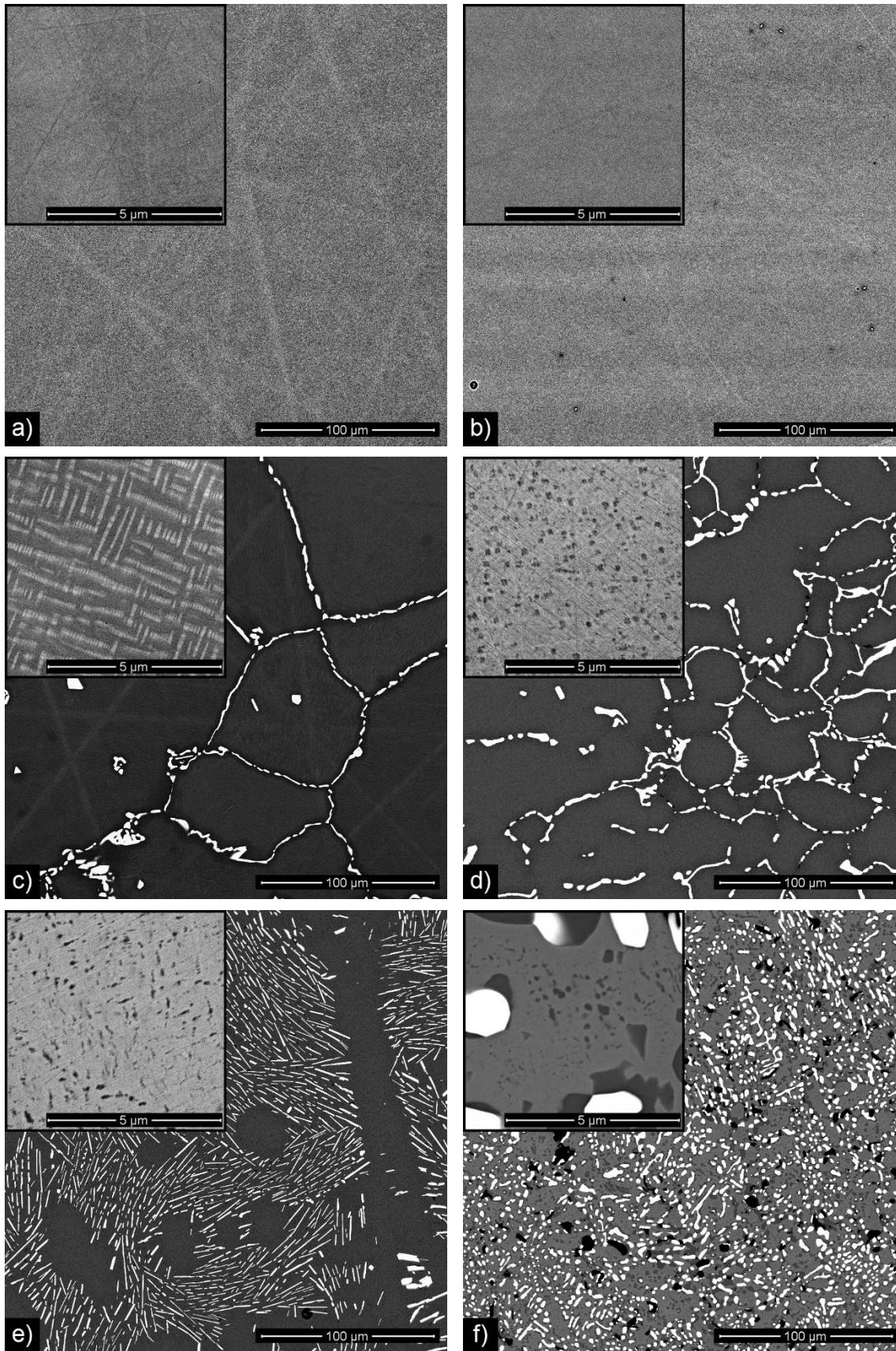


Figure 16: BSE micrographs of $\text{Co}_9\text{Al}_7\text{W}_x\text{C}$ with a) 0.1, b) 0.2, c) 0.5, d) 2.6, e) 7.1 and f) 10.7 at% carbon. The γ/γ' or γ/κ microstructure is shown as inlet in the top left of each image. Additional phases are η or WC and graphite in white and black, respectively.

Table 16: EDS measured composition (TEAM™ quantification) of η in at% in nickel-free samples from carbon series. Quantification was carried out neglecting carbon, but a peak is clearly visible in measurement spectra. The carbides are guessed from the tungsten to cobalt ratios, which is unity in $M_{12}C$ [61].

Co9Al7WxC	Al	Co	W	Carbide
0.2 at% C	1.8 ± 0.4	60.3 ± 3.7	38.0 ± 4.0	$M_6C/M_{12}C$
0.5 at% C	5.2 ± 0.5	48.5 ± 0.5	46.3 ± 0.8	$M_{12}C$
2.6 at% C	3.7 ± 0.7	51.6 ± 0.7	44.8 ± 0.9	$M_{12}C$
7.1 at% C	2.2 ± 0.5	26.7 ± 5.1	71.1 ± 5.3	M_6C/WC
10.7 at% C	2.7 ± 0.5	54.0 ± 1.0	43.4 ± 1.2	$M_{12}C$

γ/γ' microstructure is only visible in the sample with 0.5 at% carbon and is it not clear why the samples with lower carbon concentrations did not form γ' . Carbon might has a stabilizing effect on the formation of γ' as concluded in [10]. With higher carbon concentrations, γ' incorporates carbon into its structure and changes from $L1_2 Co_3(Al,W)$ to $E2_1 Co_3AlC$ which is also denoted as κ . Very little tungsten is dissolved in this phase which was measured with EDS (see Table 17). It could be reasoned that most of the tungsten must be consumed by formation of η and WC before κ becomes stable. Carbon content was not quantified but the amount of cobalt is three to four times the amount of aluminum which backs up the identification of κ with EDS. The amount of this phase increases with carbon concentration and forms quite big areas in the sample with 10.7 at% carbon.

Table 17: EDS measured composition (TEAM™ quantification) of κ in at% in nickel-free samples of carbon series. Quantification was carried out neglecting carbon, but a peak is clearly visible in measurement spectra.

Co9Al7WxC	Al	Co	W
2.6 at% C	22.1 ± 0.8	76.7 ± 0.9	1.3 ± 0.2
7.1 at% C	22.7 ± 1.2	76.5 ± 1.6	0.8 ± 0.7
10.7 at% C	23.2 ± 0.4	76.0 ± 0.4	0.8 ± 0.1

The micrographs of the nickel-containing samples from the carbon series are shown in Figure 17 again with a common section of the samples and an inlet with the γ/γ' or γ/κ

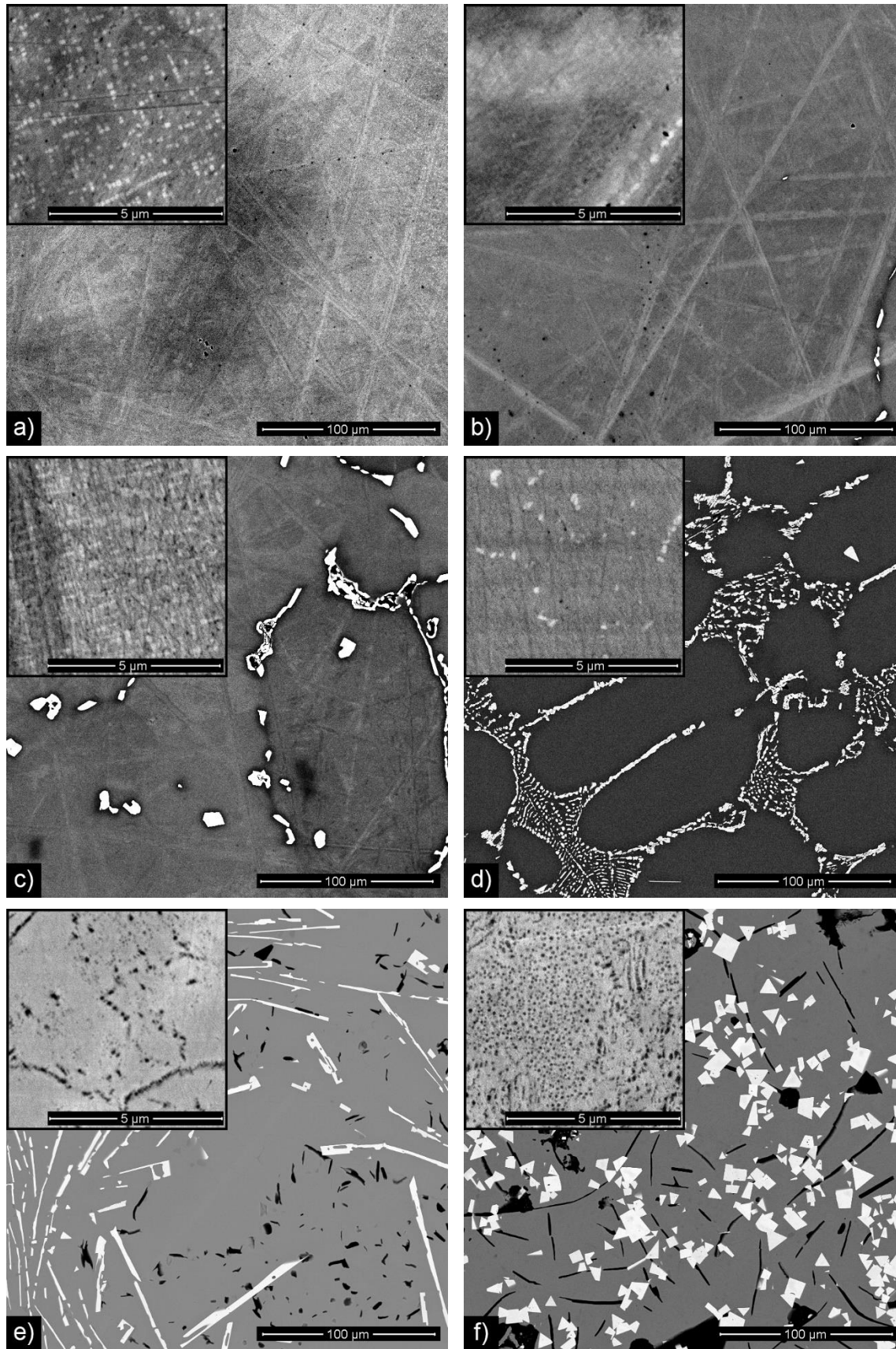


Figure 17: BSE micrographs of $\text{Co}_{30}\text{Ni}_9\text{Al}_7\text{W}_x\text{C}$ with a) 0.1, b) 0.2, c) 0.8, d) 3.7, e) 9.5 and f) 14.1 at% carbon. The γ/γ' or γ/κ microstructure is shown as inlet in the top left of each image. Additional phases are η or WC and graphite in white and black, respectively.

microstructure. Analogous to the nickel-free samples, carbides are already observable from the lowest carbon concentration of 0.2 wt% and their amount increases the more carbon is added. The shape of the white phase changes from nodular to blocky at 9.5 at% carbon. With the results from EDS in Table 18 it is very likely that $M_{12}C$ changes to M_6C and further changes to WC with increasing carbon concentrations. Graphite is observed in the two most carbon-rich samples. Together with the results from the nickel-free samples, graphite begins to form in a carbon range between 7.1 and 9.5 at% if an influence of nickel concentration is neglected.

Table 18: EDS measured composition (TEAM™ quantification) of η and WC in at% in nickel-containing samples from carbon series. Quantification was carried out neglecting carbon, but a peak is clearly visible in measurement spectra. The carbides are guessed from tungsten to cobalt/nickel ratios, which is unity in $M_{12}C$ and big in WC [61].

Co30Ni9Al7WxC	Al	Co	Ni	W	Carbide
0.2 at% C	2.8 ± 0.5	36.7 ± 0.5	12.6 ± 0.3	47.9 ± 0.4	$M_{12}C$
0.8 at% C	3.0 ± 0.2	37.1 ± 0.3	12.1 ± 0.3	47.8 ± 0.6	$M_{12}C$
3.7 at% C	2.8 ± 0.3	36.8 ± 0.5	12.6 ± 0.4	47.9 ± 0.4	$M_{12}C$
9.5 at% C	2.0 ± 0.2	12.4 ± 0.7	7.8 ± 0.6	77.8 ± 1.2	M_6C/WC
14.1 at% C	2.1 ± 0.3	5.5 ± 2.3	4.2 ± 1.0	88.2 ± 3.1	WC

γ' is observable until a carbon concentration of 3.7 at% which is way higher than in the nickel-free samples where this phase is not stable at 2.6 at% carbon already. Again, as in the discussion in chapter 3.1, a stabilization of γ' with nickel is observed. From 9.5 at% carbon, κ can be observed which was identified using EDS (see Table 19). Here it is quite dispersed and does not form big areas even at a carbon concentration of 14.1 at%.

Table 19: EDS measured composition (TEAM™ quantification) of κ in at% in nickel-containing samples of carbon series. Quantification was carried out neglecting carbon, but a peak is clearly visible in measurement spectra.

Co30Ni9Al7WxC	Al	Co	Ni	W
9.5 at% C	20.1 ± 0.6	42.5 ± 0.6	37.0 ± 0.7	0.5 ± 0.0
14.1 at% C	22.8 ± 0.3	39.9 ± 1.2	37.1 ± 0.9	0.3 ± 0.0

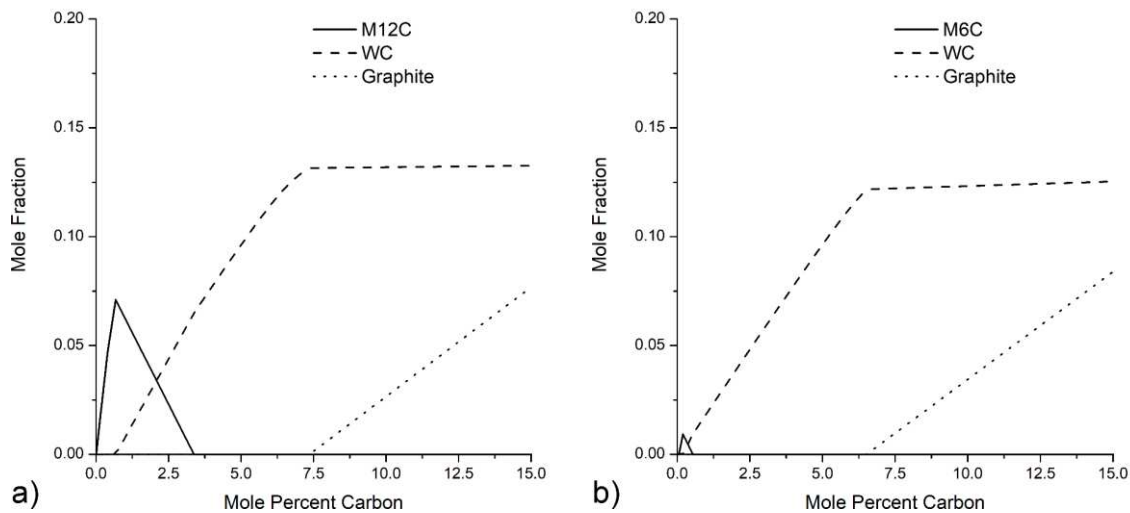


Figure 18: Calculated present phases in a) nickel-free carbon series and b) carbon series with 30 at% nickel at 950 °C using Thermo-Calc with TCFE9/TCCC1 database. The amount of γ is the rest to unity.

Thermodynamic calculations of alloys with 9 at% aluminum and 7 at% tungsten, and carbon concentration from 0 to 15 at% at 950 °C were carried out using Thermo-Calc with the TCFE9 and TCCC1 databases. The amount of present phases were plot against the carbon content which is shown in Figure 18 a) and b) for nickel-free alloys and 30 at% nickel, respectively. The calculations yielded the same results for both databases which indicates that the same thermodynamic assessments were used. This leaves the results quite doubtful because aluminum was not defined while using TCCC1 which means that this element does not influence the calculated phase equilibria at all. This also becomes apparent when the compositions of the phases are derived from the calculation results which show that the γ phase constantly has an aluminum concentration of 9 at%. Still, the experimental results for the nickel-free alloys show some similarities to the calculations. M₁₂C was observed in samples with up to 2.6 at% C and at 7.1 at% blocky WC is identified (see Figure 16 and Table 16) which coincides with the curves in Figure 18. At higher carbon concentrations M₁₂C becomes stable again which might be due to the interaction with κ . From the inlet in Figure 16 f) it seems like κ is formed on the edges of WC which leads to carbon-depletion and transformation to M₁₂C. Graphite is predicted to form at carbon contents above 7.5 at% which is also observed in the experimental results. γ' and κ are missing completely which is not surprising because they are not described in the underlying thermodynamic assessments of the used databases.

The calculated results in the nickel-containing carbon series differ severely from the experimental observations. With EDS measurements the carbides were identified to be $M_{12}C$ for the samples with up to 3.7 at% carbon (see Table 18) since the ratio between tungsten and cobalt/nickel is unity which is an indication that this phase is present [61]. It is known that the description of cemented carbides with a mixture of cobalt and nickel is erroneous in thermodynamic assessments which were used in TCFE9. This was partially corrected in [26] and these parameters were used in Zhou16 database but, unfortunately, repeating the above calculations with this database did not affect the results. The formation of WC according to the calculations might be predicted correctly since this phase becomes stable between 3.7 and 9.5 at% carbon. The calculated critical carbon concentration for the formation of graphite is a little lower for the nickel-containing alloys. This is reasonable since nickel has a higher tungsten solubility than cobalt [25, 62] and with more tungsten in γ , less is available to consume carbon through the formation of carbides.

The cemented carbides consisting of 70 wt% WC and 30 wt% Co9Al7W as binder phase and with different amounts of additional carbon are shown in Figure 19. Both samples should be right inside the carbon window as predicted from thermodynamic calculations using the TCFE9 database while considering some carbon loss. In the alloy with 0.4 wt% additional carbon only γ and WC are observed in most regions of the sample (see Figure 19 a)). The extra addition of as little as 0.2 wt% carbon to this alloy leads to the formation of another phase inside the binder region. As seen in Figure 19 b), this phase very much resembles κ of the above discussed samples. Solution heat treatment of the alloy at 1300 °C leads to grain refinement of κ after 3 h and subsequent dissolution after 24 h. This coincides with the proposed solvus temperature of around 1300 °C [10]. From these results it seems like the stability region of κ begins somewhere inside the carbon window of the cemented carbide.

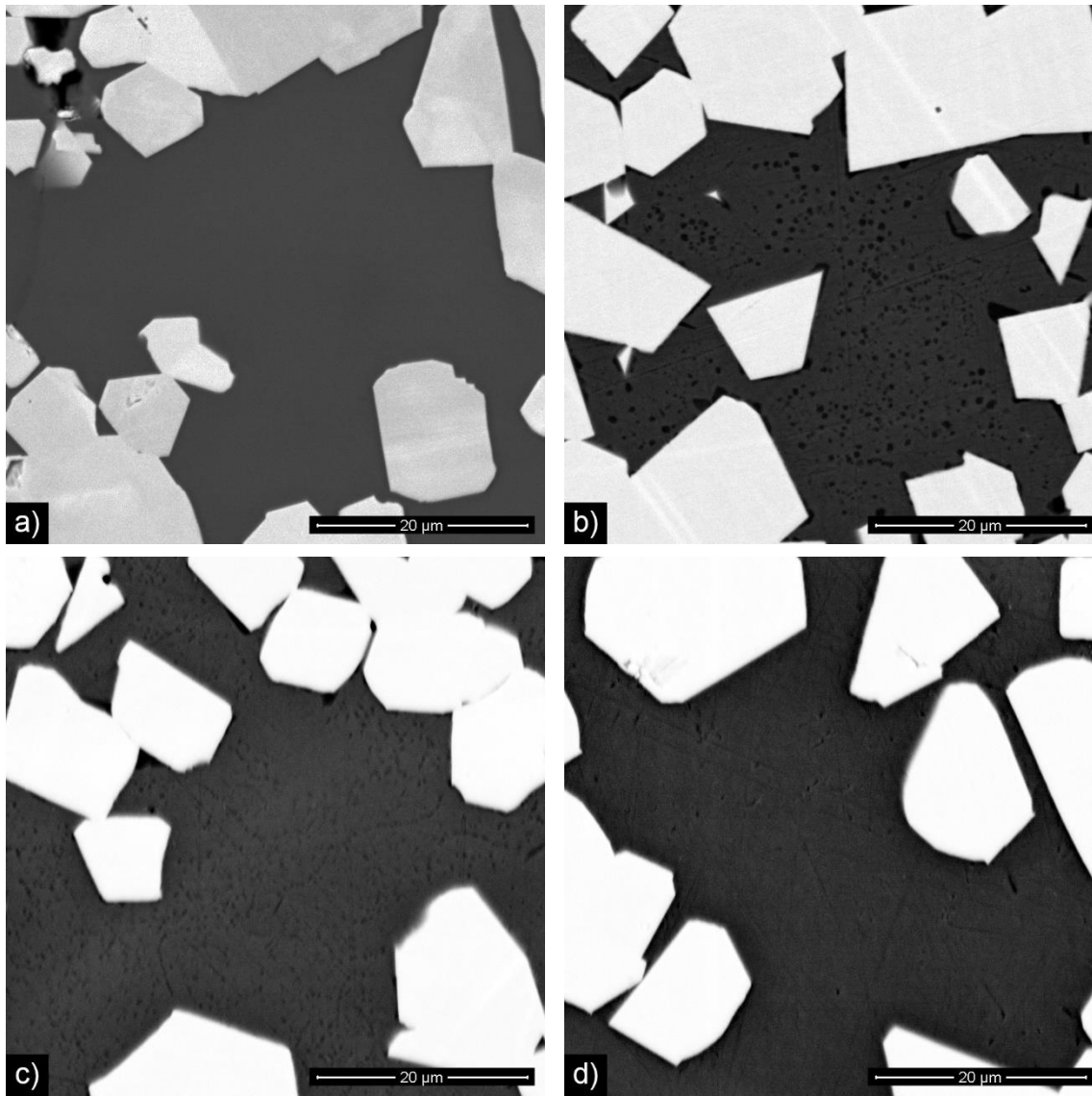


Figure 19: BSE micrographs of a) 70WC-Co9Al7W-0.4C and b-d) 70WC-Co9Al7W-0.6C in different preparation conditions: a-b) as-cast, after solution heat treatment at 1300 °C for c) 3 h and d) 24 h.

3.3 Cemented Carbides via Infiltration

Common sections of the cemented carbides which were prepared through infiltration of the samples from chapters 2.2.1 and 3.1.1 are shown in Figure 20. The images were taken from regions in the top of the cemented carbides because the binder undergoes pronounced compositional changes as it infiltrates into the tungsten carbide powder. This will be discussed after the presentation of the samples. The cemented carbide with Co30Ni11Al7W3Ta is the only one with the anticipated γ/γ' microstructure inside the binder regions. Infiltration of Co9Al8W2Ta, Co10Al10W or Co30Ni14Al6W does not allow for precipitation of γ' with the conducted preparation steps. There must be a

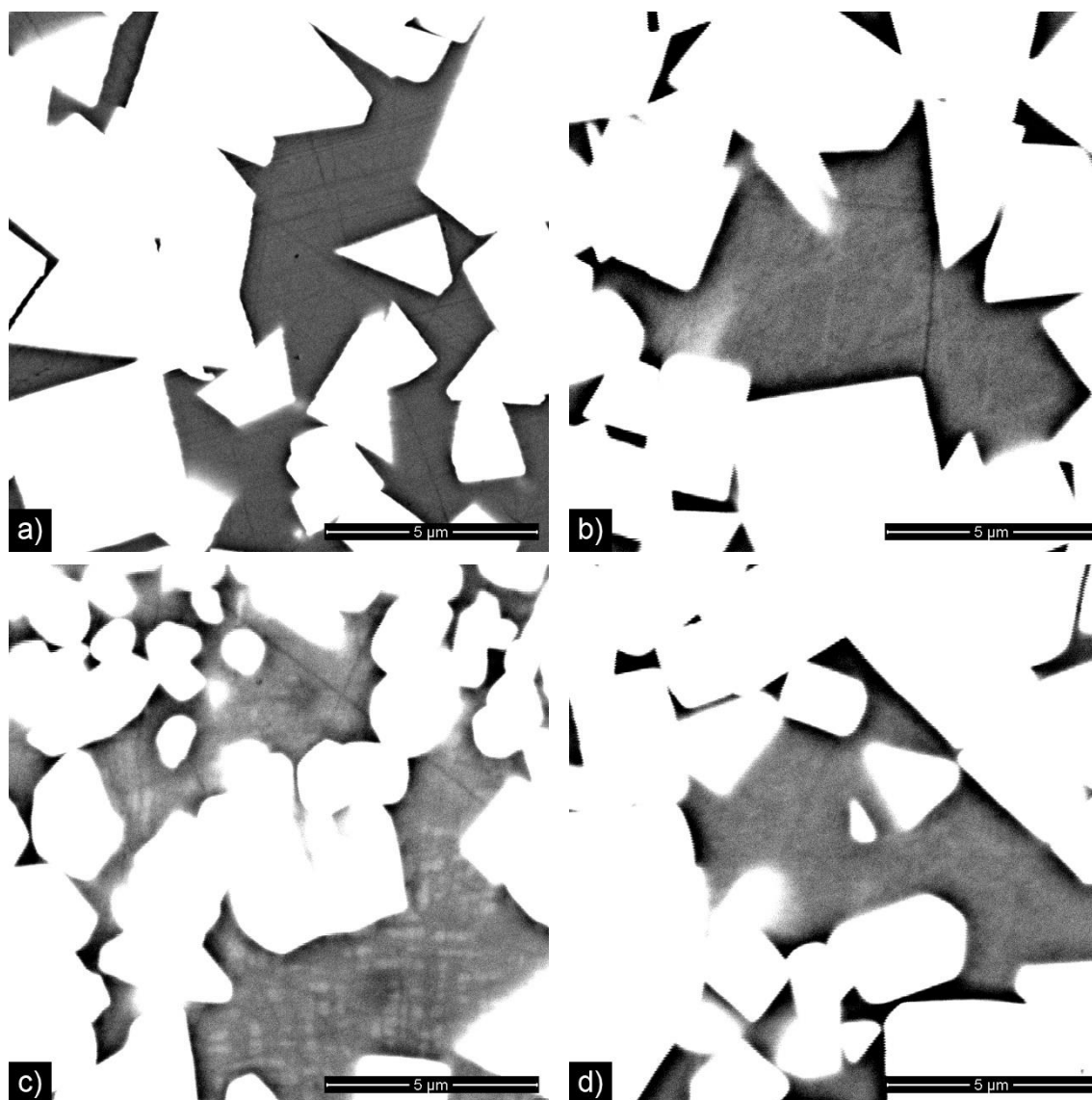


Figure 20: BSE micrographs from top of infiltrated and heat-treated cemented carbides with a) $\text{Co}_9\text{Al}_8\text{W}_2\text{Ta}$, b) $\text{Co}_{10}\text{Al}_{10}\text{W}$, c) $\text{Co}_{30}\text{Ni}_{11}\text{Al}_7\text{W}_3\text{Ta}$ and d) $\text{Co}_{30}\text{Ni}_{14}\text{Al}_6\text{W}$ binder phase.

compositional dependency which is most probably the presence of nickel as it was found to stabilize γ' in all previously discussed chapters. Tantalum also showed these effects and since no precipitates can be seen in Figure 20 d) although nickel is present in the sample, one could reason that tantalum is mandatory as well. But $\text{Co}_{30}\text{Ni}_{14}\text{Al}_6\text{W}$ has a way lower overall content of refractory elements which showed to reduce γ' stability.

The necessity of nickel for the formation of γ' in cemented carbide binder phase is confirmed in Figure 21. The superalloys from the nickel variation which were described and discussed in chapters 2.2.2 and 3.1.2 were infiltrated for preparation of these cemented carbides. All nickel-containing samples consist of γ/γ' microstructure but each look

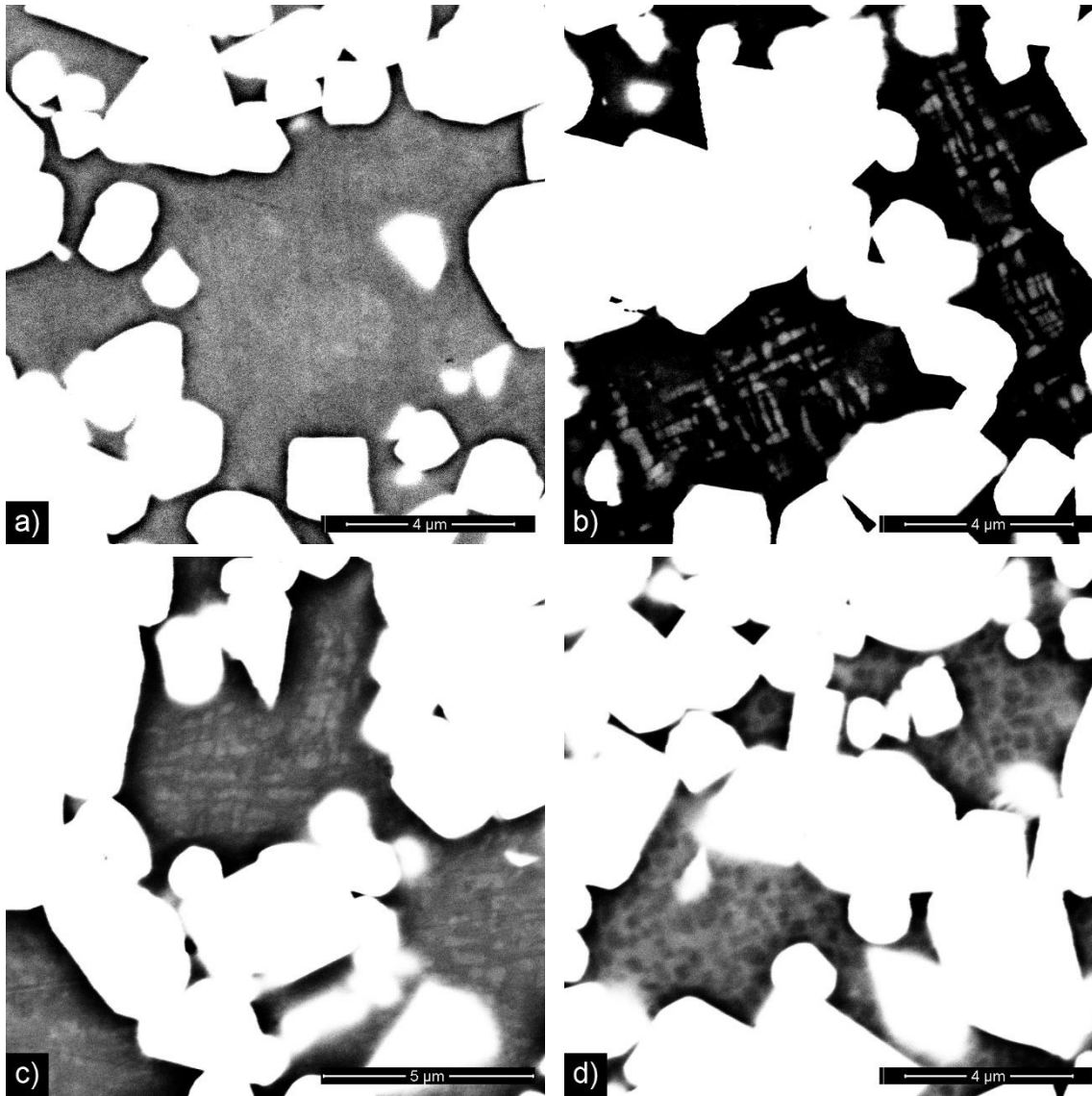


Figure 21: BSE micrographs from top of infiltrated and heat-treated cemented carbides with a) Co12Al11W, b) Co15Ni12Al11W, c) Co30Ni12Al11W and d) Co45Ni12Al11W binder phase.

different. Like in the discussion of the plain superalloys, a change in Z-contrast can be observed. With increasing nickel content, the contrast of γ' decreases and is inverted in the sample with 45 at% nickel again. The most regular shaped precipitates are found in the cemented carbide with Co15Ni12Al11W as binder phase. It is the only sample where the γ/γ' microstructure can be found practically everywhere. All other samples contain regions with varying amounts of differently shaped precipitates. In Figure 21 b) it also seems like the precipitates are formed from a homogenous binder phase since the tungsten carbide boundaries are γ' -free. Whereas in Figure 21 c) and d) it seems like the superalloy and the hard phase were just smudged together.

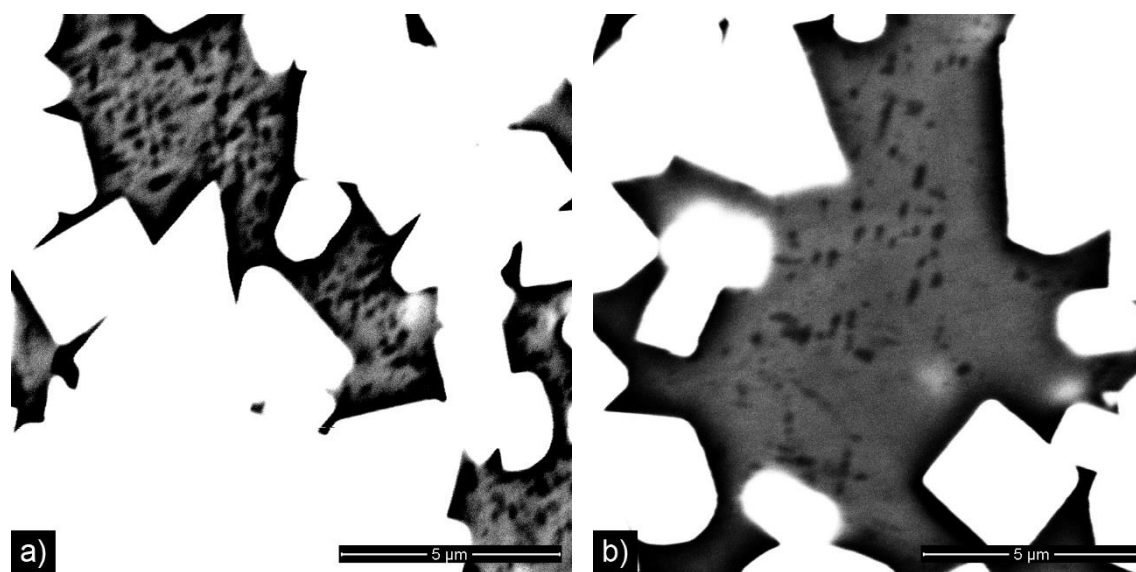


Figure 22: BSE micrographs from bottom of infiltrated and heat-treated cemented carbides with a) $\text{Co}_{30}\text{Ni}_{11}\text{Al}_7\text{W}_3\text{Ta}$ and b) $\text{Co}_{45}\text{Ni}_{12}\text{Al}_{11}\text{W}$ binder phase.

As already mentioned, the binder microstructure is not the same throughout most of the samples. The images in Figure 20 and Figure 21 were all taken from a region near to where the superalloy rests on top of the tungsten carbide powder before infiltration. It is where the liquid phase first has contact to the carbides and the phase reactions will be limited. But as the superalloy progresses through the powder, more compositional changes will occur. The binder microstructure from the bottom of two previously discussed cemented carbides is shown in Figure 22. There, κ carbides are found to precipitate inside the binder phase. In most of the samples with γ/γ' binder microstructure a gradual change from top to bottom is observed where γ' vanishes to leave single-phase γ and eventually κ will precipitate. This goes together with a decrease in tungsten concentration from top to bottom. These findings match with the discussion in chapter 3.2 where tungsten is reduced in γ through carbide formation before κ becomes stable.

The compositional changes of the binder from top to bottom in cemented carbides were analyzed using EDS measurements. In most of the cases there is an increase in aluminum content and a decrease in tungsten content in the vertical direction through the sample. Usually, this distribution is not eliminated through heat treatments and remains qualitatively the same. Figure 23 a) and b) show this distribution for the sample with $\text{Co}_{30}\text{Ni}_{11}\text{Al}_7\text{W}_3\text{Ta}$ as binder phase before and after heat treatment, respectively. On the

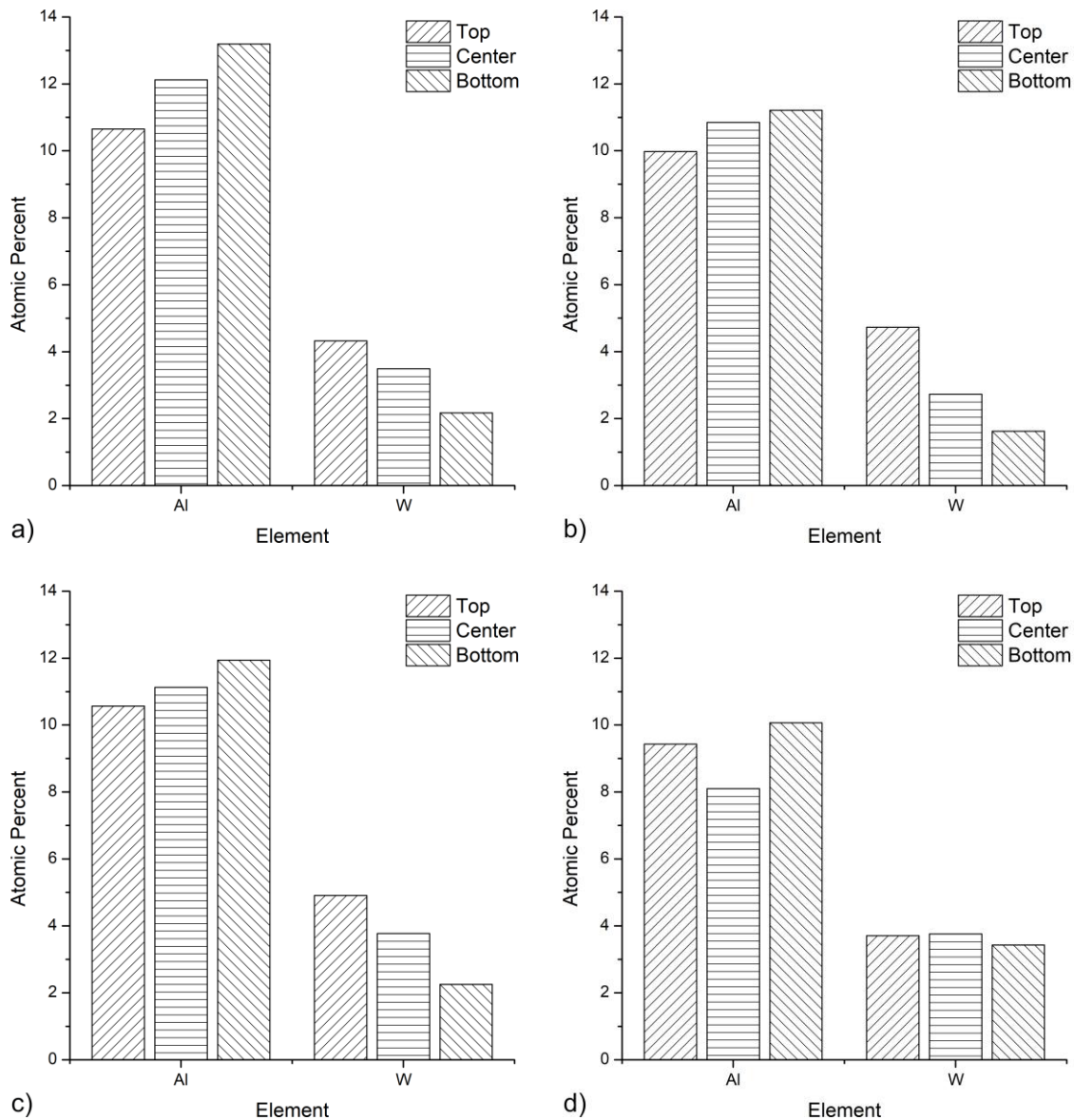


Figure 23: EDS measured aluminum and tungsten concentrations (TEAM™ quantification) in samples with a) & b) $\text{Co}_{30}\text{Ni}_{11}\text{Al}_{7}\text{W}_{3}\text{Ta}$ and c) & d) $\text{Co}_{15}\text{Ni}_{12}\text{Al}_{11}\text{W}$ as binder phase. a) & c) as-cast and b) & d) after solution and precipitation heat treatment.

other hand, the cemented carbide where $\text{Co}_{15}\text{Ni}_{12}\text{Al}_{11}\text{W}$ was infiltrated does show a homogenization of the tungsten concentration after heat treatment as seen in Figure 23 c) and d). This is also the only sample where γ/γ' binder microstructure is not locally restricted as mentioned above.

These observations are judgeable qualitatively only because the measurement errors are relatively high. Also, the absolute results are presumably erroneous as the quantification is not reliable (see chapter 2.1.4). However, qualitatively similar results were achieved from reproducing the samples which are shown in Figure 20. Preparation of cemented

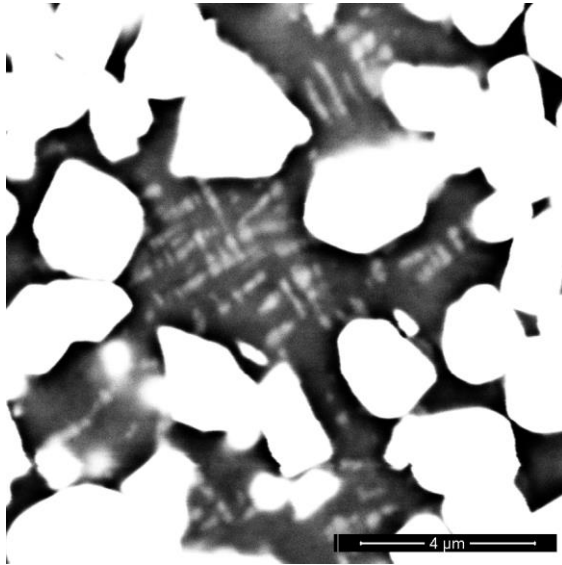


Figure 24: BSE micrograph of infiltrated and heat-treated cemented carbide with Co15Ni10Al9W binder phase.

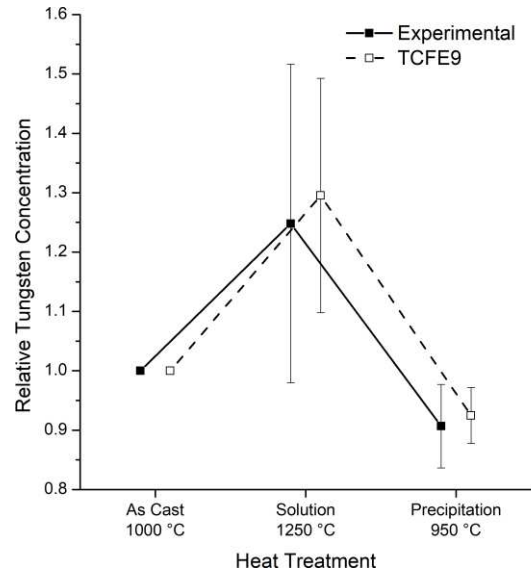


Figure 25: Relative tungsten concentration in binder averaged over all cemented carbides of the nickel variation and calculated with similar model samples using the TCFE9 database. The symbols are offset from each other for better readability.

carbides with the alloys from nickel variation was not conducted a second time. But Co15Ni10Al9W from chapters 2.2.4 and 3.1.3 was used for an infiltration experiment. The outcome in Figure 24 is very similar to the cemented carbide where Co15Ni12Al11W was used as binder phase (see Figure 21 b)) and again, the anticipated microstructure was found throughout the whole sample. Regarding these results, a cobalt alloy with 15 at% nickel, 10 to 12 at% aluminum and 9 to 11 at% tungsten is most favorable in producing a cemented carbide with γ/γ' binder microstructure.

The average tungsten concentration in the binder phase of cemented carbides changes with heat treatments. These values were derived from the above described composition distribution measurements of the nickel variation samples in three heat treatment conditions: as-cast, solution heat treated, and precipitation heat treated. The relative value to the as-cast condition was calculated and averaged over all four samples. As expected, the tungsten concentration rises after solution heat treatment because more of the refractory element is soluble at higher temperatures. The values deviate from each other quite a lot since the tungsten solubility and its temperature dependency are functions of the nickel concentration as well [25, 62]. After precipitation heat treatment, the relative tungsten concentration drops below one which means that tungsten leaves γ to form

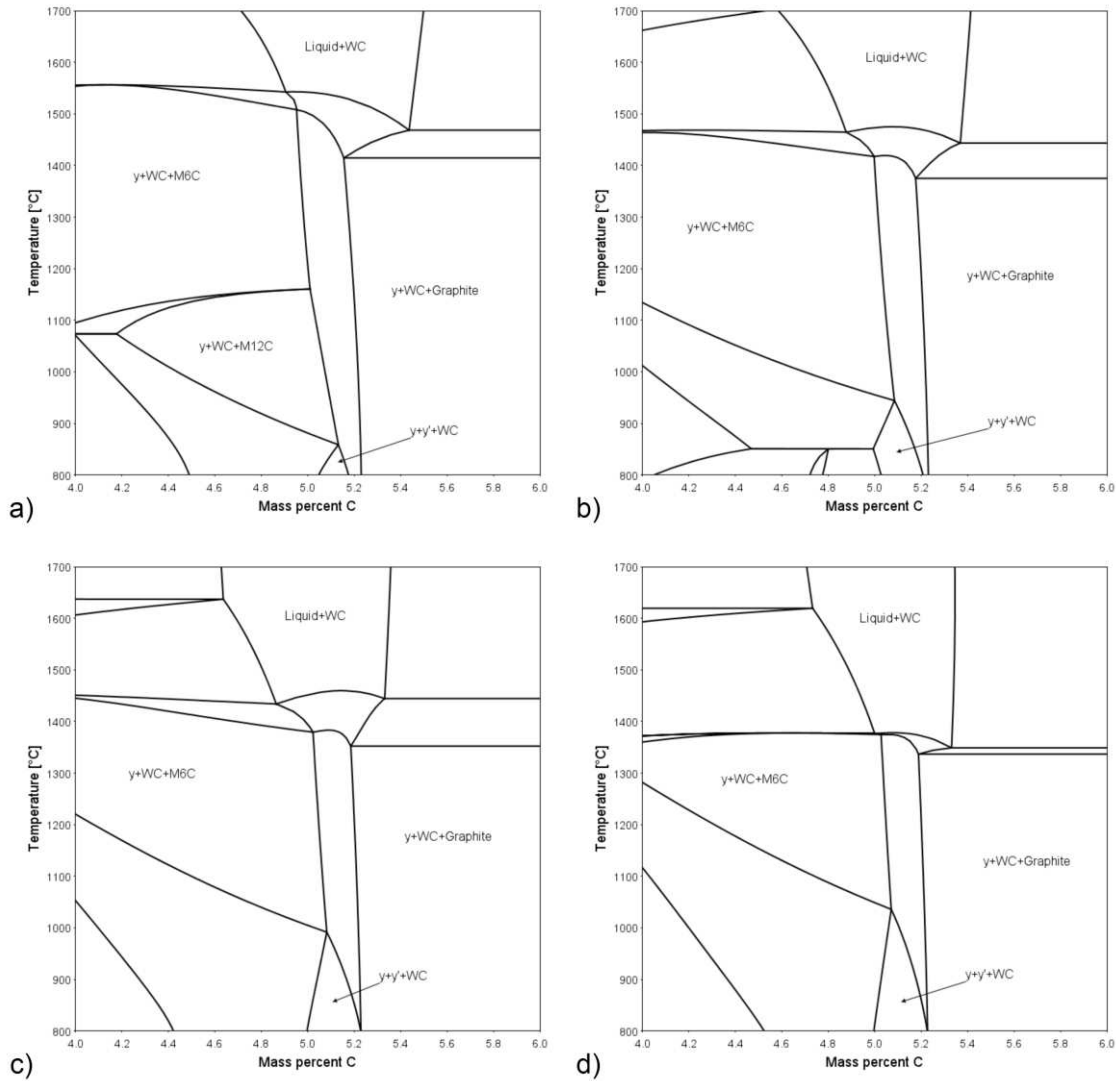


Figure 26: Calculated phase diagrams of cemented carbides with 20 wt% superalloys as binder phase. The composition of the binder is 10 at% aluminum, 10 at% tungsten, a) 0 at%, b) 15 at%, c) 30 at%, d) 45 at% nickel and cobalt for balance. Two databases, TCFE9 and Zhu, were combined for the calculation with Thermo-Calc.

other phases, presumably WC and η . Additionally, thermodynamic calculations using the TCFE9 database were carried out for comparison. The 20 wt% binder phase of the model cemented carbides were four cobalt alloys with 0, 15, 30 and 45 at% nickel, 10 at% aluminum and 10 at% tungsten which should resemble the real samples as much as possible. The equilibria at 1000, 1250 and 950 °C were calculated for the as-cast, solution heat treated, and precipitation heat treated conditions, respectively. 1000 °C for the as-cast condition was chosen because it was assumed that the diffusion of elements stops at this point after infiltration and relatively fast cooling. The measurement and calculation results are plot in Figure 25 and agree very well with each other.

The influence of nickel on the formation of γ/γ' binder microstructure in cemented carbides was also investigated using thermodynamic calculations. For this, TCFE9 and Zhu14 databases were combined because only the latter one is able to properly describe the γ' phase but does not include thermodynamic assessments with carbon. The phases which are described in the aluminum-cobalt-nickel-tungsten system were disabled from the TCFE9 database and replaced by the ones from Zhu. This has some notable downsides because realistically carbon would dissolve into γ to a certain degree which would alter the phase equilibria slightly [63, 64]. Also, each database is optimized for its own use case and some phases might interact unexpectedly. $M_{12}C$ from TCFE9 had to be removed from the calculations of nickel-containing cemented carbides because there were incorrect interactions with the phases from Zhu. Cobalt alloys with 10 at% aluminum, 10 at% tungsten and 0 to 45 at% nickel were used as 20 wt% binder phase of the model cemented carbides. The results are shown in Figure 26 where the carbon window between 4 and 6 wt% carbon of each of the four samples is displayed. These are in very good agreement with the experimental results in Figure 21 since all nickel-containing samples have a γ , γ' and WC three-phase region at 950 °C inside the carbon window. Reasoning from the phase diagram in Figure 26 a) a precipitation heat treatment below 850 °C might would have delivered γ/γ' binder microstructure in this sample as well. The stabilization of γ' through nickel-addition is again observed in the calculated results since the three-phase region gets bigger with increasing nickel concentration. The destabilization of γ' through carbon which was observed in chapter 3.2 can also be seen since the upper boundary of the three-phase region decreases with increasing carbon content in each sample. Only the formation of κ is missing which is not surprising because this phase is not described in any of the underlying thermodynamic assessments. As already mentioned above, the description of cemented carbides with binder phases which contain both cobalt and nickel is erroneous. This can be seen in the decreasing solidus temperature with increasing nickel content, because it should increase instead [15].

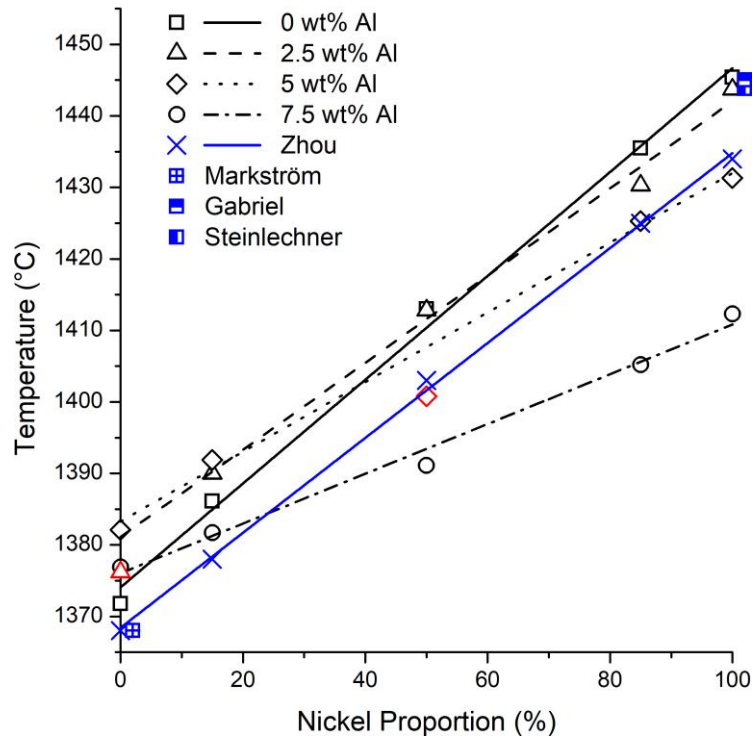
3.4 Cemented Carbides via DTA

3.4.1 Solidus Temperature

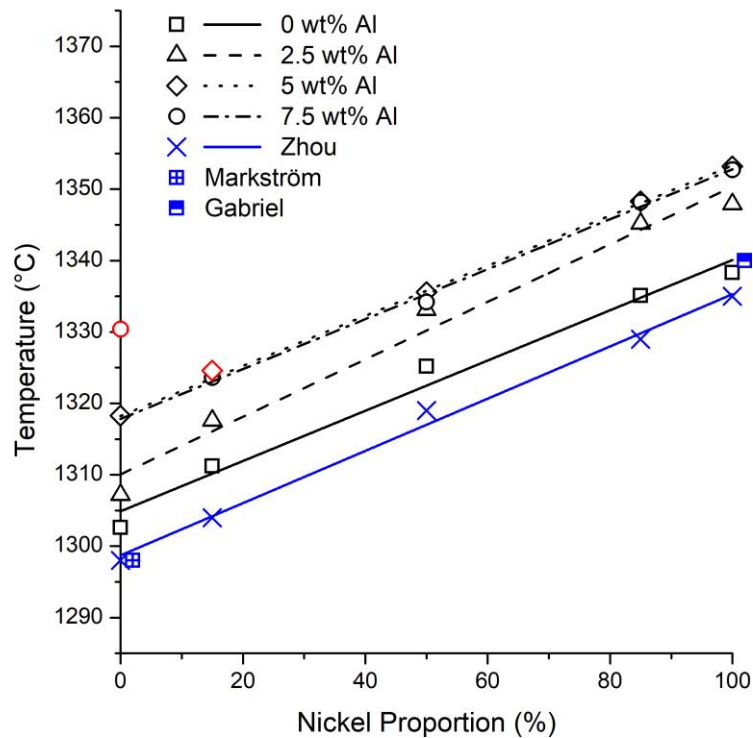
The temperature of liquid formation was determined from DTA heating curves which are shown together with the cooling curves for all 40 samples in the appendix in chapter 6.1.2. “h” and “c” indicate heating and cooling, respectively.

The results are plot against the nickel proportion of the binder (fraction of nickel in the cobalt-nickel ratio) in Figure 27 a) and b) for the tungsten- and carbon-rich samples, respectively. Red colored datapoints are presumably wrong because oddly shaped DTA signals occur at the solidus temperature of these samples (see example in Figure 28). These are two overlapping peaks which cannot be separated since there is a complex relationship between them [65]. Therefore, they are excluded from further discussion. Each series with different aluminum content was linearly fit by least-squares regression omitting the rejected results. But since the changes in temperature are not expected to depend linearly on nickel, the curves are discussed qualitatively only. The solidus temperature is elevated with increasing nickel proportion in all binder series and the rate of this effect is described by the slope of the linear fit curves. It stays almost constant for the carbon-rich samples, and the addition of aluminum always increases the temperature of liquid formation. In the samples with excess tungsten on the other hand, the slope becomes less steep the more aluminum is added. This leads to an inversion of the trend at higher nickel proportions where aluminum addition decreases the solidus temperature. The inversion occurs at the intercept of the 0 wt% aluminum line with the other lines, i.e. at around 60, 35 and 5 % nickel proportion for 2.5, 5 and 7.5 wt% binder aluminum concentration, respectively. For the carbon-rich series there is no change of the solidus temperature from 5 to 7.5 wt% aluminum and the fit curves are identical in Figure 27 b).

The results of the series with 0 wt% aluminum are further compared to [26] where very similar experiments were carried out. All measured solidus temperatures are higher in the present work, but the deviations are below 10 K for all carbon-rich samples and for the samples with low nickel content in the tungsten-rich series. Additional literature



a)



b)

Figure 27: Solidus temperatures of cemented carbides with different cobalt-nickel-aluminum binder and a) excess tungsten (4.23 wt% C), and b) excess carbon (5.84 wt% C). The red colored datapoints were excluded from further discussion since the solidus temperature could not be evaluated validly. The literature data is colored in green and taken from [26], [38] and [66] for Zhou, Markström and Gabriel, respectively. Steinlechner is from unpublished work carried out at the Institute of Chemical Technologies and Analytics at TU Wien where a conventionally prepared cemented carbide with 20 wt% nickel as binder was analyzed.

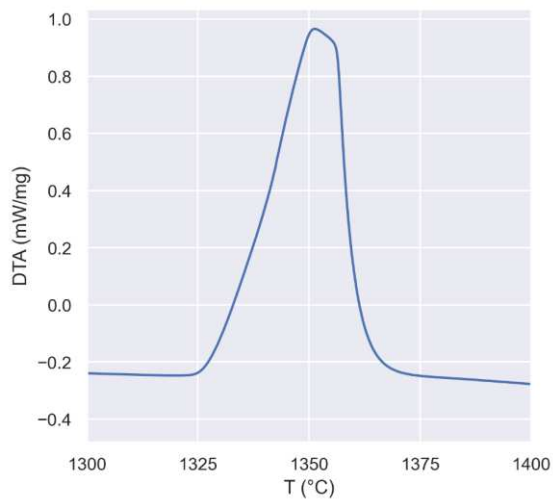


Figure 28: Oddly shaped DTA signal at the formation of liquid phase in WCCo0075C from two overlapping peaks.

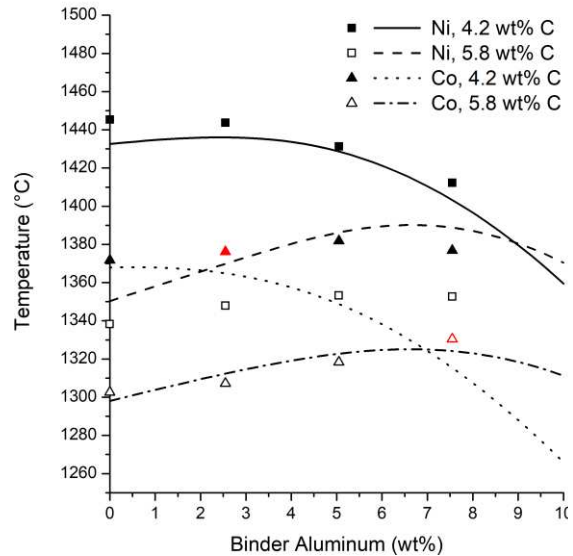


Figure 29: Calculated (lines) and measured (symbols) solidus temperatures of cemented carbides versus binder aluminum concentration. The red colored datapoints could not be evaluated validly. Calculations were carried out using the TCFE9 database.

values coincide very well with the present results at 100 % nickel proportion and the deviations in the nickel-free samples are only 5 K. Therefore, the temperatures of liquid formation and their compositional dependencies seem valid in the present work.

The solidus temperature of cemented carbides was calculated for binder aluminum concentrations between 0 and 10 wt% using the TCFE9 database. Only binary binder systems, i.e. aluminum-cobalt and aluminum-nickel, were modelled because mixtures of cobalt and nickel as binder are not well defined in the used database as already discussed in chapter 3.2. A tungsten-rich and a carbon-rich series were calculated with 4.2 and 5.8 wt% carbon, respectively, analogous to the experimental samples. The calculated curves are shown in Figure 29 along with the corresponding measurement results. Calculations for the tungsten-rich nickel-series and the carbon-rich cobalt-series describe the experimental determined temperatures remarkably well. Aluminum lowers the solidus temperature in the former case and elevates it in the latter one. The calculations for the carbon-rich nickel-series show an increasing solidus temperature but the measured effect is far less pronounced. And the calculated tungsten-rich cobalt-series does not reflect the subtle increase of the solidus temperature which can be seen in the experimental results. However, the experimentally determined curves of the nickel-series

seem to approach each other at higher aluminum concentrations with solidus temperatures between 1340 and 1380 °C. This coincides quite well with the solidus temperature of a cemented carbide with 20 wt% nickel and 3 wt% aluminum from [22]. The temperature of liquid formation is measured to be between 1380 and 1400 °C and calculated to stay almost constant between 4 and 5 wt% carbon in their work. Since the two measured curves approach or even intersect each other, a constant solidus temperature between 4.2 and 5.8 wt% carbon would indeed be possible at higher aluminum concentrations.

3.4.2 Analysis of Phases

BSE micrographs of all 40 samples which show a common section and the binder microstructure as inlet are given in the appendix in chapter 6.1.3. The present phases were identified and the results are given in Table 20 together with the results of difference thermal analysis. Graphite was, as intended, found in every sample of the carbon-rich series. η , on the other hand, could not easily be identified in WC505025W and WC158525W via scanning electron microscopy since no big areas of this phase are visible. But a closer look at WC158525W reveals finely dispersed structures with a more rectangular shape than quadratic WC. This indicates that the carbon window is shifted to higher carbon concentrations and the sample is further in the η region [5]. Although not observed directly in WC505025W, it is quite unlikely that no η carbide has formed in this sample since it has been found in every other tungsten-rich sample. It might just be dispersed very finely.

γ' is observable in micrographs of five tungsten-rich samples with 5 and 7.5 wt% aluminum concentration in binder. Although not visible in WC851575W at the default resolution, very fine precipitates can be seen at higher resolution in Figure 30. Since γ' is also visible in WC158575W and WC00Ni75W, this phase is expected to be stable in WC505075W as well but cannot be observed in BSE micrographs. There might be similar reasons like for Co30Ni12Al11W (see chapter 3.1.2) where either only γ' is stable or there is no Z-contrast between γ and γ' . A phase transformation can be seen in DTA curves and the temperature fits perfectly into the trend of an increasing γ' solvus with increasing nickel content. γ/γ' phase transformations were also found in measurements

Table 20: Summary of microstructural analysis of cemented carbides which were prepared from powder mixtures in the difference thermal analyzer. The present phases other than WC and γ are γ' and η for the tungsten-rich samples, and κ and graphite for the carbon-rich samples. \checkmark and x represent absent and present phases, respectively. DTA measured temperatures in °C are given as well, where phases with bold numbers were also found metallographically and the ones with cursive numbers are missing in BSE micrographs. ? will be discussed separately.

Sample	γ'	η	Sample	κ	Graphite
WCCo0000W	x	\checkmark	WCCo0000C	x	\checkmark
WC851500W	x	\checkmark	WC851500C	x	\checkmark
WC505000W	x	\checkmark	WC505000C	x	\checkmark
WC158500W	x	\checkmark	WC158500C	x	\checkmark
WC00Ni00W	x	\checkmark	WC00Ni00C	x	\checkmark
WCCo0025W	x	\checkmark	WCCo0025C	x	\checkmark
WC851525W	x	\checkmark	WC851525C	x	\checkmark
WC505025W	x	?	WC505025C	x	\checkmark
WC158525W	x	?	WC158525C	x	\checkmark
WC00Ni25W	x	\checkmark	WC00Ni25C	x	\checkmark
WCCo0050W	887	\checkmark	WCCo0050C	1112	\checkmark
WC851550W	909	\checkmark	WC851550C	1191	\checkmark
WC505050W	1093	\checkmark	WC505050C	x	\checkmark
WC158550W	1100	\checkmark	WC158550C	x	\checkmark
WC00Ni50W	1160	\checkmark	WC00Ni50C	x	\checkmark
WCCo0075W	x	\checkmark	WCCo0075C	1330?	\checkmark
WC851575W	991	\checkmark	WC851575C	1284	\checkmark
WC505075W	1142	\checkmark	WC505075C	1188	\checkmark
WC158575W	1246	\checkmark	WC158575C	1164	\checkmark
WC00Ni75W	1293	\checkmark	WC00Ni75C	?	\checkmark

of samples with high cobalt ratio in the series with 5 wt% aluminum. The results are a bit unreliable since no two-phase binder microstructure was observed in these samples. But the trend of an increasing γ' solvus with increasing nickel content is a sign for correct

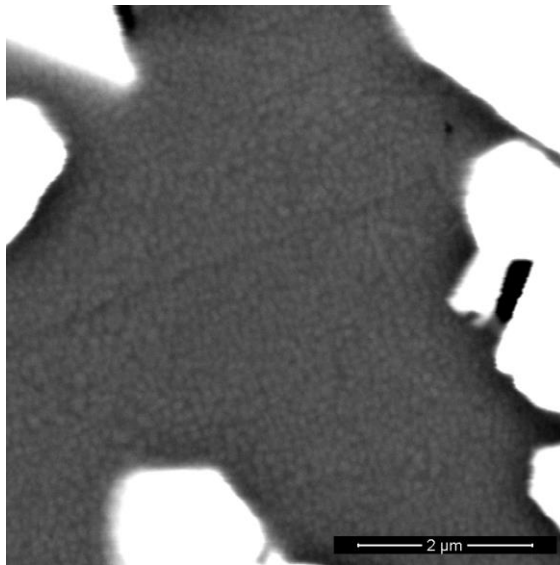


Figure 30: BSE micrograph of WC851575W at high resolution where very fine γ' precipitates are visible in the binder phase.

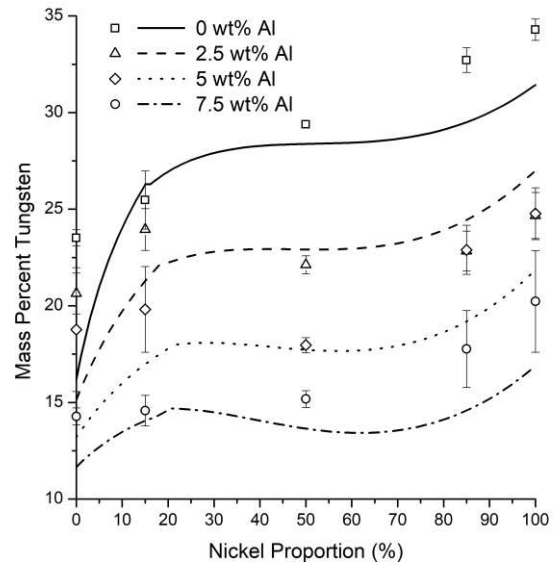


Figure 31: EDS measured (WA quantification, symbols) and calculated (lines) binder tungsten concentration of the tungsten-rich cemented carbides versus nickel proportion of the cobalt-nickel binder. Calculations were carried out at 1000 °C using the TCFE9 database.

interpretation of the measurements. No γ' precipitation can be measured in WCCo0075W although it was determined in WCCo0050W and aluminum tends to stabilize γ' . But in the aluminum-cobalt-tungsten system the stable composition range for γ' is quite narrow [9] and small deviations could prevent it from forming. A decreasing tungsten solubility with an increasing aluminum concentration was observed which also affects the stability of γ' . Figure 31 shows this effect for the tungsten-rich samples but details of the binder composition analysis are discussed below.

κ is visible in WCCo0050C and WC851550C, and in all carbon-rich samples with 7.5 wt% aluminum in binder. It seems like nickel has destabilizing effects on this phase because it is only visible at high cobalt ratios in the samples with 5 wt% aluminum. This finding can also be reasoned from the observations in chapter 3.2 where κ needs higher carbon concentrations to become stable when nickel is added. When enough aluminum is added κ will be stable at higher nickel concentrations as well. All of this might be indirectly a function of the binder tungsten concentration. As already discussed, more carbon will reduce the amount of tungsten through formation of η and WC, and aluminum tends to decrease the binder tungsten solubility while nickel increases it. Thus, a binder

with little nickel and aluminum concentration will dissolve less tungsten and it is more likely that κ becomes stable. This can also be reasoned from the micrographs where κ frequently appears to form at the edges of WC. The reason behind this may be a depletion of tungsten around the carbides as these precipitate from the binder and grow in size. The formation temperature of κ could not be determined for WCCo0075C and WC00Ni75C although the phase is clearly visible in the micrographs. In the former sample the quaternary phase reaction between liquid, WC, γ and graphite might overlap with the κ formation because the measured solidus temperature is unexpectedly high (see Figure 27 b)). This temperature of 1330 °C coincides quite well with the temperature of the κ dissolving experiment at the end of chapter 3.2. In WC00Ni75C the reaction heat could be very low and spread out over a wide temperature range. A small dent at 1150 °C can even be observed in the cooling curve but since it is not seen in the heating curve this value cannot be evaluated. The κ formation temperature increases with the binder nickel concentration in the 5 wt% aluminum series but decreases in the samples with 7.5 wt% aluminum.

3.4.3 Binder Composition Analysis

The results of EDS binder measurements for all samples are given in Table 21. As mentioned above, aluminum decreases the tungsten solubility which can be seen in Figure 31 for the tungsten-rich samples. This effect is quite pronounced because the solubility is decreased by over 60 % between the samples with 0 and 7.5 wt% binder aluminum. The tungsten concentration of the carbon-rich samples cannot be discussed quantitatively because the exact carbon concentration is presumably different in every sample. But the trend of aluminum decreasing the tungsten concentration is qualitatively observed as well. Nickel increases the tungsten solubility which can also be seen in Figure 31 and is well known in the literature [25, 62]. Thermodynamic equilibrium calculations at 1000 °C were additionally carried out using the TCFE9 database. The trends coincide quite well with the EDS results, but higher tungsten concentrations were measured, especially for the samples with 0 and 100 % nickel proportion. From Table 21 it seems like nickel also influences the binder aluminum concentration because it is higher

Table 21: EDS measured binder compositions (WA quantification) in wt% of cemented carbides which were prepared from powder mixtures in the difference thermal analyzer. Three measurements inside a section of $15 \times 15 \mu\text{m}$ were carried out for each sample.

Sample	Al	W	Sample	Al	W
WCCo0000W	–	23.5 ± 0.4	WCCo0000C	–	5.1 ± 0.7
WC851500W	–	25.5 ± 1.5	WC851500C	–	5.9 ± 0.2
WC505000W	–	29.4 ± 0.2	WC505000C	–	9.5 ± 1.4
WC158500W	–	32.7 ± 0.6	WC158500C	–	12.4 ± 0.8
WC00Ni00W	–	34.3 ± 0.5	WC00Ni00C	–	14.7 ± 0.2
WCCo0025W	0.9 ± 0.2	20.6 ± 1.1	WCCo0025C	1.6 ± 0.1	4.5 ± 0.4
WC851525W	1.3 ± 0.3	23.9 ± 1.1	WC851525C	2.5 ± 0.2	5.5 ± 2.1
WC505025W	1.5 ± 0.0	22.1 ± 0.5	WC505025C	1.9 ± 0.1	6.8 ± 0.4
WC158525W	1.9 ± 0.2	22.8 ± 1.0	WC158525C	2.3 ± 0.1	6.8 ± 0.8
WC00Ni25W	2.0 ± 0.2	24.7 ± 1.2	WC00Ni25C	2.5 ± 0.1	8.7 ± 1.0
WCCo0050W	3.6 ± 0.2	18.8 ± 3.2	WCCo0050C	4.4 ± 0.5	5.8 ± 4.5
WC851550W	4.4 ± 0.2	19.8 ± 2.2	WC851550C	6.1 ± 0.1	3.6 ± 0.5
WC505050W	5.2 ± 0.1	18.0 ± 0.4	WC505050C	4.8 ± 0.4	7.5 ± 2.1
WC158550W	4.0 ± 0.5	22.9 ± 1.3	WC158550C	5.0 ± 0.1	7.3 ± 0.4
WC00Ni50W	4.5 ± 0.2	24.8 ± 1.3	WC00Ni50C	4.7 ± 0.1	10.1 ± 0.6
WCCo0075W	5.2 ± 0.1	14.3 ± 0.4	WCCo0075C	5.9 ± 0.4	5.0 ± 0.8
WC851575W	6.0 ± 0.4	14.6 ± 0.8	WC851575C	4.8 ± 0.3	3.9 ± 0.2
WC505075W	6.9 ± 0.5	15.2 ± 0.4	WC505075C	7.1 ± 1.0	3.0 ± 0.6
WC158575W	6.3 ± 0.7	17.8 ± 2.0	WC158575C	7.1 ± 0.1	4.6 ± 0.4
WC00Ni75W	6.8 ± 1.5	20.2 ± 2.6	WC00Ni75C	6.8 ± 0.8	6.0 ± 1.1

for samples with higher nickel proportion. The tungsten concentration must be mathematically eliminated for a correct value of the recovery rate of aluminum. This leads to almost full recovery for samples with high nickel proportion, but in all nickel-free samples aluminum is lost. Considering the EDS measurements of η in Table 16 and Table 18 from chapter 3.2, some aluminum could be dissolved in these carbides.

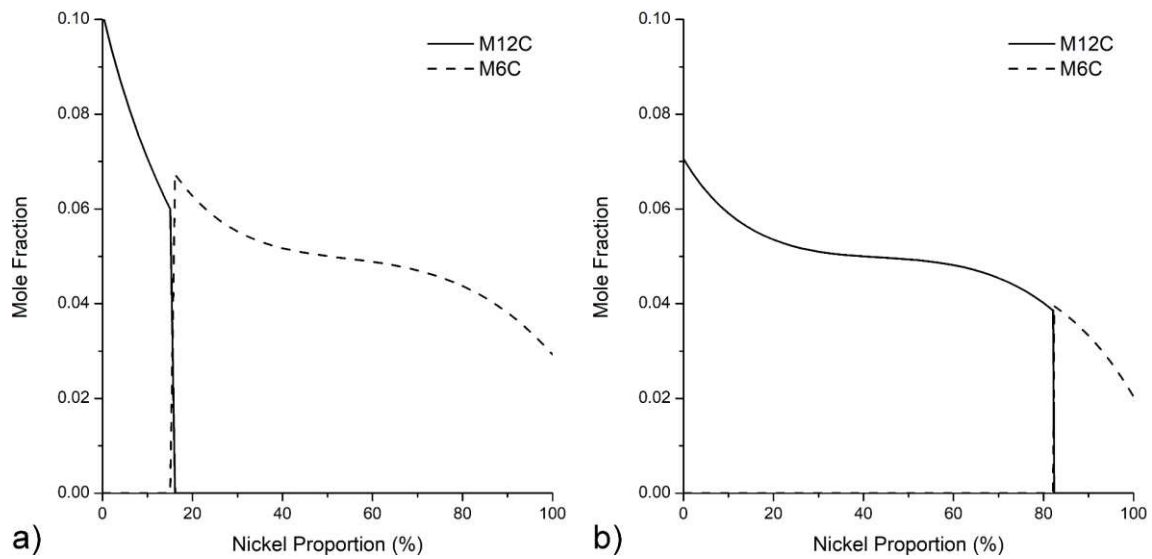


Figure 32: Calculated mole fractions of η in cemented carbides with 20 wt% cobalt-nickel binder and 4.23 wt% carbon at 1000 °C plot against the nickel proportion of the binder. There is a huge difference if a) TCFE9 database or b) Zhou16 database is used but the trend of a transformation from $M_{12}C$ to M_6C with increasing nickel proportion can be concluded quite certainly.

There, $M_{12}C$ seems to dissolve more aluminum than M_6C or WC, but nickel readily stabilizes the latter phases when more carbon is added. No definite literature source was found but from thermodynamic calculations (see Figure 32) it is known that $M_{12}C$ is less likely to form the more nickel is added. This leads to the assumption that the binder aluminum concentration is reduced in samples with less nickel due to the dissolution in $M_{12}C$. The lower aluminum loss in carbon-rich samples supports this hypothesis since no η phase is formed there. Unfortunately, no compositional measurements of the carbides were carried out for a certain conclusion of this observation. Still, some aluminum is lost which might have preparational reasons or is a measurement error since only three areas inside a 15 x 15 μm section of each sample were analyzed.

3.5 Ab Initio Calculations

3.5.1 Reference State Elements

The lattice constants of the calculated elements in their reference structures are given in Table 22 and compared to experimentally determined literature values. The error of the lattice constants is well below 1 % for each element. Quite small cutoff energies of the plane waves were needed for reaching converged results. In nickel, convergence was hardest to obtain, followed by cobalt, tungsten, carbon, and aluminum which consents with the number of valence electrons in this series with 10, 9, 6, 4 and 3, respectively.

Table 22: Calculated reference state elements with the maximum kinetic energy of allowed plane waves (*ecut*), and comparison of calculated and experimentally determined lattice constants.

Element	Structure	<i>ecut</i> (Ha)	Lattice constant (Å)	Reference value (Å)
C	Diamond	30	3.570	3.567 [67]
Al	FCC	30	4.039	4.046 [68]
Co	HCP	50	a = 2.491 c = 4.044	a = 2.507 [69] c = 4.070 [69]
Ni	FCC	70	3.524	3.499 [68]
W	BCC	40	3.185	3.155 [68]

3.5.2 L1₂ structures

All twelve possible binary permutations of aluminum, cobalt, nickel, and tungsten which form a compound with A₃B configuration were calculated. The evaluated enthalpies of formation from the total energies according to chapter 2.6 are given in Table 23 and compared to reference values where available. The results agree to each other quite well within a few kilojoule, especially with [18] where the difference is below 5 % even though an other software package was used for the calculations in this work. The cutoff energies of the plane waves which were needed for reaching converged results have quite a wide range. In compounds with nickel the *ecuts* are the highest and they decrease analogous to the values for the reference state elements.

Table 23: Calculated enthalpies of formation for the L1₂ structure type compounds with the maximum kinetic energy of allowed plane waves (*ecut*) and comparison with calculated energies from other literature sources.

Compound	<i>ecut</i> (Ha)	Enthalpy of formation (kJ/(mol atom))	Reference value (kJ/(mol atom))
Al ₃ Co	50	-19.69	-20.07 [18]
			-22.60 [19]
Co ₃ Al	50	-16.23	-17.05 [18]
			-19.90 [19]
Al ₃ Ni	80	-20.96	-22.90 [19]
Ni ₃ Al	90	-41.75	-42.38 [19]
Al ₃ W	40	6.16	-
W ₃ Al	50	19.75	-
Co ₃ Ni	80	3.86	-
Ni ₃ Co	110	0.96	-
Co ₃ W	60	-4.08	-
W ₃ Co	70	25.36	-
Ni ₃ W	90	11.17	-
W ₃ Ni	80	17.45	-

The thermodynamically stable compounds with L1₂ structure at 0 K are Al₃Co, Co₃Al, Al₃Ni, Ni₃Al and Co₃W because they have negative enthalpies of formation. This predicts that these could be found as (meta)stable phases in the binary systems aluminum-cobalt, aluminum-nickel, and cobalt-tungsten. But only Co₃Al and Ni₃Al are observed experimentally or described in thermodynamic assessments with L1₂ structure [33, 70]. The other compounds are not formed because at this composition intermetallic phases with different crystal structures are presumably more stable. Al₃Co is described as stoichiometric phase of the space group P2/m but no value for the enthalpy of formation was found [33]. Al₃Ni forms crystals of the space group Pnma with an enthalpy of formation of about -40 kJ/(mol atom) [70, 71] which is much more stable than in the L1₂ structure. The D0₁₉ phase was already introduced in chapter 3.1.1 and is the stable form of the

Co_3W compound with an enthalpy of formation of about $-8 \text{ kJ}/(\text{mol atom})$ [33] which is a little less than in the L1_2 structure.

Co_3Al with L1_2 structure on its own does not form in the binary system [72] but is readily stabilized through the addition of tungsten in the form of $\text{Co}_3(\text{Al,W})$ and might even be stable in the ternary system [9, 11]. $\text{L1}_2 \text{Co}_3\text{W}$ has a negative enthalpy of formation and this could facilitate the replacement of aluminum with tungsten and allow the formation of a (meta)stable compound. The enthalpy of formation of $\text{L1}_2 \text{Ni}_3\text{W}$ on the other hand is positive and thus, tungsten might destabilize γ' when $\text{Ni}_3(\text{Al,W})$ is formed. But since the enthalpy of formation of $\text{L1}_2 \text{Ni}_3\text{Al}$ is very negative, a quite high amount of tungsten can be dissolved before the structure is not stable anymore. This can be reasoned from the ternary phase diagram where γ' consist of up to 10 at% tungsten [40]. Still, the destabilizing effect is seen in the γ' partition coefficients which reveal that tungsten changes from a γ' to a γ former at higher concentrations [73].

The most positive enthalpies of formation are found for the compounds with three tungsten atoms on the faces of the L1_2 structures which means they are the most unstable. This limits the maximum amount of tungsten in the γ' phase, whereas a higher amount of aluminum is possible since Al_3Co and Al_3Ni are quite stable. Definite conclusions are hard to draw from the other results, but the values are quite important for a thermodynamic description of the L1_2 phase in the aluminum-cobalt-nickel-tungsten system.

3.5.3 E2_1 structures

As discussed in chapter 2.6, two different configurations of the E2_1 structure are possible, i.e. A_3BC with B in the corners and A_2BAC with A in the corners which are called $\text{E2}_1\text{-I}$ and $\text{E2}_1\text{-II}$, respectively. The order of the first three atoms is alphabetically and the fourth atom is always the one on the corners, followed by C for the carbon atom in the center. All permutations with aluminum, cobalt, and nickel as A or B were calculated and the results are given in Table 24. Tungsten was not considered for these calculations since it is not found to dissolve into κ phase and even seems to destabilize its formation as discussed in chapter 3.4.2. The ecuts for reaching convergence follow the series from

Table 24: Calculated enthalpies of formation for the E₂₁ structure type compounds with the maximum kinetic energy of allowed plane waves (ecut) and comparison with calculated energies from other literature sources. Each compound was calculated in two different configurations, i.e. E₂₁-I A₃BC and E₂₁-II A₂BAC with B and A in the corners, respectively.

Compound	ecut (Ha)	Enthalpy of formation (kJ/(mol atom))	Reference value (kJ/(mol atom))
Al ₃ CoC	40	25.22	24.44 [18]
Al ₂ CoAlC	50	23.23	22.51 [18]
			22.70 [19]
Co ₃ AlC	50	-23.07	-24.25 [18]
			-35.80 [19]
AlCo ₂ CoC	80	17.49	11.87 [18]
Al ₃ NiC	70	14.03	-
Al ₂ NiAlC	70	23.52	12.90 [19]
Ni ₃ AlC	100	-19.17	-28.20 [19]
AlNi ₂ NiC	90	6.98	-
Co ₃ NiC	80	16.59	-
			-
Co ₂ NiCoC	110	22.72	-
	120	33.12	-
Ni ₃ CoC	90	25.12	-
	110	33.06	-
CoNi ₂ NiC	120	18.17	-
			-
Al ₄ C	50	29.98	29.87 [18]
			32.10 [19]
Co ₄ C	60	19.03	18.73 [18]
			19.60 [19]
Ni ₄ C	90	17.46	12.20 [19]

chapter 3.5.1 again, with compounds consisting of nickel needing the highest values. The calculations agree very well with [18] except for AlCo₂CoC where the reference enthalpy of formation is more than 5 kJ/(mol atom) lower. However, this is negligible because the stable configuration is Co₃AlC, i.e. the E₂₁-I structure, anyways. In contrast to

the results for the $L1_2$ structures, the differences to [19] are quite pronounced for the κ compounds. But it was already discussed in [18] that the enthalpy of formation for Co_3AlC is way too low there. Also, only one configuration of $E2_1$ with aluminum always in the corners was considered in their calculations.

The only stable compounds are the $E2_1$ -I structures Co_3AlC and Ni_3AlC with aluminum on the corners. The former one is found in the ternary system and has a very small homogeneity range, i.e. is almost stoichiometric, but with a carbon content between 10 and 12 at%. Therefore, it should rather be denoted as Co_3AlC_x where x is about 0.5 [18, 74, 75]. Ni_3AlC is not described as an individual intermetallic compound in the ternary system but as already discussed, Ni_3Al is stable there. The γ' phase has a high solubility of carbon with up to 10 at% and therefore, forms a homogenous phase field with κ which is nothing else but $L1_2$ Ni_3Al with a carbon atom in the body center to form $E2_1$ -I [19, 22, 23].

Co_3AlC is more stable than Ni_3AlC which could explain why the former phase seems to be more readily formed in cemented carbides (see chapter 3.4.2). Tungsten stabilizes the $L1_2$ structure of the cobalt compounds but seems to destabilize it in the nickel compounds which could further influence the formation of $E2_1$ in this system. Co_3Al is not found to be stable in the binary system but with carbon in the body center the structure is stabilized by almost 7 kJ/(mol atom).

Aluminum seems to preferably occupy the corners since Al_2CoAlC , Co_3AlC and Ni_3AlC are the more stable configurations of these compounds. Except for Al_3NiC which is more stable than its $E2_1$ -II pendant Al_2NiAlC . Probably because nickel also prefers to occupy the corners as can be seen in the enthalpies of formation of Co_3NiC and CoNi_2NiC versus their other configurations.

Co_2NiCoC and Ni_3CoC both have results for two different ecuts because the total energy spiked to a lower value at these exact cutoff energies of 110 and 90 Ha, respectively. The convergence study lead to higher ecuts when these outliers were removed. Using the lower cutoff energies but the parameters for the final calculation resulted in the higher

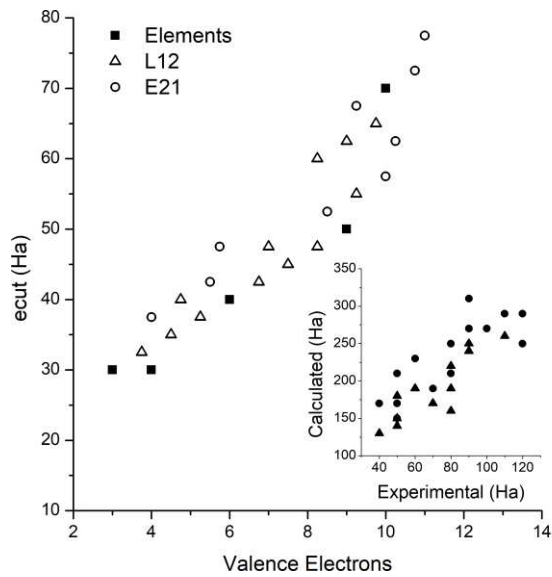


Figure 33: Kinetic cutoff energy for allowed plane waves (*ecut*) plot against the valence electrons of the reference state elements (see Table 22). The open symbols for $L1_2$ and $E2_1$ structures are interpolated *ecuts* from their normalized composition. The inset shows that the calculated and experimental *ecuts* of the compounds correlate linearly.

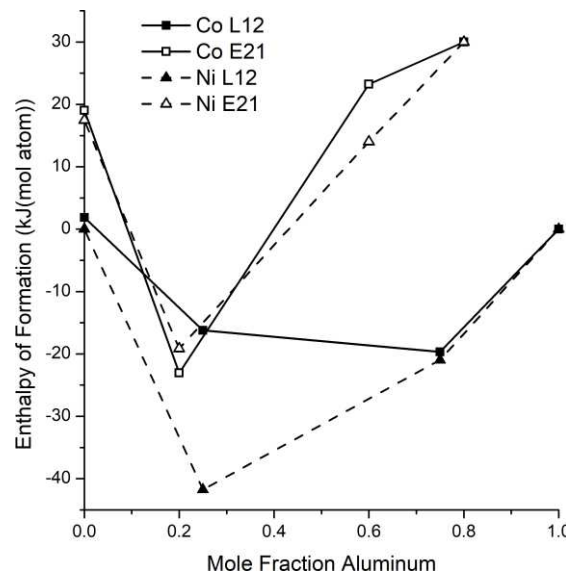


Figure 34: Calculated enthalpies of formation of cobalt (squares) and nickel (triangles) based $L1_2$ and $E2_1$ structures versus aluminum concentration of the compounds.

total energies. This means that the lower enthalpies of formation for Co_2NiCoC and Ni_3CoC are indeed outliers at the convergence study parameters but not fully converged results. However, the enthalpies of formation for the compounds in the other configuration, i.e. Co_3NiC and CoNi_2NiC , are lower anyway.

3.5.4 Comparison

As already discussed above, the *ecut* of the calculation depends on the valence electrons of the elements in the structure. This applies especially for the reference state elements as they show an almost linear or quadratic dependency as seen from the black squares in Figure 33. The same tendency is also seen for the $L1_2$ and $E2_1$ structures but the *ecuts* are not depending on the sum or average number of valence electrons. Interpolated values were calculated with the element's *ecuts* multiplied by their number in the structures. For example, Al_3Ni would have three times the *ecut* of aluminum plus one time the *ecut* of nickel resulting in 160 Ha. The results were normalized by the number of atoms and plot against the average number of valence electrons as open symbols in Figure 33. A linear dependency of the interpolated values with the experimental *ecuts* is seen in the

inset which has a slope of approximately 3. This indicates that the cutoff energy indeed depends on the average number of valence electrons but that the structure also influences it.

The calculated enthalpies of formation of the cobalt and nickel based compounds from Table 23 and Table 24 for $L1_2$ and $E2_1$ structures, respectively, are plot against their aluminum concentration in Figure 34. Ni_3Al resides in a deep well of stability and since Al_3Ni is also quite stable the slope between the two compounds is not very steep. This could explain why the phase field of the $L1_2$ structure also reaches into regions of higher nickel and aluminum concentrations [44]. Co_3Al on the other hand is not that stable compared to pure $L1_2$ /fcc cobalt which could inhibit its formation. But when carbon is introduced Co_3AlC sits in a steep well between Co_4C and Al_3CoC which seems to facilitate its formation but is also responsible for the narrow phase field [22].

4 Summary

The samples in this work are compositional quite different and not as consistent as it was intended. This leads to bad comparability because minor changes of the aluminum and tungsten concentrations affect the microstructure and physical properties to an extent which is measurable at least. The variations are mainly a result of the confusion with the wrong measurement results of the EDS quantification using the TEAM™ software which was discussed in chapter 2.1.4.

Nevertheless, a comparison of the samples from all different aspects of this work will be carried out using calculated ternary phase diagrams. Figure 35 shows such a plot for the aluminum-cobalt-tungsten system at 950 °C calculated using Thermo-Calc with the Zhu14 database. All samples from the ternary are included as symbols in the diagram, i.e. the binder compositions of the DTA cemented carbides from chapter 3.4, Co10Al10W from the compositional assessment (see chapter 3.1.1), Co12Al11W from the nickel-variation in chapter 3.1.2 and the Co9Al7WxC samples from the influence of carbon in chapter 3.2.

The DTA samples have different symbols depending on the present phases which were determined by metallographic and thermo analytic methods. The γ' and κ phases are considered stable at 950 °C if the measured solvus is above this temperature. Needless to say, carbon is not included in the calculations since it is not described in the Zhu14 database, but the effects might be derived as difference to the aluminum-cobalt-tungsten system. Most of the samples have a single phase γ binder only, which coincides quite well with the calculated results. The samples which are inside two-phase regions with D0₁₉ or B2 are on the edge of the calculated phase fields, so it is not surprising that no additional phases were found metallographically. The two samples with γ/κ microstructure imply that there is a tie line for the formation of κ between 2 and 5 at% tungsten. From the stoichiometric composition of Co₃AlC it could be reasoned that the upper limit of the two-phase region is around 20 at% aluminum. The superalloys Co10Al10W and Co12Al11W both have γ/γ' microstructure and the latter one even shows B2 phase,

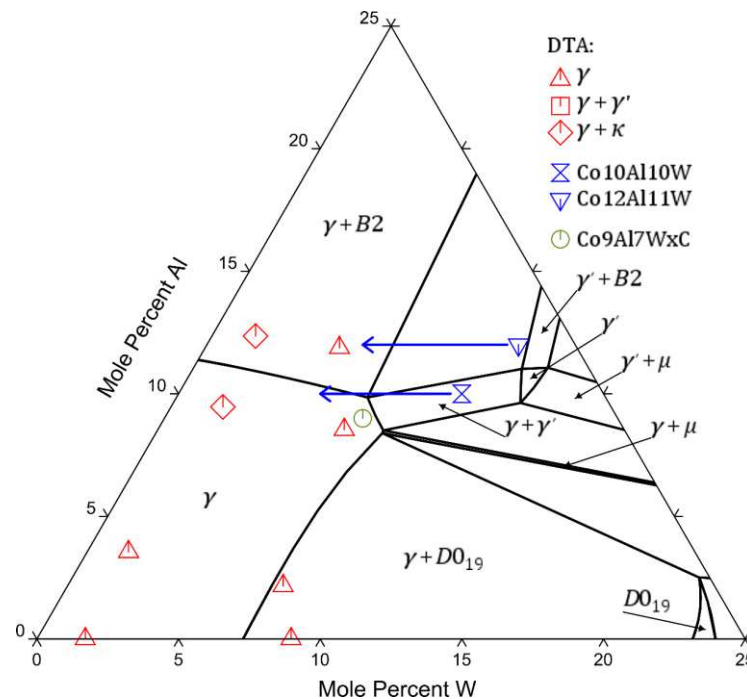


Figure 35: Calculated phase diagram of the aluminum-cobalt-tungsten system at 950 °C using Thermo-Calc with Zhu14 database. The red symbols show the binder microstructure of DTA cemented carbides from chapter 3.4 at EDS measured binder compositions (WA quantification). The blue symbols are for superalloys from chapter 3.1 and the arrows indicate the tungsten depletion which occurs through the infiltration into tungsten carbide. The green symbol shows the weighed in composition of carbon-influence samples from chapter 3.2.

besides μ and DO_{19} . After infiltration, the tungsten concentration is decreased significantly which is reflected by the blue arrows in Figure 35. It is assumed that approximately half of the initial amount of tungsten is preserved which can be reasoned by comparing the compositions before (from sample names) and after infiltration in Figure 23. The tip of the arrows is near the single-phase DTA samples, which coincide with the single-phase binder of the infiltrated samples in Figure 20 b) and Figure 21 a). The samples from the carbon influence investigation start inside the γ single-phase field and move to lower tungsten concentrations since it binds in the form of carbides when carbon is added. Eventually, it crosses the κ tie line. But before that, γ' seems to be stabilized which was already discussed based on Figure 16 c).

Nickel stabilizes the γ' phase which was discussed extensively before and can again be seen in Figure 36. The solid lines define the phase fields for alloys with a fixed cobalt to nickel ratio of 85:15 and the green dashed lines show the phase diagram for alloys with a constant nickel content of 15 at%. The other conditions for the calculations are the

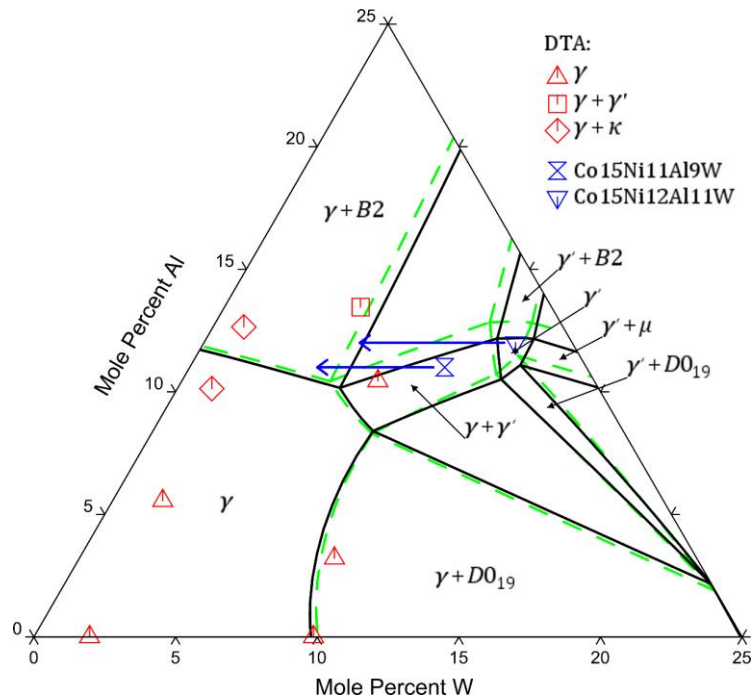


Figure 36: Calculated phase diagram of the aluminum-cobalt-nickel-tungsten system with a fixed cobalt to nickel ratio of 85:15 (black solid lines) and a constant nickel concentration of 15 at% (green dashed lines) at 950 °C using Thermo-Calc with Zhu14 database. The red symbols show the binder microstructure of DTA cemented carbides from chapter 3.4 at EDS measured binder compositions (WA quantification). The blue symbols are for superalloys from chapter 3.1 and the arrows indicate the tungsten depletion which occurs through the infiltration into tungsten carbide.

same as above. The results are very similar to each other which allows the comparison of the samples from DTA measurements with the infiltrated ones. The four DTA samples with the lower aluminum concentrations are again predicted and experimentally confirmed to have γ single-phase binder. The two γ/κ samples are in about the same region as their equivalents in Figure 35. It is quite surprising that the DTA sample with approximately 10 at% aluminum and 9 at% tungsten has γ single-phase binder only because the other three samples in this region do indeed show γ' precipitates (see Figure 21 b) and Figure 24). It would be possible that the γ' phase field is enlarged, and it is single-phase γ' instead. This would also explain why the other three samples have γ/γ' binder microstructure which is not predicted by the calculations. The microstructure of Co15Ni11Al9W from chapter 2.2.4 coincides with the predictions, probably because the composition is well defined from producing a bigger batch. But the calculations are also reasonable for the nickel-variation sample Co15Ni12Al11W (see 2.2.2) because, as already mentioned, some aluminum and tungsten might be lost during the preparation.

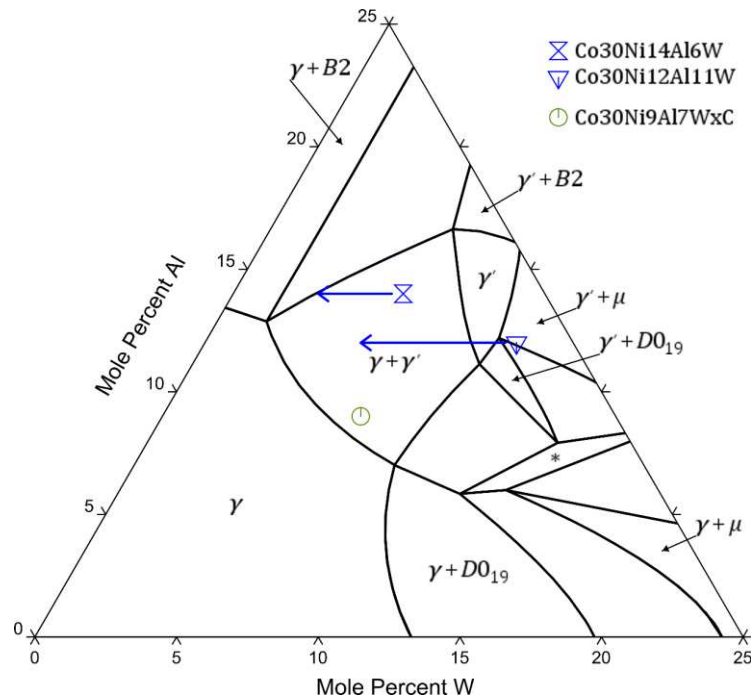


Figure 37: Calculated phase diagram of the aluminum-cobalt-nickel-tungsten system with a constant nickel concentration of 30 at% at 950 °C using Thermo-Calc with Zhu14 database. The blue symbols are for superalloys from chapter 3.1 and the arrows indicate the tungsten depletion which occurs through the infiltration into tungsten carbide. The green symbol shows the weighed in composition of carbon-influence samples from chapter 3.2.

The samples with a constant nickel concentration of 30 at% are plotted with the calculated results in Figure 37. Since there are no DTA samples, no additional phase diagram is plotted. Again, the γ' phase field is enlarged through the addition of nickel which confirms the assumption that Co30Ni12Al11W in Figure 12 c) is single-phase γ' , besides some μ and D0₁₉. The γ/γ' microstructure of Co30Ni14Al6W can be seen in Figure 10 d). Both infiltrated samples are also predicted fairly good which can be reasoned from Figure 21 c) and Figure 20 d) with γ/γ' and γ microstructure, respectively. But as already discussed, they are very inhomogeneous. The Co30Ni9Al7WxC samples start with a γ/γ' microstructure which coincides with the metallographically obtained results in Figure 17. They move to the left of the plot again, as the carbon concentration increases but the γ' precipitates do not vanish completely. This is again an indication, that carbon enlarges the γ' field such that the samples stay within the γ/γ' two-phase region until they cross the κ tie line to form the E2₁ phase.

In Figure 38 two phase diagrams are superimposed once more. The solid lines are for the DTA samples with a fixed cobalt to nickel ratio of 50:50 and the green dashed lines show

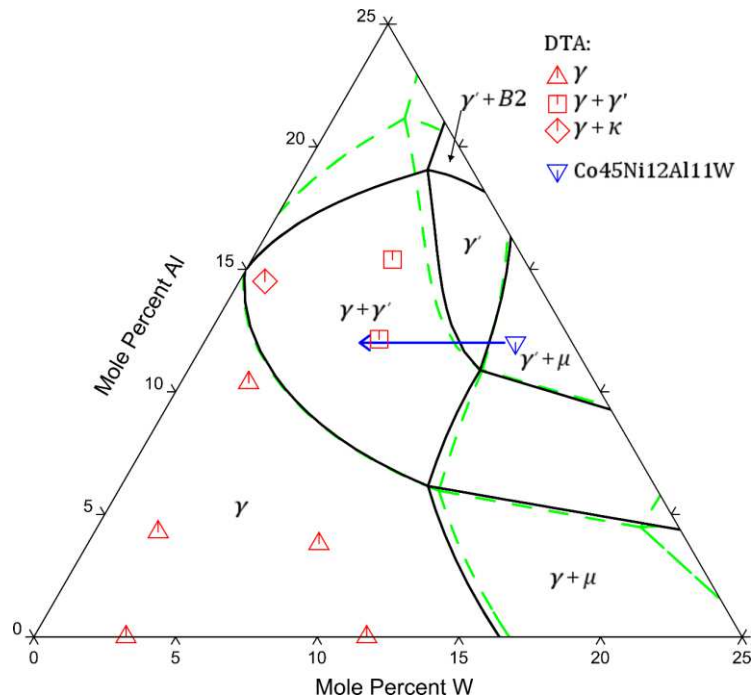


Figure 38: Calculated phase diagram of the aluminum-cobalt-nickel-tungsten system with a fixed cobalt to nickel ratio of 50:50 (black solid lines) and a constant nickel concentration of 45 at% (green dashed lines) at 950 °C using Thermo-Calc with Zhu14 database. The red symbols show the binder microstructure of DTA cemented carbides from chapter 3.4 at EDS measured binder compositions (WA quantification). The blue symbols are for superalloys from chapter 3.1 and the arrows indicate the tungsten depletion which occurs through the infiltration into tungsten carbide.

the phase regions of alloys with a constant nickel concentration of 45 at%. The calculated and experimentally determined results coincide very well with each other. The γ/κ region seems to have become smaller because only the DTA sample with the highest aluminum concentration shows this microstructure but the tie line is still somewhere between 2 and 5 at% tungsten. Co45Ni12Al11W is probably depleted in aluminum and tungsten because it rather is inside the three-phase field of $\gamma/\gamma'/\mu$ with comparably little μ (see Figure 11 d)). The infiltrated sample has γ/γ' microstructure as predicted but is very inhomogeneous again.

Alloys with fixed cobalt to nickel ratios of 15:85 and 0:100 are plot together with the corresponding DTA samples in Figure 39 and Figure 40, respectively. The calculations reflect the experimental results very well for the samples with high nickel content. The κ phase is again found only at high aluminum and low tungsten concentrations but inside the γ/γ' two phase region of the aluminum-cobalt-nickel-tungsten system.

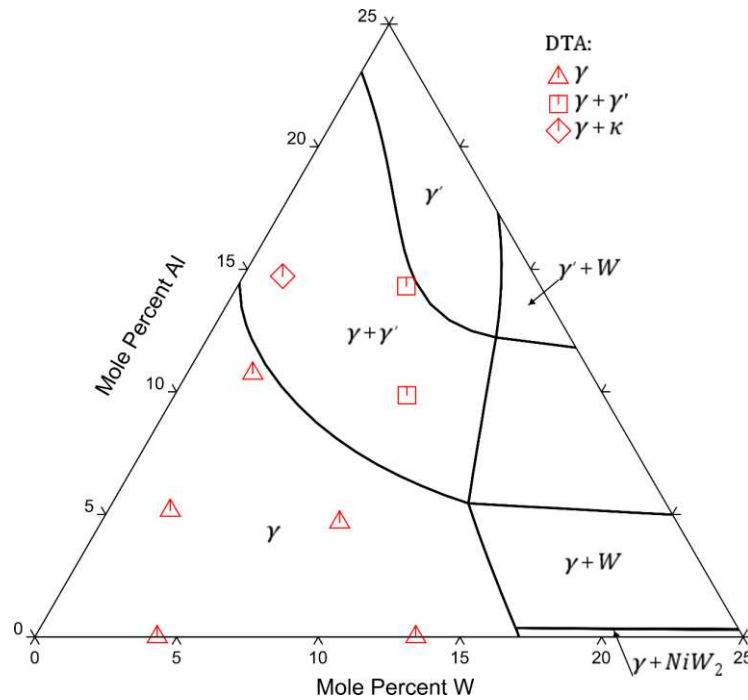


Figure 39: Calculated phase diagram of the aluminum-cobalt-nickel-tungsten system with a fixed cobalt to nickel ratio of 15:85 at 950 °C using Thermo-Calc with Zhu14 database. The red symbols show the binder microstructure of DTA cemented carbides from chapter 3.4 at EDS measured binder compositions (WA quantification).

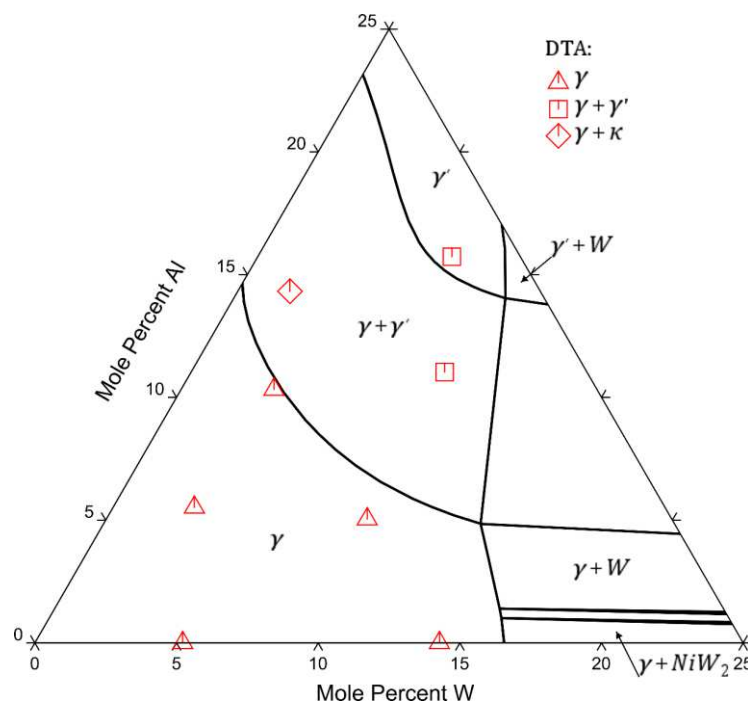


Figure 40: Calculated phase diagram of the aluminum-nickel-tungsten system at 950 °C using Thermo-Calc with Zhu14 database. The red symbols show the binder microstructure of DTA cemented carbides from chapter 3.4 at EDS measured binder compositions (WA quantification).

5 Conclusions and Outlook

The phase equilibria in cemented carbides with superalloys of the aluminum-cobalt-nickel-tungsten system as binder phase were investigated with focus on several aspects.

The following conclusions can be drawn from the results:

1. The precipitation of γ' inside a γ matrix of the investigated quaternary system is quite stable against preparational and compositional variations. Solution heat treatment leads to a more uniform microstructure but is not mandatory for obtaining the cuboidal precipitates. Aluminum concentrations between 9 and 14 at%, and tungsten concentrations between 6 and 12 at% enclose a non-exclusive compositional region where the γ/γ' microstructure constitutes the majority of the alloy. The addition of nickel stabilizes the γ' phase which leads to even more preparational stability as well as higher volume fractions and solvus temperatures.
2. This stability is lost when carbon is introduced to the system. First, very small carbon additions seem to promote the precipitation of γ' . But then, the amount of dissolved tungsten in the γ matrix is reduced through the formation of carbides and γ' vanishes. However, the absence of tungsten facilitates the formation of another precipitate phase, κ , which seems to be especially stable in the cobalt-rich samples.
3. γ/γ' binder microstructure of cemented carbides is hard to obtain because the maximum tungsten concentration is limited and depends on the overall carbon content. But nickel does not only stabilize the γ' phase, it also elevates the amount of dissolved tungsten in the binder phase of cemented carbides. This might be the reason why only nickel-containing samples worked out as intended in this work.
4. Aluminum additions of up to 15 at% to the binder of cemented carbides have moderate effects on the temperature of the quaternary phase reactions. But it was shown that other phase transformations at lower temperatures occur which yield γ , γ/γ' and γ/κ binder microstructures. These results may be useful for the thermodynamic description of the aluminum-carbon-cobalt-nickel-tungsten system.
5. Ab initio calculated enthalpies of formation of the γ and κ compounds coincide with literature data, reflect the experimental results, and might also be used for assessing the quinary system thermodynamically.

The thermodynamic description of the aluminum-carbon-cobalt-nickel-tungsten system is far from complete. There are many aspects which should be investigated in more detail with the most important being:

1. Producing samples with more consistent compositions would make it possible to compare them better with each other resulting in more certain conclusions. Also, the nickel variation is spread over a wide concentration range and since samples with 15 at% nickel yielded the best results, minor concentration changes starting from there should be investigated.
2. Some of the cemented carbides which were produced via DTA have the anticipated γ/γ' binder microstructure, even without heat treatment. Some more at least show a solvus reaction in the measurement curve. Especially the samples with cobalt to nickel ratio of 15:85, and 5 or 7.5 wt% aluminum look very promising. Cemented carbides with these binder compositions should be produced by conventional methods and investigated more thoroughly.
3. Furthermore, the DTA samples were only analyzed at two carbon concentrations. Promising candidates should be revisited using the same method from this work but with the focus on the whole carbon window.
4. The conditions for the formation of κ were roughly determined in this work but must be narrowed down even more. This could be achieved using the diffusion couple technique with which the phases in a sample with carbon gradient can be studied. But a proper quantification method using reference standards would be mandatory for determining the carbon concentration locally.
5. The ab initio calculations could be extended by using supercells of the structures with compositional different primitive cells. This would simulate the substitution of some element by another and, for example, the stabilizing effect of tungsten in $\text{Co}_3(\text{Al,W})$ could be studied.

With all the data which was gathered in this work and after elaboration of the open aspects from above, a thermodynamic assessment of the aluminum-carbon-cobalt-nickel-tungsten system with specialization on cemented carbides could be carried out. Many of the database parameters must be optimized but the foundation for reaching this goal is laid here.

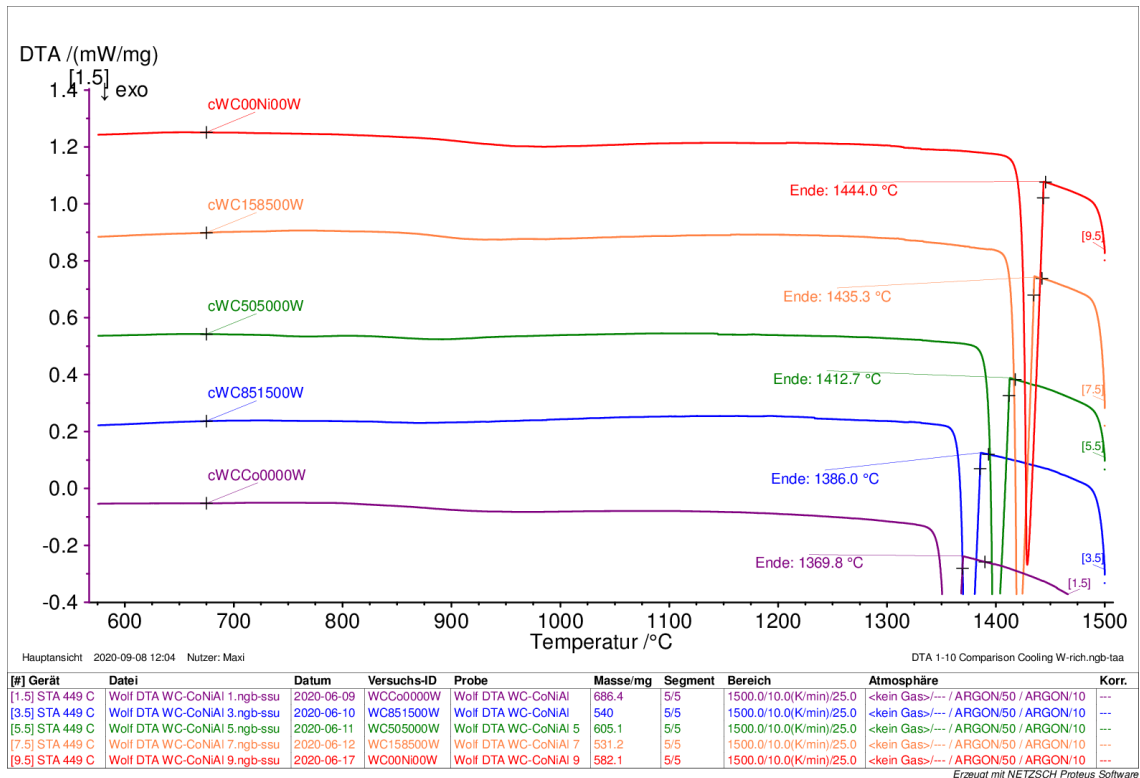
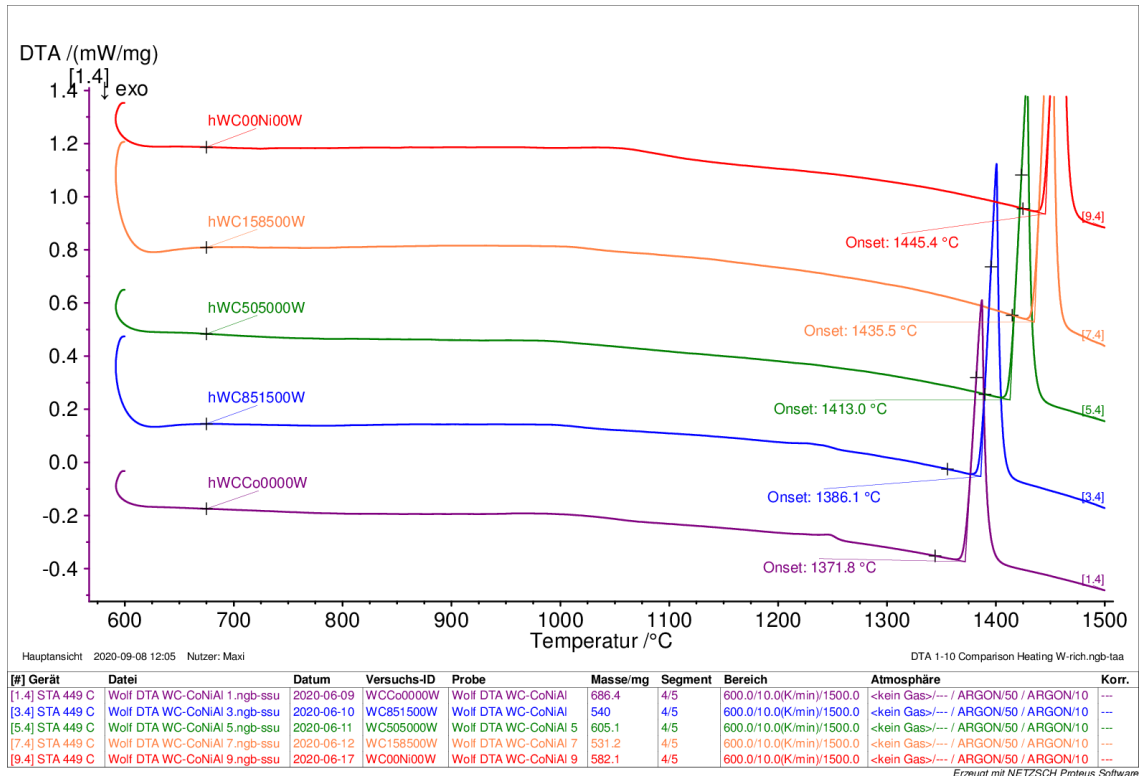
6 Appendix

6.1 Cemented Carbides via DTA

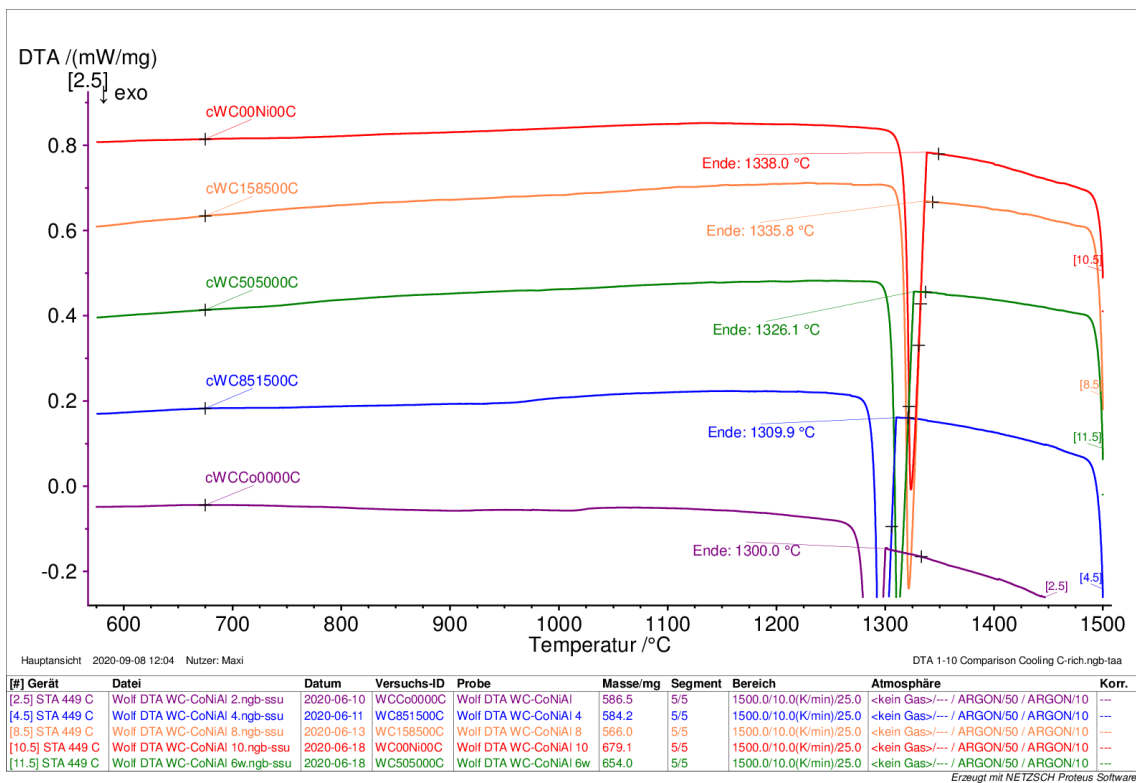
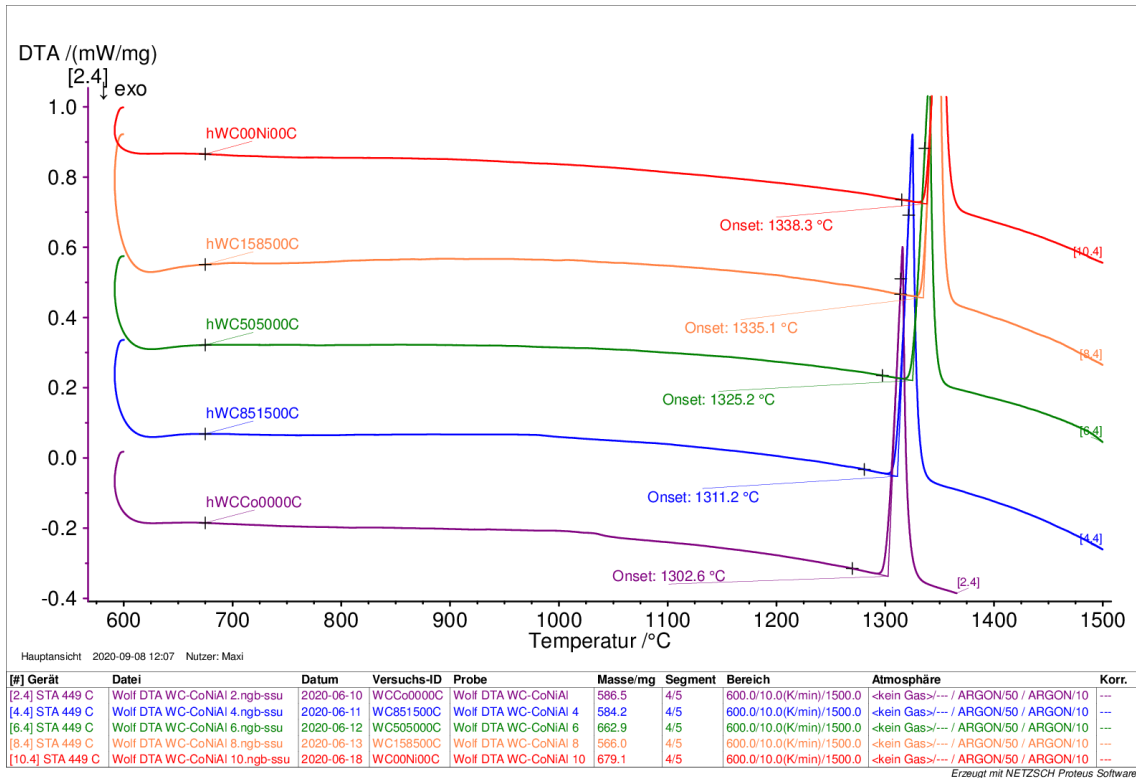
6.1.1 Weighed-In Compositions

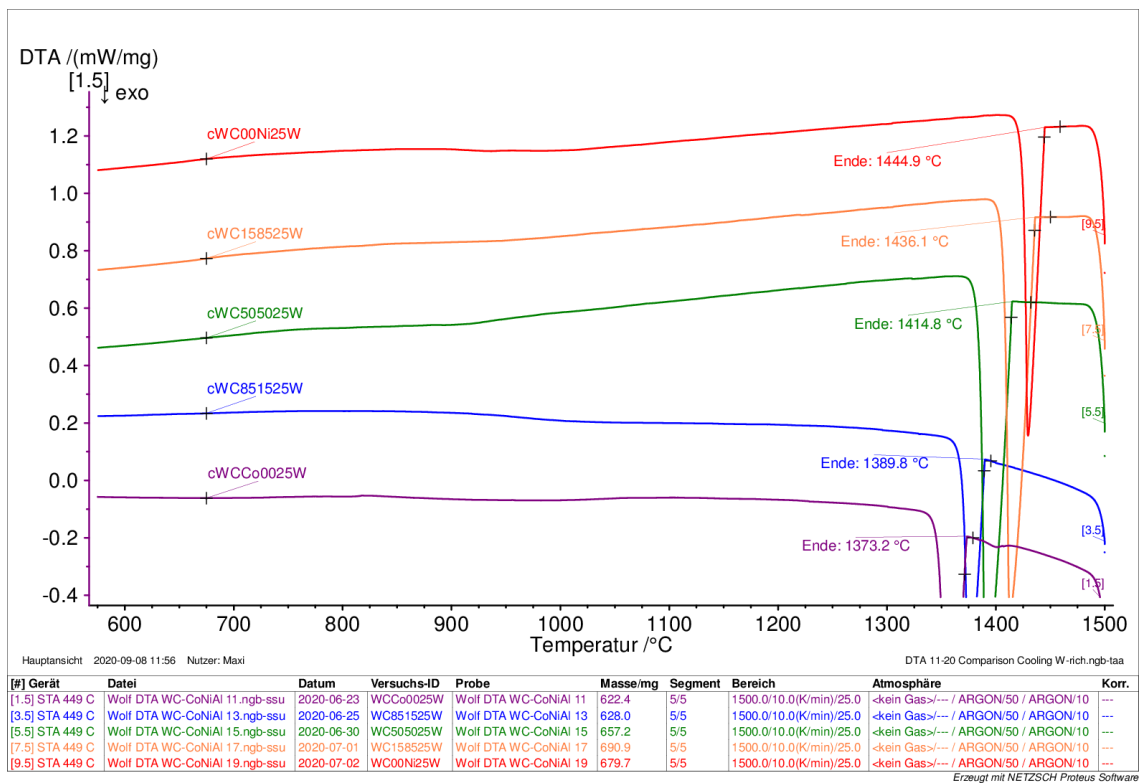
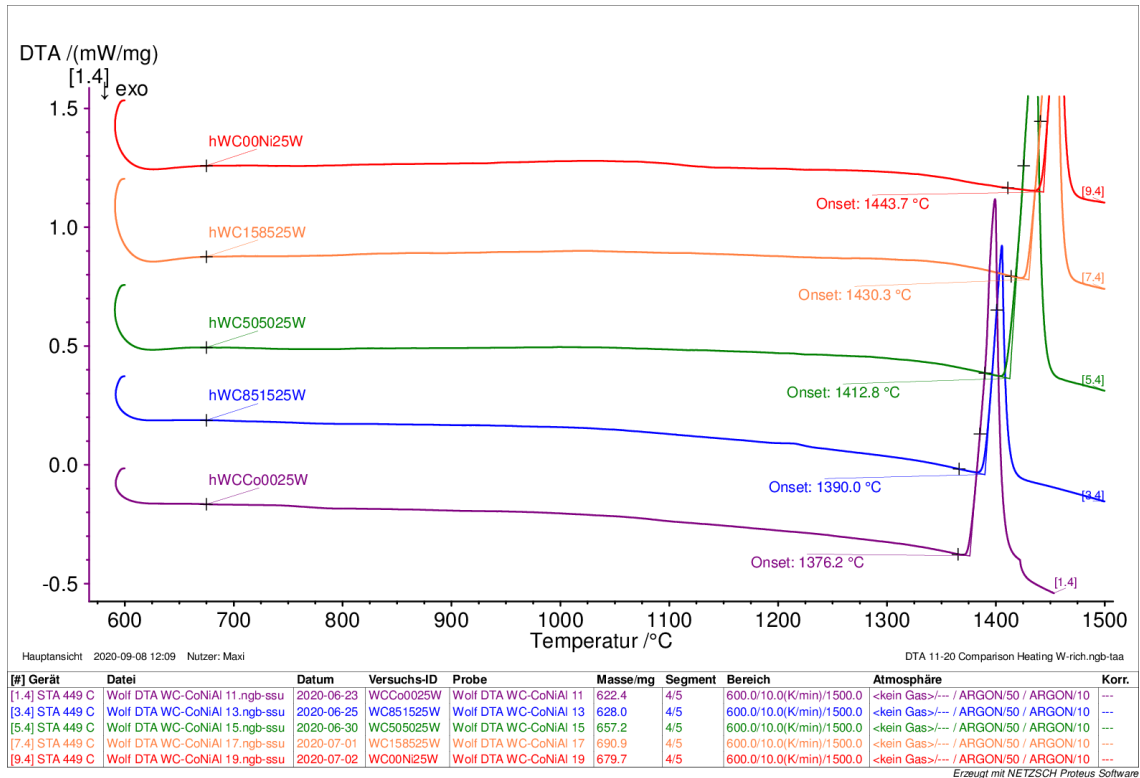
Sample	Co (wt%)	Ni (wt%)	Al (wt%)	W (wt%)	C (wt%)
WCCo0000W	19.99	0.00	0.00	75.77	4.23
WCCo0000C	20.00	0.00	0.00	74.17	5.84
WC851500W	17.00	3.01	0.00	75.76	4.23
WC851500C	17.02	3.02	0.00	74.11	5.85
WC505000W	10.02	10.02	0.00	75.73	4.23
WC505000C	10.00	10.00	0.00	74.16	5.84
WC158500W	3.00	17.01	0.00	75.76	4.23
WC158500C	3.01	17.05	0.00	74.10	5.84
WC00Ni00W	0.00	20.04	0.00	75.74	4.23
WC00Ni00C	0.00	20.03	0.00	74.13	5.84
WCCo0025W	19.47	0.00	0.50	75.79	4.23
WCCo0025C	19.50	0.00	0.50	74.16	5.84
WC851525W	16.58	2.94	0.50	75.75	4.23
WC851525C	16.56	2.94	0.50	74.16	5.84
WC505025W	9.77	9.77	0.50	75.73	4.23
WC505025C	9.73	9.74	0.50	74.19	5.85
WC158525W	2.92	16.56	0.50	75.78	4.23
WC158525C	2.93	16.58	0.50	74.15	5.84
WC00Ni25W	0.00	19.50	0.50	75.77	4.23
WC00Ni25C	0.00	19.52	0.50	74.14	5.84
WCCo0050W	19.01	0.00	1.02	75.74	4.23
WCCo0050C	18.98	0.00	1.00	74.18	5.85
WC851550W	16.15	2.86	0.99	75.76	4.23
WC851550C	16.13	2.86	1.00	74.17	5.85
WC505050W	9.50	9.50	0.99	75.78	4.23
WC505050C	9.50	9.50	1.01	74.15	5.84
WC158550W	2.85	16.15	0.98	75.78	4.23
WC158550C	2.85	16.15	1.01	74.15	5.84
WC00Ni50W	0.00	19.00	1.00	75.76	4.23
WC00Ni50C	0.00	18.98	0.99	74.18	5.85
WCCo0075W	18.49	0.00	1.50	75.77	4.23
WCCo0075C	18.54	0.00	1.50	74.12	5.84
WC851575W	15.71	2.78	1.49	75.79	4.23
WC851575C	15.72	2.79	1.52	74.13	5.84
WC505075W	9.24	9.24	1.50	75.78	4.23
WC505075C	9.25	9.25	1.50	74.15	5.84
WC158575W	2.78	15.74	1.50	75.75	4.23
WC158575C	2.78	15.73	1.49	74.16	5.84
WC00Ni75W	0.00	18.49	1.51	75.77	4.23
WC00Ni75C	0.00	18.51	1.50	74.15	5.84

6.1.2 DTA Measurements

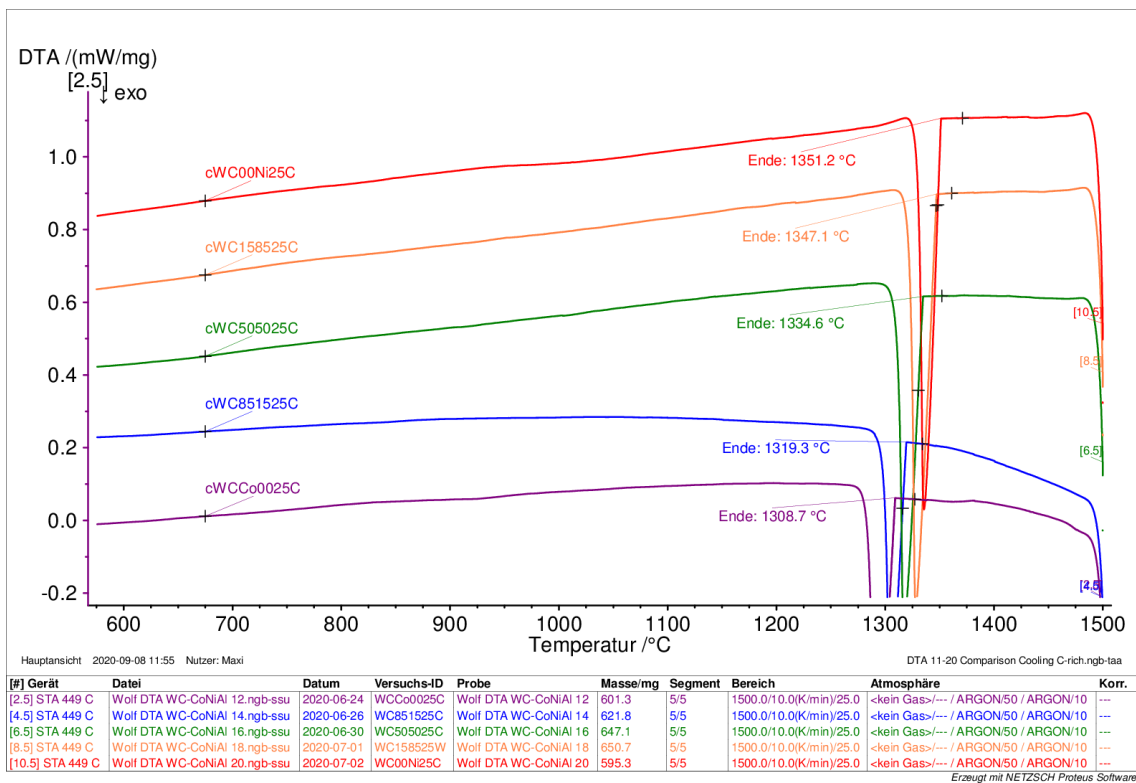
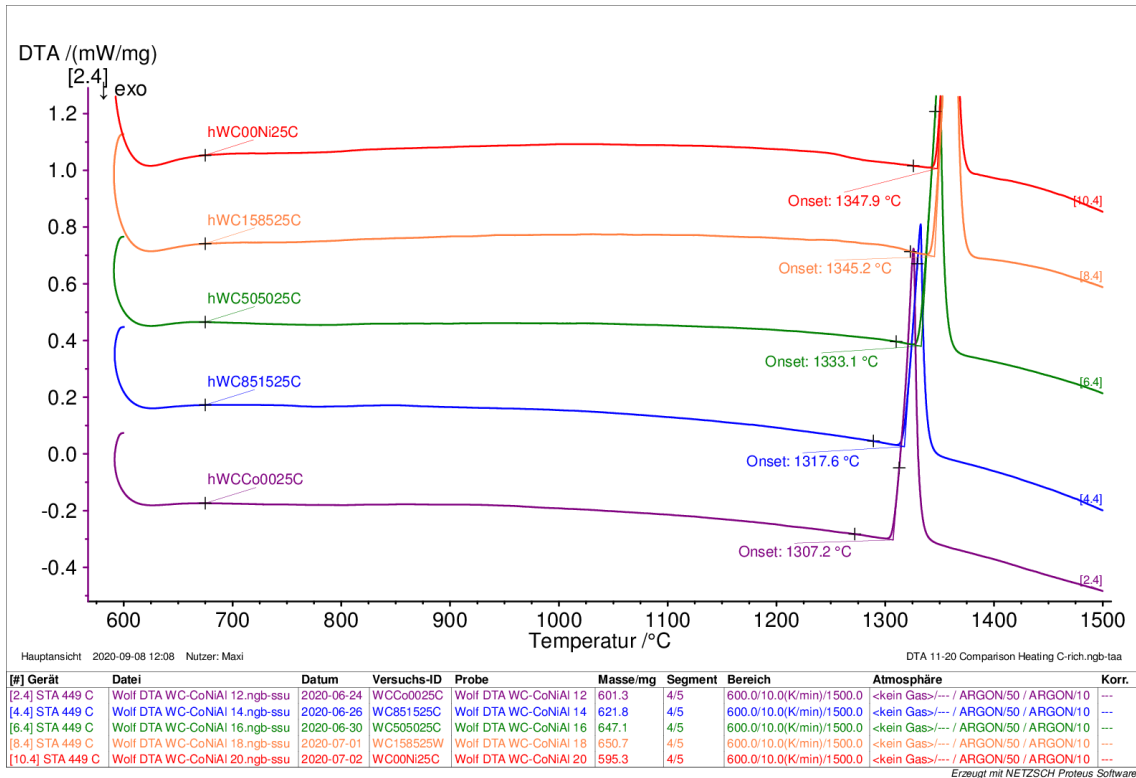


Die approbierte gedruckte Originalversion dieser Diplomarbeit ist an der TU Wien Bibliothek verfügbar. The approved original version of this thesis is available in print at TU Wien Bibliothek.

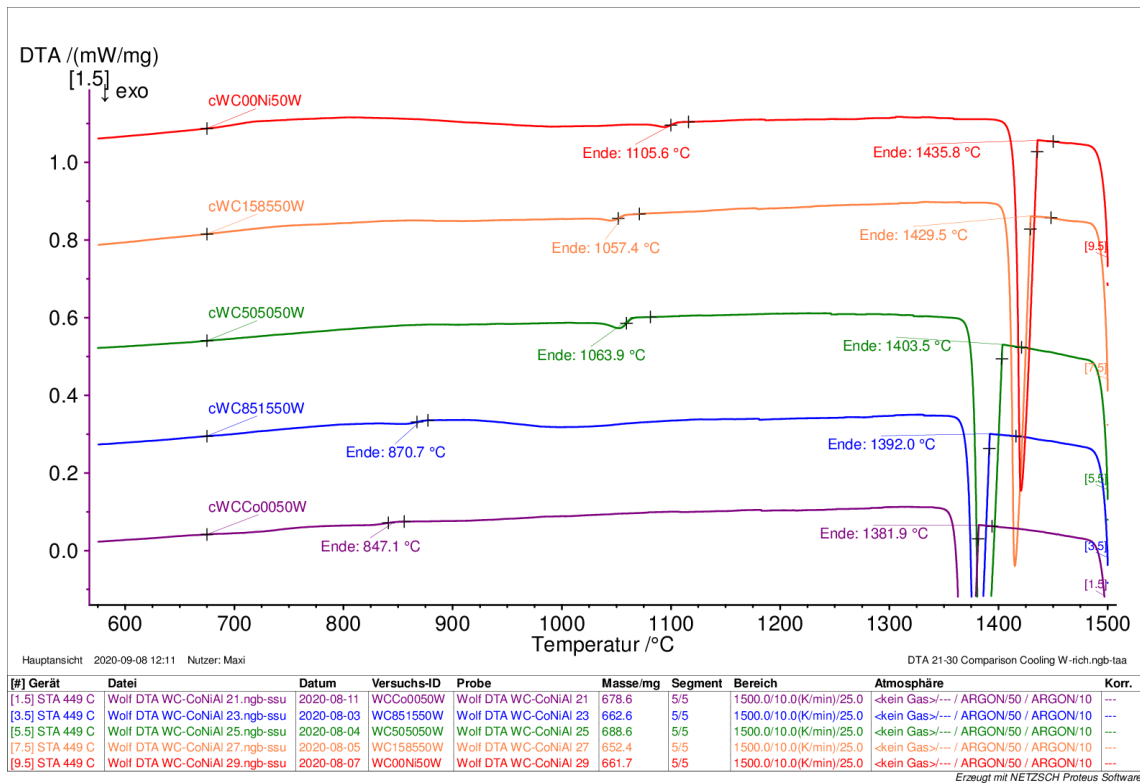
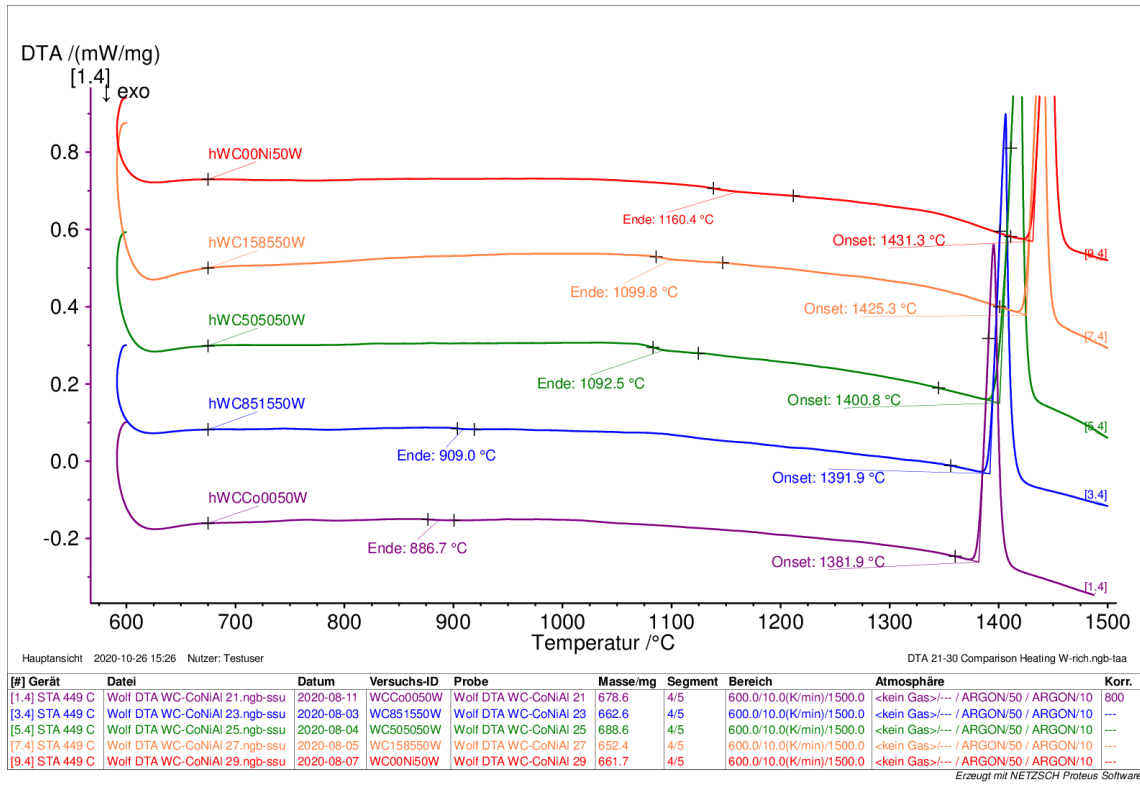




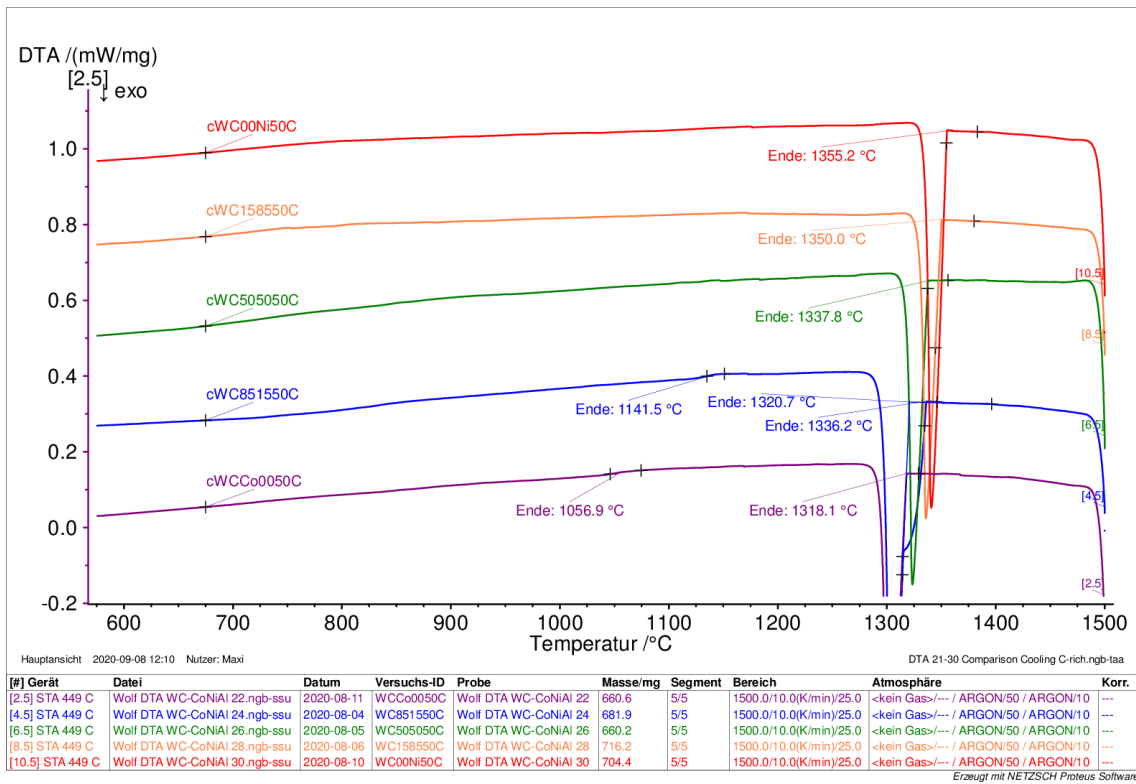
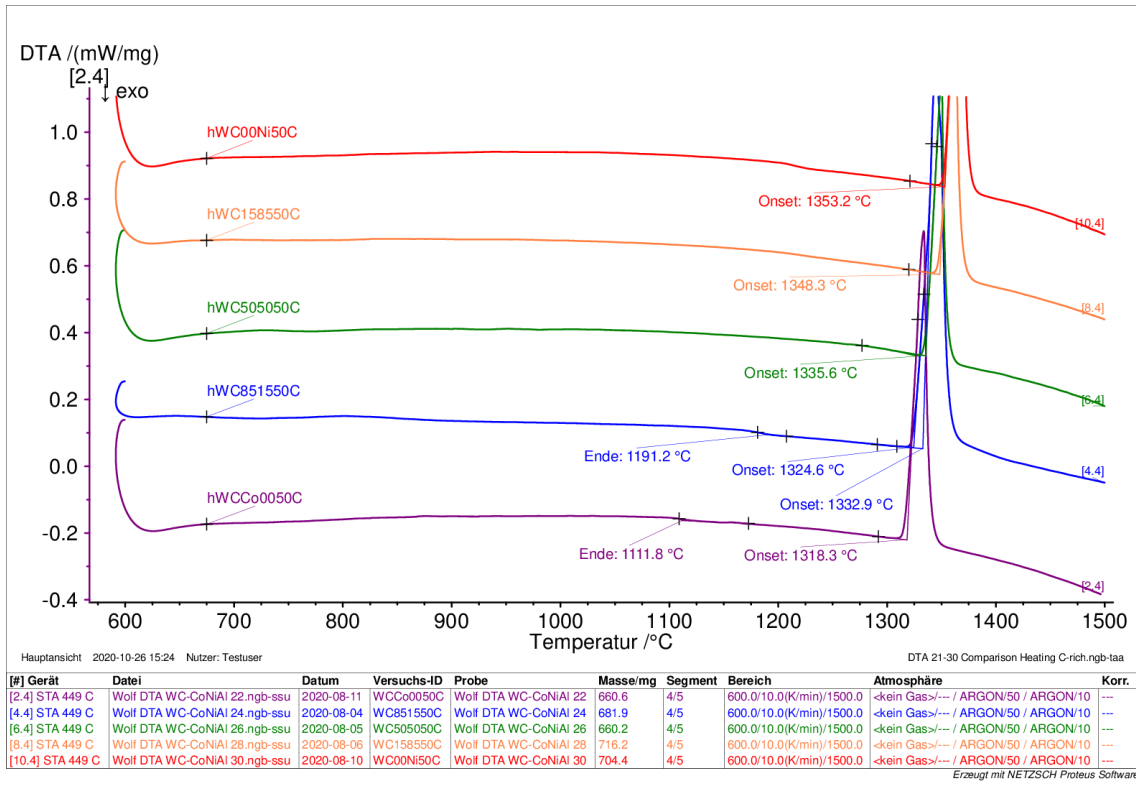
Die approbierte gedruckte Originalversion dieser Diplomarbeit ist an der TU Wien Bibliothek verfügbar. The approved original version of this thesis is available in print at TU Wien Bibliothek.



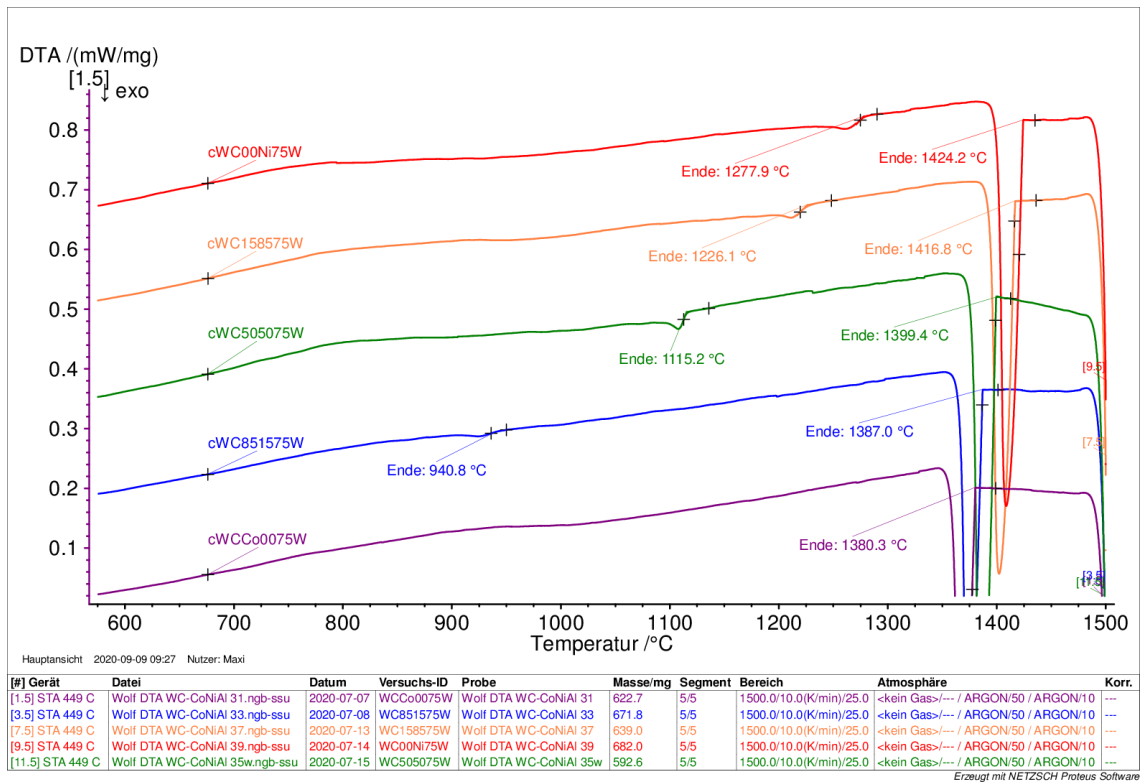
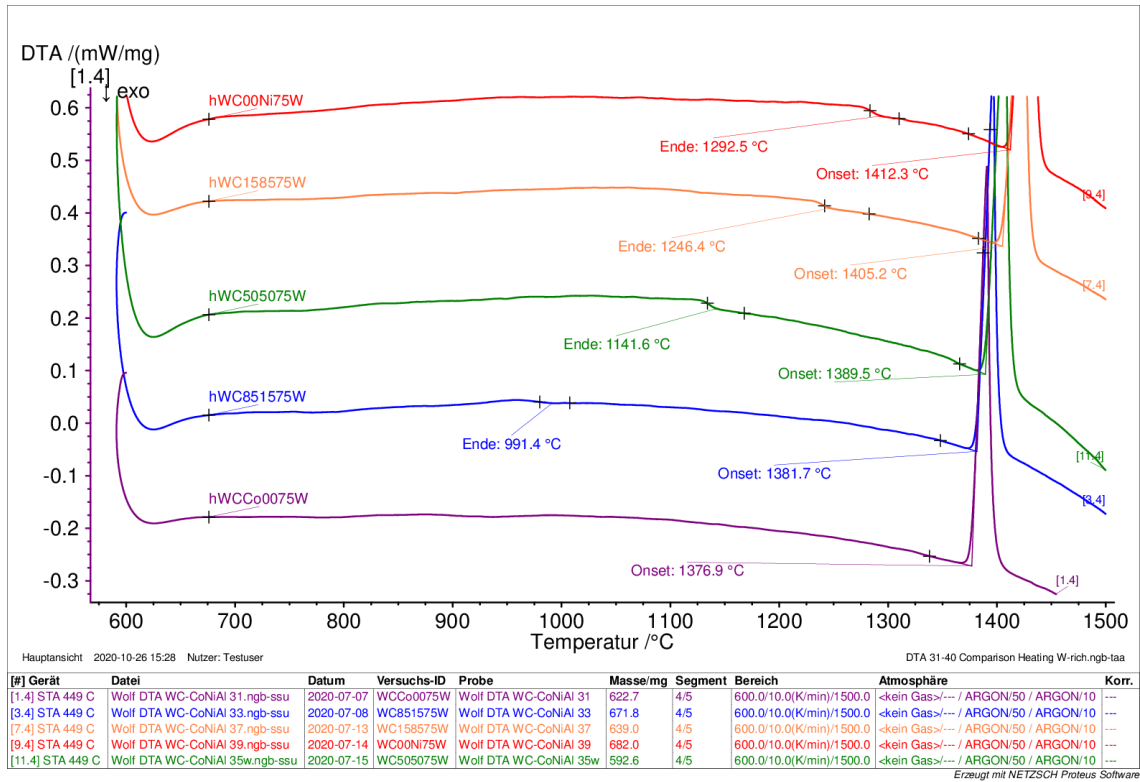
Die approbierte gedruckte Originalversion dieser Diplomarbeit ist an der TU Wien Bibliothek verfügbar. The approved original version of this thesis is available in print at TU Wien Bibliothek.

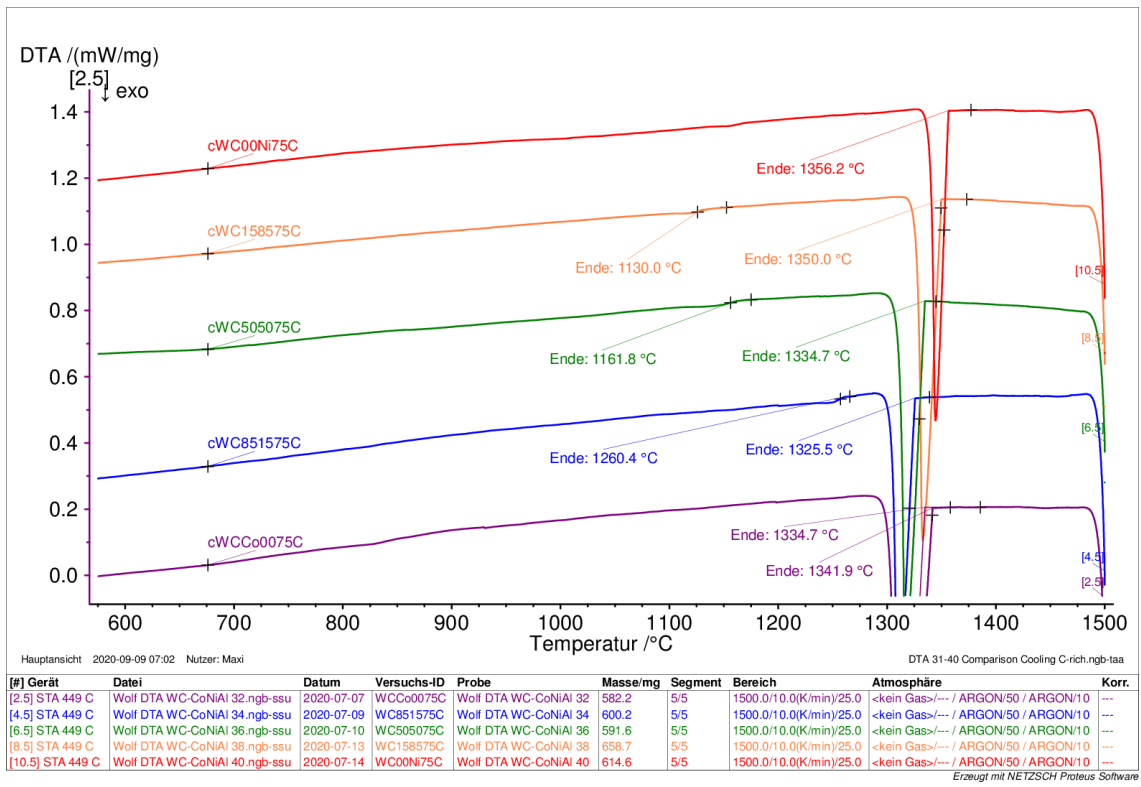
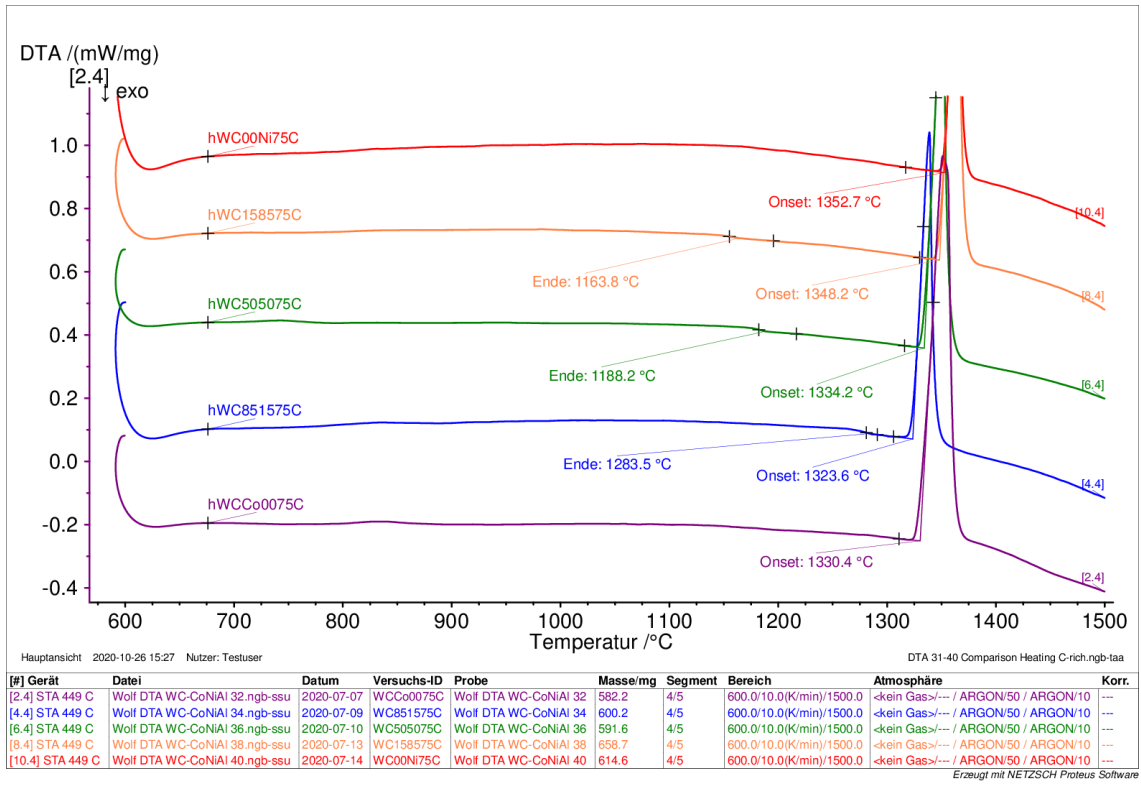


Die approbierte gedruckte Originalversion dieser Diplomarbeit ist an der TU Wien Bibliothek verfügbar. The approved original version of this thesis is available in print at TU Wien Bibliothek.

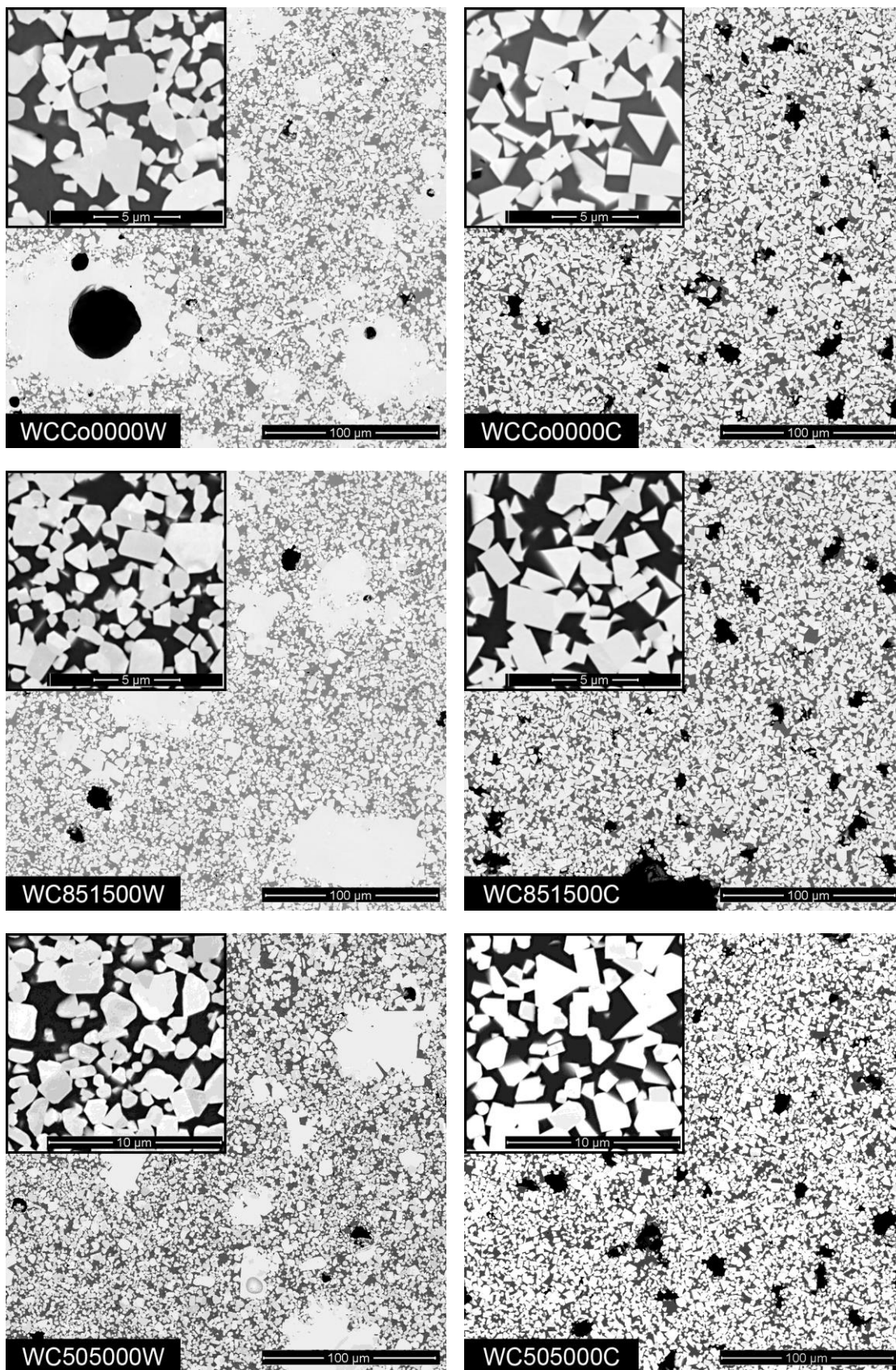


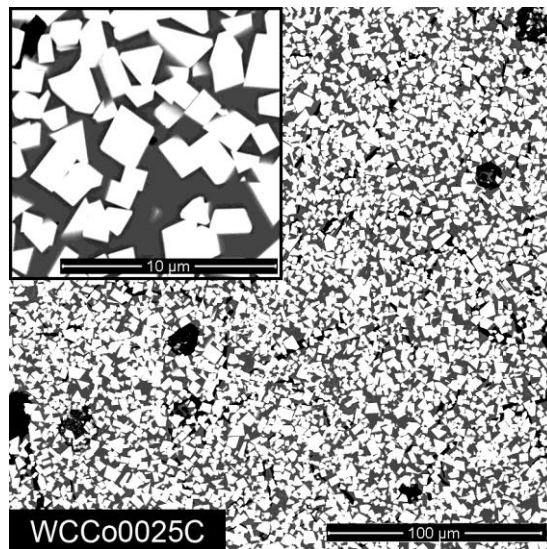
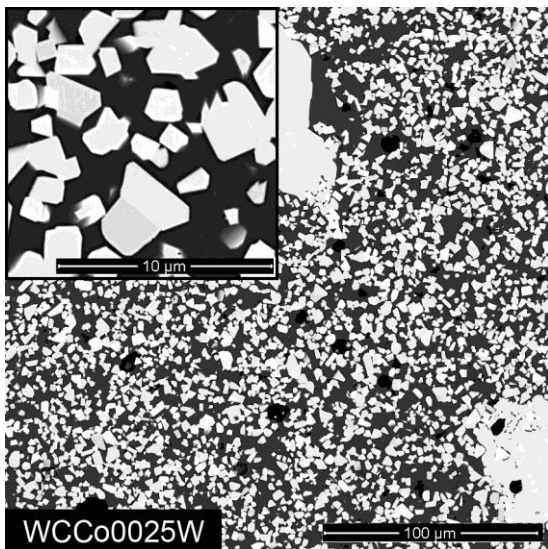
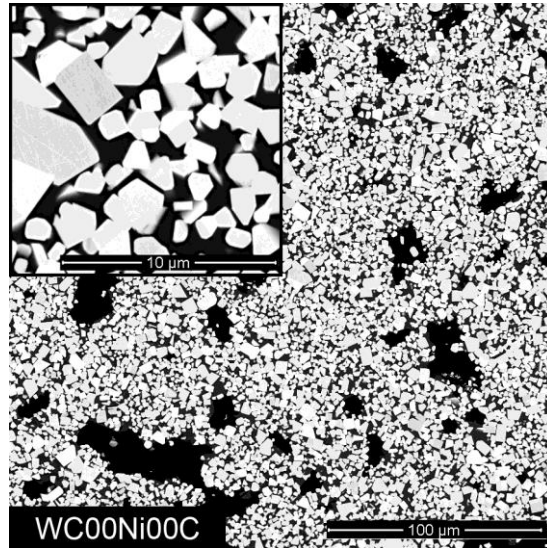
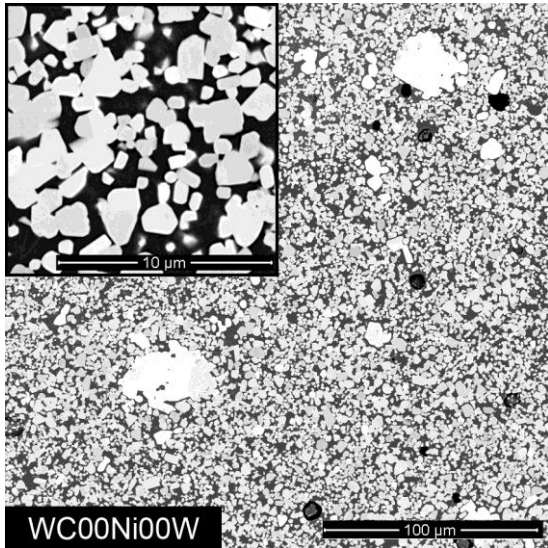
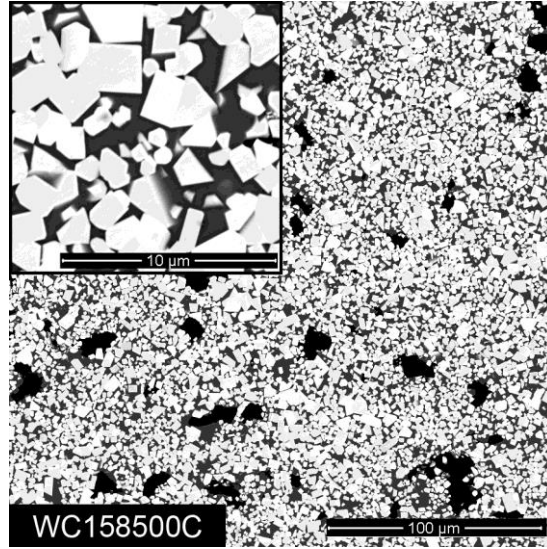
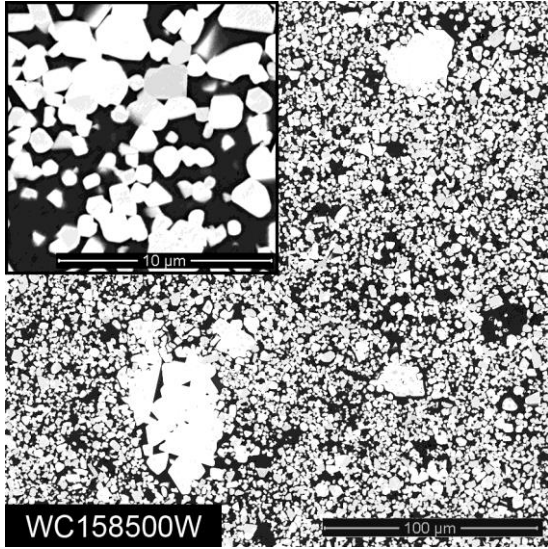
Die approbierte gedruckte Originalversion dieser Diplomarbeit ist an der TU Wien Bibliothek verfügbar. The approved original version of this thesis is available in print at TU Wien Bibliothek.

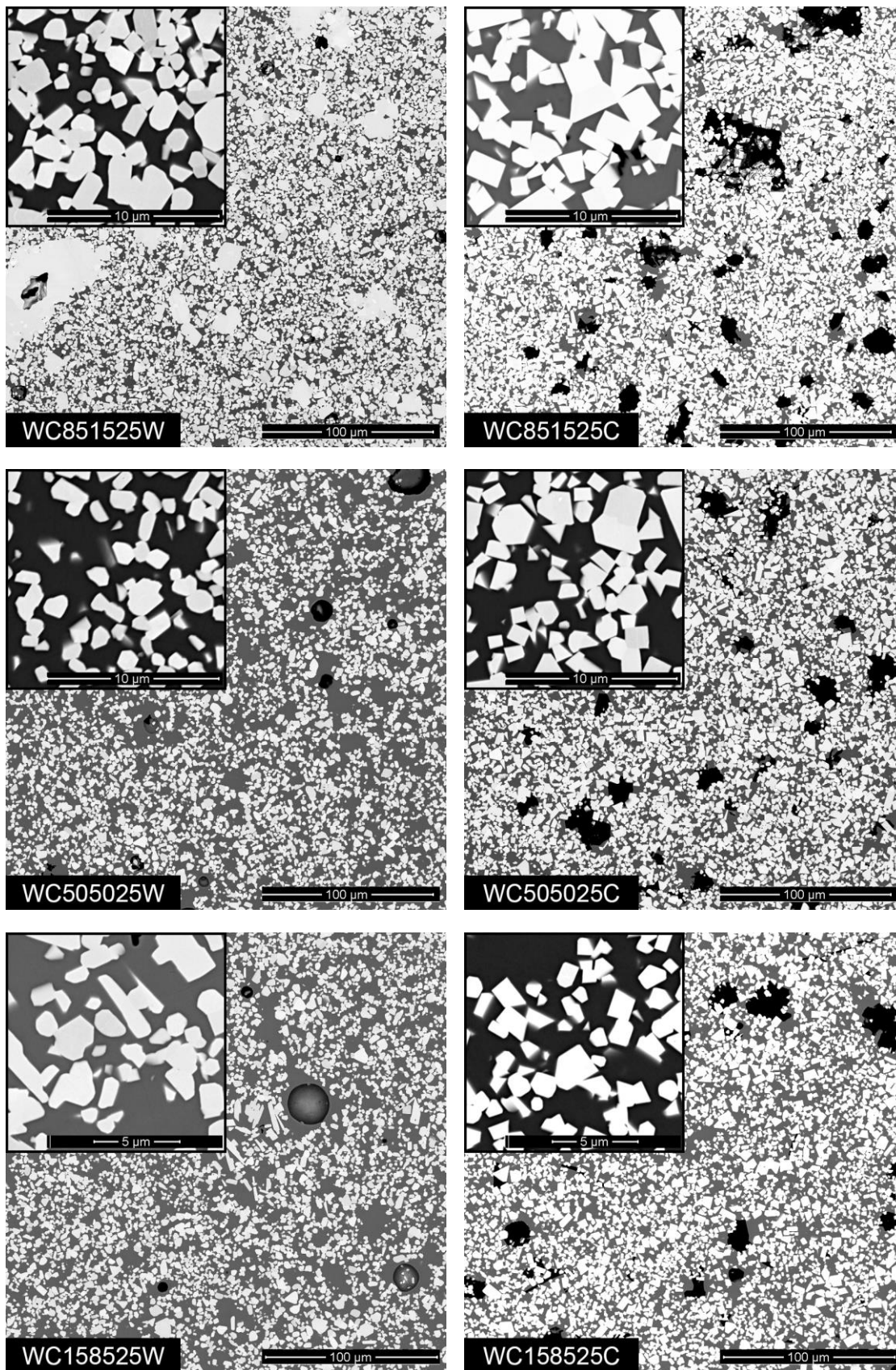




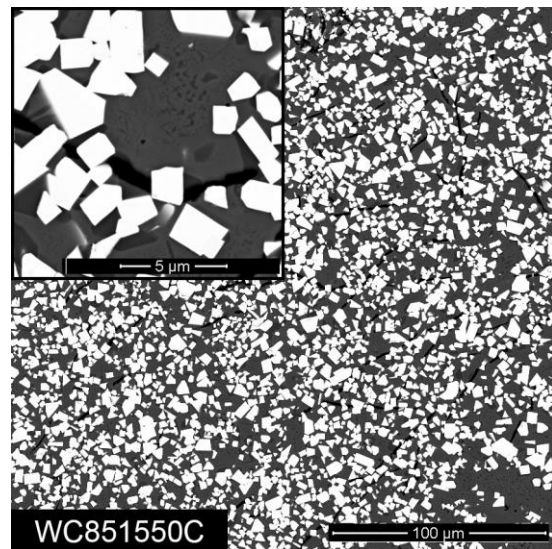
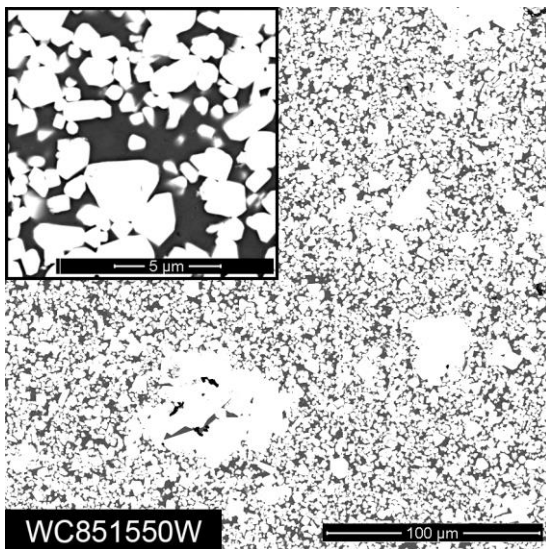
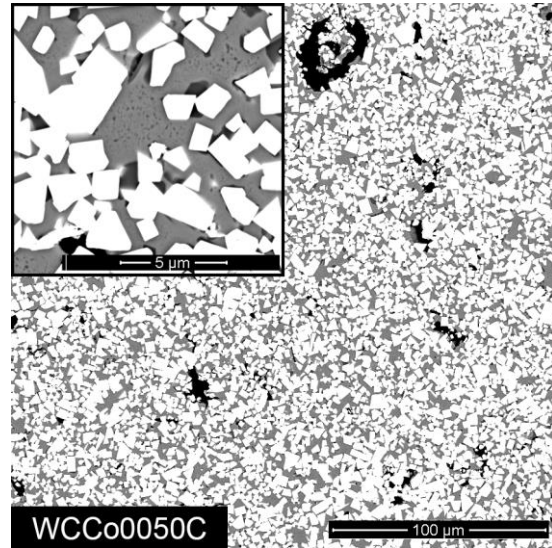
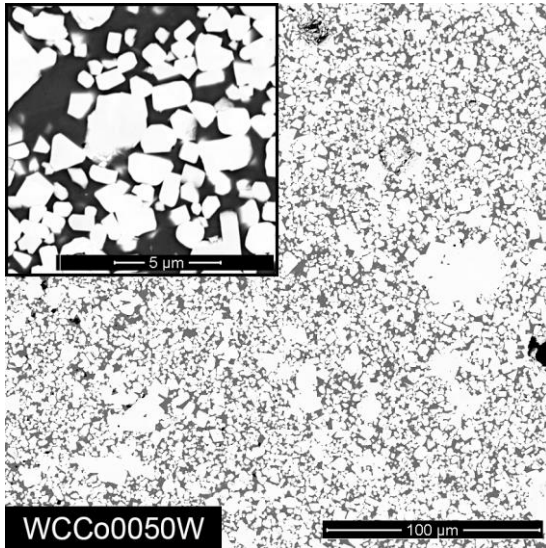
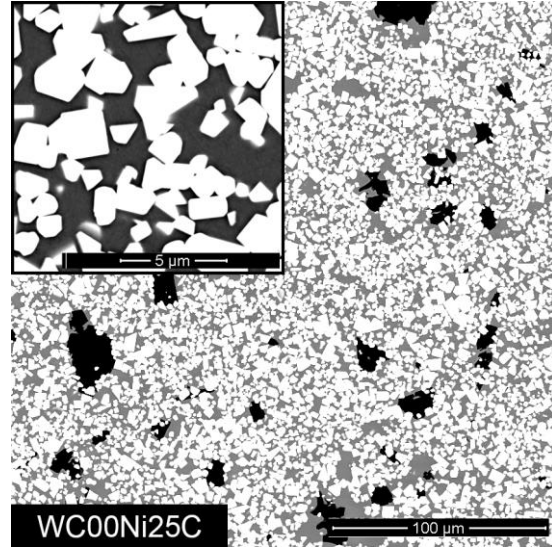
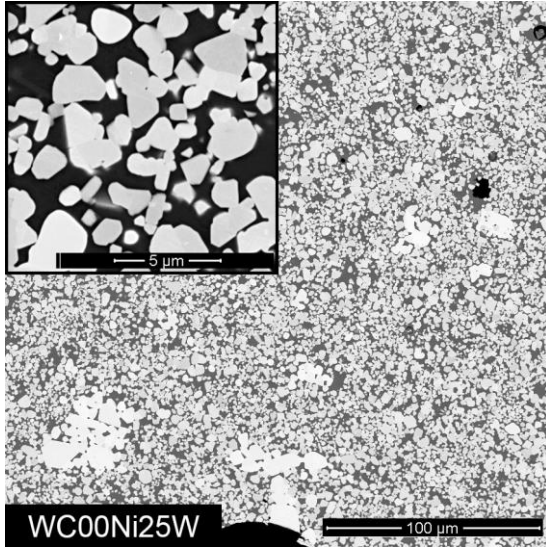
6.1.3 Microstructure

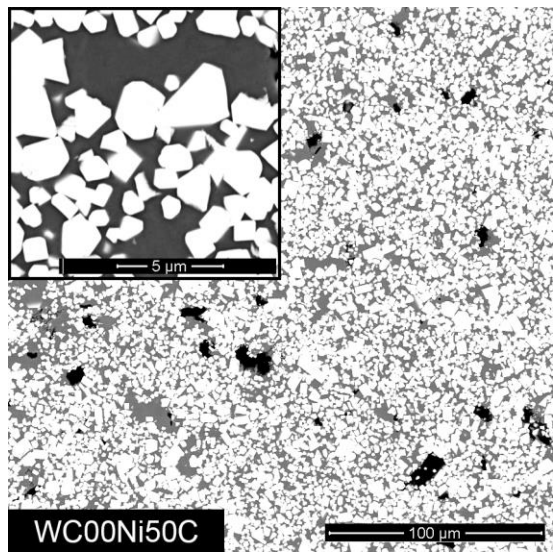
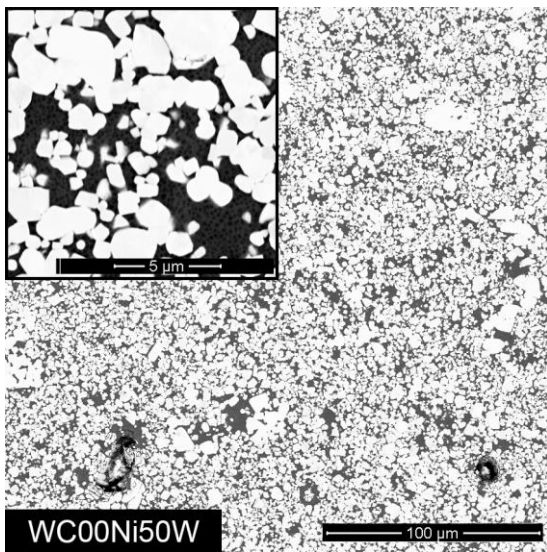
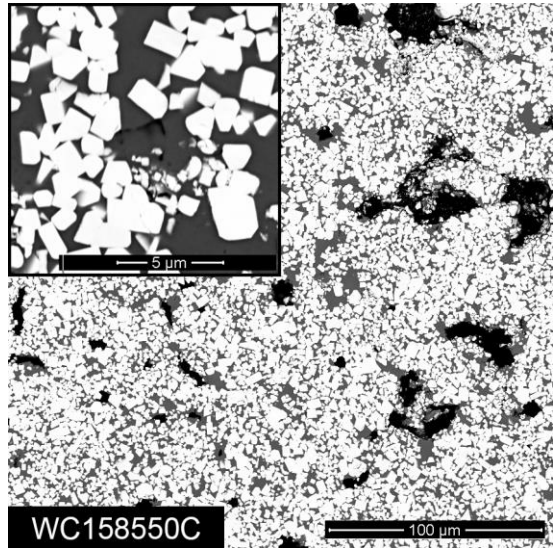
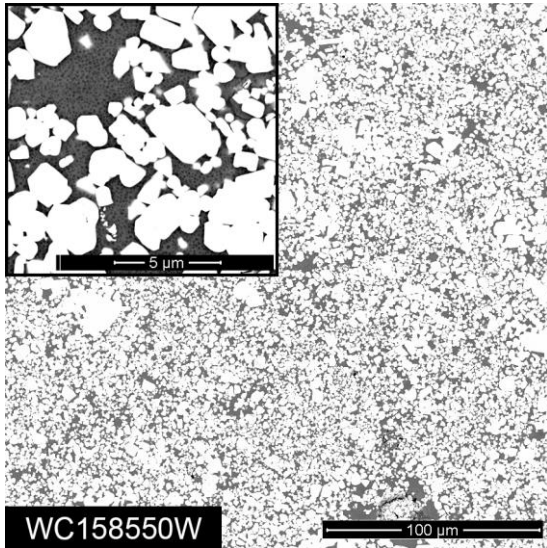
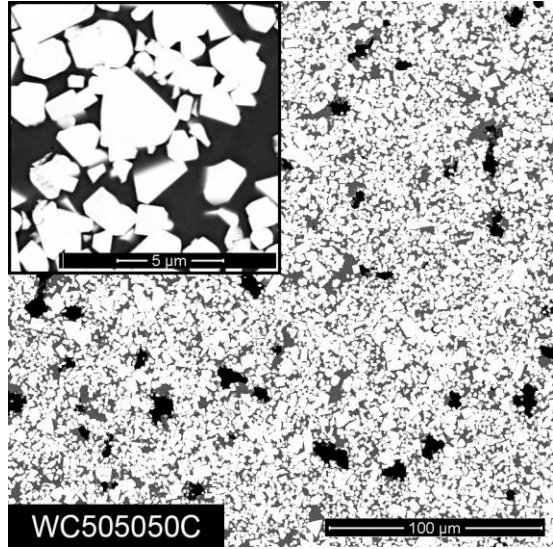
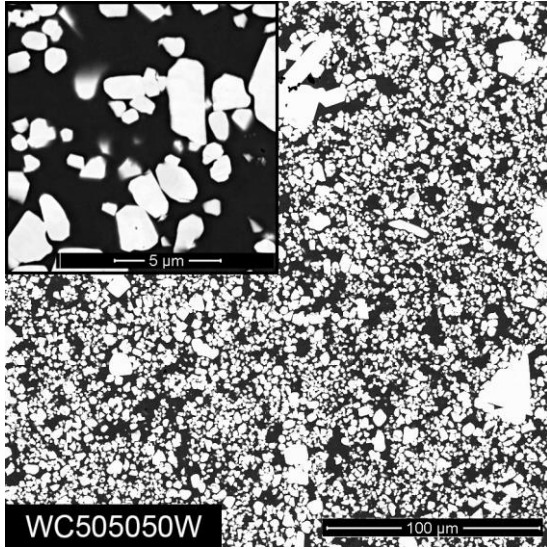


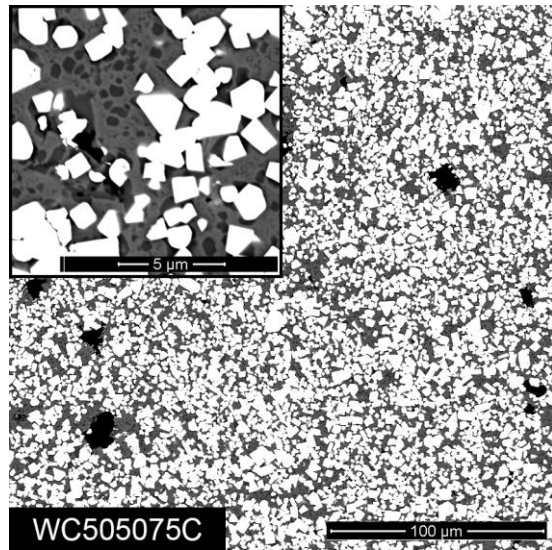
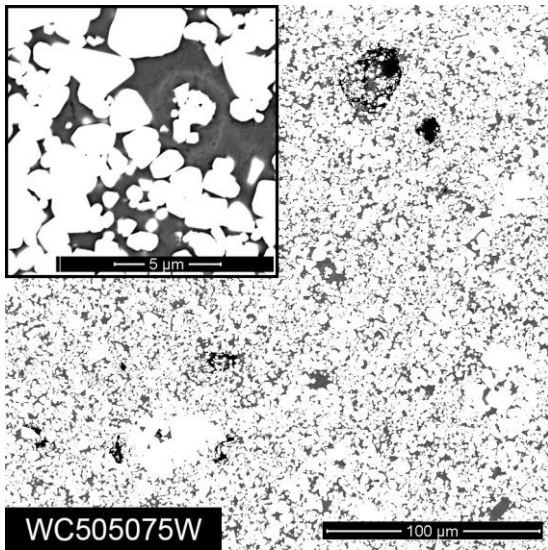
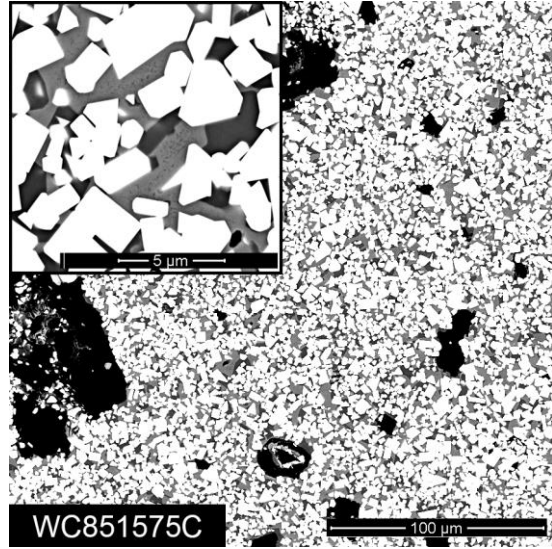
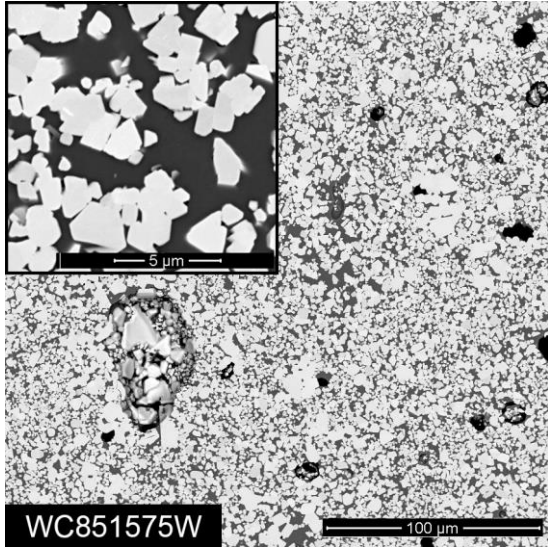
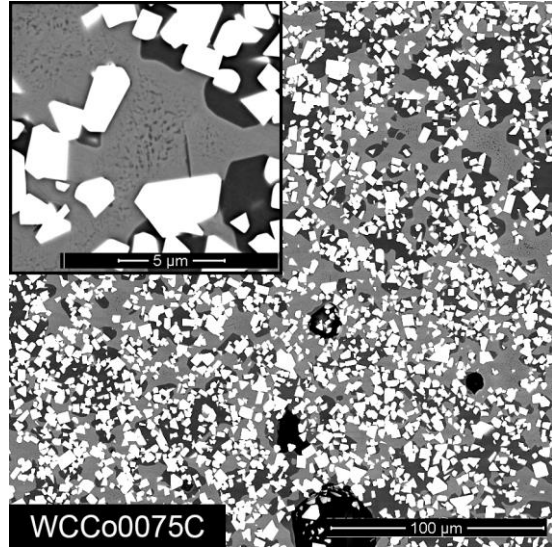
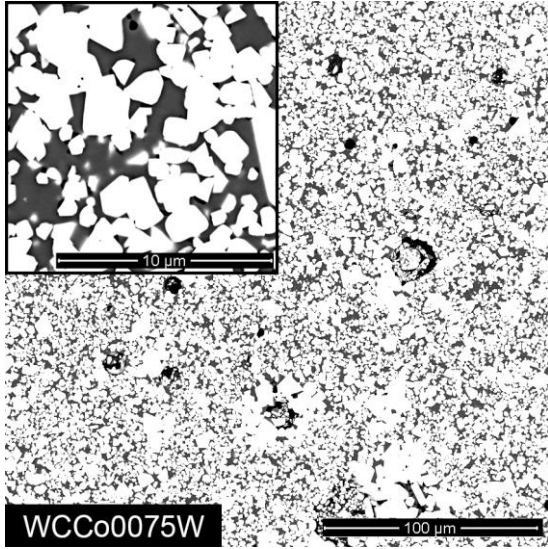


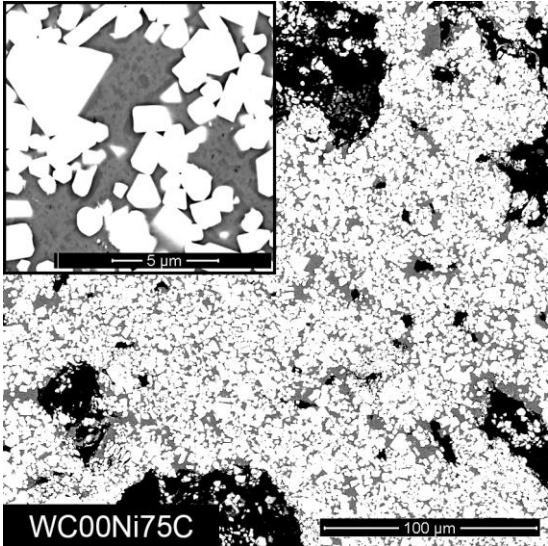
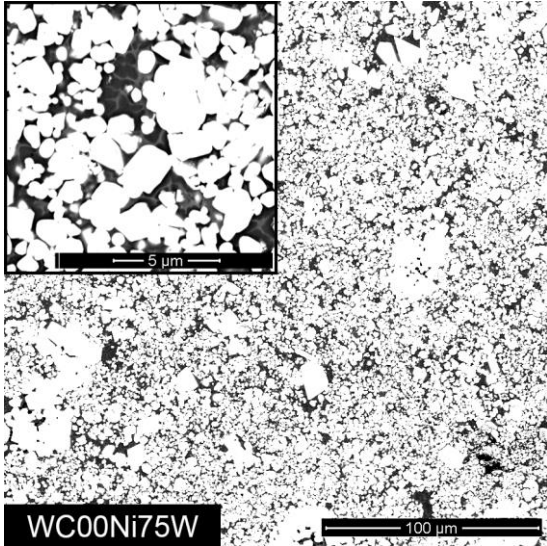
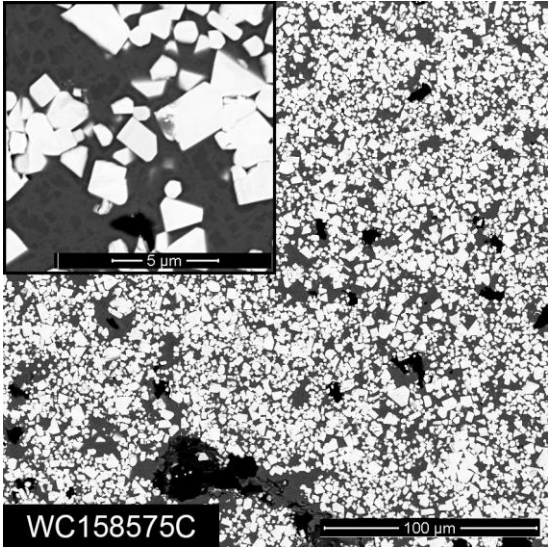
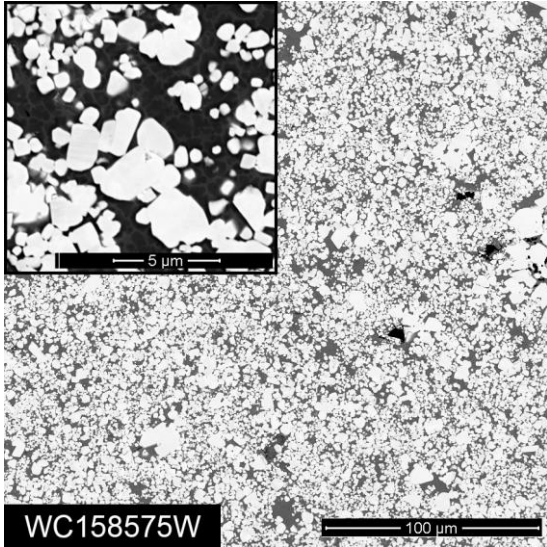


Die approbierte gedruckte Originalversion dieser Diplomarbeit ist an der TU Wien Bibliothek verfügbar.
The approved original version of this thesis is available in print at TU Wien Bibliothek.









Die approbierte gedruckte Originalversion dieser Diplomarbeit ist an der TU Wien Bibliothek verfügbar.
The approved original version of this thesis is available in print at TU Wien Bibliothek.

6.2 Thermo-Calc Macros

This section lists some basic scripts for the calculations which were carried out using Thermo-Calc. The important commands are explained before their use.

6.2.1 γ/γ' Solvus Temperature

```
GOTO_MODULE DATA
SWITCH_DATABASE USER "Zhu14.tdb"
DEFINE_ELEMENTS Al Co Ni W
GET_DATA
GOTO_MODULE GIBBS
@@ Create a second composition set of the  $\gamma/\gamma'$  phase
@@ with Co and Ni on the first, and Al and W on the second sublattice
AMEND_PHASE_DESCRIPTION
L12
COMPOSITION_SET
2
Co Ni
Al W
VA
GOTO_MODULE POLY
@@ Remove all phases and define the equilibrium of the solvus reaction
CHANGE_STATUS PHASES *=SUS
CHANGE_STATUS PHASES L12#1=ENT 1
CHANGE_STATUS PHASES L12#2=FIX 0
SET_CONDITION P=101325 N=1 X(Al)=0.11 X(W)=0.09 X(Ni)=0.15
@@ Give initial conditions for the calculation
@@ with start from 1600 K where  $\gamma/\gamma'$  is completely disordered
@@ and set the initial constitutions manually
@@ with L12#1 completely disordered and L12#2 completely ordered
SET_ALL_START_VALUES
1600
N
Y

0.11
0.65
0.15
0.09
0.11
0.65
0.15
0.09

0
0.5
0.5
0
0.5
0
0
0.5

COMPUTE_EQUILIBRIUM
SET_INTERACTIVE
```


6.2.2 Phase Diagram using TCFE9 and Zhu14 Databases

```
GOTO_MODULE DATA
SWITCH_DATABASE TCFE9
DEFINE_ELEMENTS Co Ni Al W C
@@ Remove all phases which are defined in Zhu14 database
@@ and M12C because the calculations did not work out well with it
REJECT PHASES M12C, AL2Y_C15, AL5FE4, BCC_A2, BETA1, CENI2, CENI5, CHI_A12,
CO17Y2, CO3VV, CO5Y_D2D, COZN4_GAMMA, COZN_BETA1, CR3SI, DICTRA_FCC_A1,
FCC_A1, GAMMA, L12_FCC, LAVES_PHASE_C14, MU_PHASE, NBNI3, NI3TI, R_PHASE,
SIGMA, ZETA_FEZN
GET_DATA
APPEND_DATABASE USER "Zhu14.tdb"
DEFINE_ELEMENTS Co Ni Al W
@@ Remove all phases which should be used from TCFE9 database
REJECT PHASES B2, BCC_A2, FCC_A1, LIQUID, HCP_A3
GET_DATA
GOTO_MODULE POLY
SET_CONDITION W(Co)=0.11 W(Ni)=0.03 W(Al)=0.01 W(C)=0.0491 P=1E5 N=1
T=1172.15
COMPUTE_EQUILIBRIUM
SET_AXIS_VARIABLE 1 W(C) .02 .08 0.001
SET_AXIS_VARIABLE 2 T 500 2000 15
MAP
POST
SET_DIAGRAM_AXIS X WEIGHT-PERCENT C
SET_DIAGRAM_AXIS Y TEMPERATURE-CELSIUS
SET_PLOT_OPTIONS N N N N Y 0 .1 N N N N
SET_SCALING_STATUS X N 4 6
SET_SCALING_STATUS Y N 800 1700
PLOT
SET_INTERACTIVE
```

6.2.3 Solidus Temperature VS Aluminum Concentration

```
GOTO_MODULE DATA
SWITCH_DATABASE TCFE9
DEFINE_ELEMENTS Co Ni Al W C
GET_DATA
GOTO_MODULE POLY
SET_CONDITION W(W)=0.7577 W(C)=0.0423 W(Al)=0.0001 W(Ni)=0.0001 P=1E5 N=1
SET_CONDITION T=1000
COMPUTE_EQUILIBRIUM
SET_CONDITION T=NONE
@@ Only the four phases from the invariant equilibrium are preserved
CHANGE_STATUS PHASES *=SUSPENDED
CHANGE_STATUS PHASES MC_SHP,FCC_A1,M6C=ENT 1
CHANGE_STATUS PHASES LIQUID=FIXED 0
COMPUTE_EQUILIBRIUM
@@ Define an independent axis for 1D calculations (STEP)
SET_AXIS_VARIABLE 1 W(Al) 0 0.02 0.0005
STEP NORMAL
POST
SET_DIAGRAM_AXIS X W(Al)
SET_DIAGRAM_AXIS Y TEMPERATURE-CELSIUS
PLOT
@@ Save calculation results to output file
LIST_DATA_TABLE FILE OutputFile.xls
SET_INTERACTIVE
```

6.2.4 Calculation of a Ternary Diagram

```
GOTO_MODULE SYSTEM
SET_TC_OPTIONS Y 0 Y
GOTO_MODULE DATA
SWITCH_DATABASE USER "../Zhu_TCFE9.tdb"
DEFINE_ELEMENTS Co Ni Al W
GET_DATA
GOTO_MODULE POLY
SET_CONDITION X(Al)=0.11 X(W)=0.09 P=1E5 N=1
SET_CONDITION W(Ni)=0.15
SET_CONDITION T=1223.15
COMPUTE_EQUILIBRIUM
SET_CONDITION X(Al)=NONE
SET_CONDITION X(W)=NONE
@@ Define two independent axis for 2D calculations (MAP)
SET_AXIS_VARIABLE 1 X(Al) 0 0.3 0.01
SET_AXIS_VARIABLE 2 X(W) 0 0.3 0.01
MAP
POST
@@ Save the calculation results to an experimental datafile
@@ which can be edited manually to add experimental data
@@ and drawn afterwards without recalculation
MAKE_EXPERIMENTAL_DATAFI FILE "ExperimentalDatafile.exp"
SET_INTERACTIVE
```

6.2.5 Draw a Ternary Diagram with Experimental Data

```
@@ Macro for the actual drawing process
GO POLY
POST
SET_PLOT_OPTIONS N N N N Y 0 .1 N N N N
SET_AXIS_TEXT_STATUS X N Mole Percent W
SET_SCALING_STATUS X N 0 30
SET_AXIS_TEXT_STATUS Y N Mole Percent Al
SET_SCALING_STATUS Y N 0 30
SET_DIAGRAM_TYPE YES
@@ Draw the datafiles 1, 11 and 101
@@ from the prolog 1 in the experimental datafile
APPEND_EXPERIMENTAL_DATA Y "ExperimentalDatafile.exp" 1; 1,11,101;
PLOT
SET_INTERACTIVE

@@ Excerpt of ExperimentalDatafile.exp
PROLOG 1
XSCALE      0      25
YSCALE      0      25
XTYPE LINEAR
YTYPE LINEAR
XLENGTH     11.5000
YLENGTH     11.5000
TITLE
XTEXT Mole Percent W
YTEXT Mole Percent Al
DATASET 1 Legend
SYMBOLSIZE 0.4
CLIP OFF
COLOR 2
CHAR 0.6
STRING GAMMA \latex \gamma
STRING GAMMA_PR \latex \gamma'
STRING KAPPA \latex \kappa
11.5 12.5 MVAS1'~GAMMA
```

```

11.5 12.0 MVAS2'~GAMMA+~GAMMA_PR
11.5 11.5 MVAS3'~GAMMA+~K

DATASET 11 Experimental Data
SYMBOLSIZE 0.4
CLIP OFF
CHAR 0.25
COLOR 2
BLOCK X=C1; Y=C2; GOC=C3,WAMS1;
1.70688      0
8.97163      0
1.45656      3.55412
7.60637      2.16805
1.829        9.46642      S3
6.57781      8.54388
1.5399       12.3534      S3
4.74158      11.87744
BLOCKEND

DATASET 101 Calculated Phase Diagram
LINETYPE 0
CHAR 0.25
COLOR 1
$ BLOCK #66 1 FOR:
$F0 B2
$E L12#1
BLOCK X=C1; Y=C2; GOC=C3,WAD;
$ PLOTTED COLUMNS ARE : X(W)*100.0 and X(AL)*100.0
  1.0000000000E+00  1.1462706106E+01  M
  9.9900000000E-01  1.1462967971E+01
  4.9950000000E-01  1.1592483619E+01
  1.0000000000E-10  1.1719167402E+01
  1.0000000000E-10  1.1719170335E+01
  1.0000000000E-10  1.1719175160E+01
  1.0000000000E-10  1.1719175160E+01
BLOCKEND
$ BLOCK #141 1 FOR:
$F0 B2
$E L12#1
$E L12#2
BLOCK X=C1; Y=C2; GOC=C3,WAD;
$ PLOTTED COLUMNS ARE : X(W)*100.0 and X(AL)*100.0
  5.7173986915E+00  1.0157397063E+01  M
  5.7183986915E+00  1.0157893408E+01
  6.7173986915E+00  1.0639850959E+01
  7.7173986915E+00  1.1097569709E+01
...

```

6.3 References

1. Konyashin, I., et al., *Strengthening zones in the Co matrix of WC–Co cemented carbides*. Scripta Materialia, 2014. **83**: p. 17-20.
2. Shinagawa, K., et al., *Phase Equilibria and Microstructure on γ ' Phase in Co–Ni–Al–W System*. Materials Transactions, 2008. **49**(6): p. 1474-1479.
3. Ortner, H.M., P. Ettmayer, and H. Kolaska, *The history of the technological progress of hardmetals*. International Journal of Refractory Metals and Hard Materials, 2014. **44**: p. 148-159.
4. Upadhyaya, G.S., *Cemented tungsten carbides: production, properties and testing*. 1998: William Andrew.
5. García, J., et al., *Cemented carbide microstructures: a review*. International Journal of Refractory Metals and Hard Materials, 2019. **80**: p. 40-68.
6. Nishigaki, K., et al. *Binder Phase Strengthening Through γ ' Precipitation of WC–Co–Ni–Cr–Al Hard Alloys*. in *11 th International Plansee Seminar'85*. 1985.
7. Long, J., et al., *A new type of WC–Co–Ni–Al cemented carbide: Grain size and morphology of γ '-strengthened composite binder phase*. Scripta Materialia, 2017. **126**: p. 33-36.
8. Sims, C.T., *A history of superalloy metallurgy for superalloy metallurgists*. Superalloys, 1984. **1984**: p. 399-419.
9. Sato, J., et al., *Cobalt-Base High-Temperature Alloys*. Science, 2006. **312**(5770): p. 90.
10. Freund, L.P., et al., *Formation of Cuboidal Co₃AlC Precipitates in Carbon-Containing Co–Al–W-Based Superalloys*. Advanced Engineering Materials, 2015. **17**(8): p. 1113-1118.
11. Lass, E.A., R.D. Grist, and M.E. Williams, *Phase Equilibria and Microstructural Evolution in Ternary Co–Al–W Between 750 and 1100 °C*. Journal of Phase Equilibria and Diffusion, 2016. **37**(4): p. 387-401.
12. Zhu, J., M.S. Titus, and T.M. Pollock, *Experimental Investigation and Thermodynamic Modeling of the Co-Rich Region in the Co–Al–Ni–W Quaternary System*. Journal of Phase Equilibria and Diffusion, 2014. **35**(5): p. 595-611.
13. Liu, X.L., et al., *Thermodynamic modeling of Al–Co–Cr, Al–Co–Ni, Co–Cr–Ni ternary systems towards a description for Al–Co–Cr–Ni*. Calphad, 2016. **52**: p. 125-142.
14. Dinçer, O., et al., *Processing and microstructural characterization of liquid phase sintered tungsten–nickel–cobalt heavy alloys*. International Journal of Refractory Metals and Hard Materials, 2015. **50**: p. 106-112.
15. Wang, Y., et al., *A thermodynamic description of the Al–Co–Ni system and site occupancy in Co + AlNi₃ composite binder phase*. Journal of Alloys and Compounds, 2016. **687**: p. 855-866.
16. Stein, F., C. He, and N. Dupin, *Melting behaviour and homogeneity range of B2 CoAl and updated thermodynamic description of the Al–Co system*. Intermetallics, 2013. **39**: p. 58-68.
17. Ansara, I., et al., *Thermodynamic assessment of the Al–Ni system*. Journal of Alloys and Compounds, 1997. **247**(1): p. 20-30.
18. Zheng, W., et al., *Thermodynamic Evaluation of the Co–Al–C System by Coupling Ab Initio Calculations and CALPHAD Approach*. Journal of Phase Equilibria and Diffusion, 2018. **39**(5): p. 538-548.
19. Ohtani, H., M. Yamano, and M. Hasebe, *Thermodynamic analysis of the Co–Al–C and Ni–Al–C systems by incorporating ab initio energetic calculations into the CALPHAD approach*. Calphad, 2004. **28**(2): p. 177-190.
20. Guillermet, A.F., *Thermodynamic Properties of the Fe–Co–Ni–C System*. Zeitschrift für Metallkunde, 1988. **79**: p. 524-536.
21. Gröbner, J., H.L. Lukas, and F. Aldinger, *Thermodynamic calculations in the Y–Al–C system*. Journal of Alloys and Compounds, 1995. **220**(1): p. 8-14.

22. Wang, Y., et al., *Phase equilibria in the Al–C–Ni–W quaternary system*. International Journal of Refractory Metals and Hard Materials, 2014. **46**: p. 43-51.
23. Hosoda, H. and T. Inamura, *Evaluation of Solubility Limit of Carbon in Ni₃AlC_{1-x}*. MRS Proceedings, 2011. **1295**: p. mrsf10-1295-n02-09.
24. Guillermet, A.F., *Thermodynamic properties of the Co–W–C system*. Metallurgical Transactions A, 1989. **20**(5): p. 935-956.
25. Guillermet, A., *The Co–Fe–Ni–W–C Phase Diagram: A Thermodynamic Description and Calculated Sections for (Co–Fe–Ni)-Bonded Cemented WC Tools*. Zeitschrift für Metallkunde, 1989. **80**: p. 83-94.
26. Zhou, P., et al., *Experimental investigation and thermodynamic assessment of the C–Co–Fe–Ni–W system*. International Journal of Refractory Metals and Hard Materials, 2016. **54**: p. 60-69.
27. Kaufman, L. and H. Bernstein, *Computer calculation of phase diagrams. With special reference to refractory metals*. 1970.
28. Kattner, U.R., *The Calphad method and its role in material and process development*. Tecnologia em metalurgia, materiais e mineracao, 2016. **13**(1): p. 3.
29. Liu, Z.-K. and Y. Wang, *Computational thermodynamics of materials*. 2016: Cambridge University Press.
30. Lukas, H., S.G. Fries, and B. Sundman, *Computational thermodynamics: the Calphad method*. 2007: Cambridge university press.
31. Dinsdale, A.T., *SGTE data for pure elements*. Calphad, 1991. **15**(4): p. 317-425.
32. Connetable, D., et al., *A Calphad assessment of Al–C–Fe system with the carbide modelled as an ordered form of the fcc phase*. Calphad, 2008. **32**(2): p. 361-370.
33. Wang, P., et al., *Thermodynamic re-assessment of the Al–Co–W system*. Calphad, 2017. **59**: p. 112-130.
34. Dupin, N., I. Ansara, and B. Sundman, *Thermodynamic re-assessment of the ternary system Al–Cr–Ni*. Calphad, 2001. **25**(2): p. 279-298.
35. Lee, B.-J., *On the stability of Cr carbides*. Calphad, 1992. **16**(2): p. 121-149.
36. Jonsson, S., *Phase relations in quaternary hard materials*. 1995.
37. Guillermet, A.F., *Assessment of the Thermodynamic Properties of the Ni–Co System*. Zeitschrift für Metallkunde, 1987. **78**: p. 639-647.
38. Markström, A., K. Frisk, and B. Sundman, *A revised thermodynamic description of the Co–W–C system*. Journal of Phase Equilibria and Diffusion, 2005. **26**(2): p. 152-160.
39. Gustafson, P., *A thermodynamic evaluation of the Cr–Ni–W system*. Calphad, 1988. **12**(3): p. 277-292.
40. Popovič, J., P. Brož, and J. Buršik, *Microstructure and phase equilibria in the Ni–Al–W system*. Intermetallics, 2008. **16**(7): p. 884-888.
41. Goldstein, J.I., et al., *Scanning electron microscopy and X-ray microanalysis*. 2017: Springer.
42. *TCS Cemented Carbide Database 1.0*. 2015, Thermo-Calc Software AB.
43. *TCS Steels and Fe-alloys Database 9.1*. 2019, Thermo-Calc Software AB.
44. Bauer, A., et al., *Microstructure and creep strength of different γ/γ' -strengthened Co-base superalloy variants*. Scripta Materialia, 2010. **63**(12): p. 1197-1200.
45. Tanaka, K., et al., *Creep deformation of single crystals of new Co–Al–W-based alloys with fcc/L12two-phase microstructures*. Philosophical Magazine, 2012. **92**(32): p. 4011-4027.
46. Titus, M.S., A. Suzuki, and T.M. Pollock, *Creep and directional coarsening in single crystals of new γ – γ' cobalt-base alloys*. Scripta Materialia, 2012. **66**(8): p. 574-577.
47. Blöchl, P.E., *Projector augmented-wave method*. Physical Review B, 1994. **50**(24): p. 17953-17979.
48. Kresse, G. and D. Joubert, *From ultrasoft pseudopotentials to the projector augmented-wave method*. Physical Review B, 1999. **59**(3): p. 1758-1775.

49. Gonze, X., et al., *The Abinitproject: Impact, environment and recent developments*. Computer Physics Communications, 2020. **248**.
50. Romero, A.H., et al., *ABINIT: Overview and focus on selected capabilities*. J Chem Phys, 2020. **152**(12): p. 124102.
51. Torrent, M., et al., *Implementation of the projector augmented-wave method in the ABINIT code: Application to the study of iron under pressure*. Computational Materials Science, 2008. **42**(2): p. 337-351.
52. Perdew, J.P., K. Burke, and M. Ernzerhof, *Generalized Gradient Approximation Made Simple*. Physical Review Letters, 1996. **77**(18): p. 3865-3868.
53. Jollet, F., M. Torrent, and N. Holzwarth, *Generation of Projector Augmented-Wave atomic data: A 71 element validated table in the XML format*. Computer Physics Communications, 2014. **185**(4): p. 1246-1254.
54. Head, J.D. and M.C. Zerner, *A Broyden—Fletcher—Goldfarb—Shanno optimization procedure for molecular geometries*. Chemical Physics Letters, 1985. **122**(3): p. 264-270.
55. Monkhorst, H.J. and J.D. Pack, *Special points for Brillouin-zone integrations*. Physical Review B, 1976. **13**(12): p. 5188-5192.
56. Methfessel, M. and A.T. Paxton, *High-precision sampling for Brillouin-zone integration in metals*. Physical Review B, 1989. **40**(6): p. 3616-3621.
57. Kobayashi, S., et al., *Determination of phase equilibria in the Co-rich Co–Al–W ternary system with a diffusion-couple technique*. Intermetallics, 2009. **17**(12): p. 1085-1089.
58. Zhou, C., et al., *Thermodynamic description of the Co–Ni–Ta system*. Calphad, 2019. **66**: p. 101649.
59. Shi, L., et al., *Effect of Ta additions on microstructure and mechanical properties of a single-crystal Co–Al–W-base alloy*. Materials Letters, 2015. **149**: p. 58-61.
60. Ooshima, M., et al., *Effects of quaternary alloying elements on the γ' solvus temperature of Co–Al–W based alloys with fcc/L12 two-phase microstructures*. Journal of Alloys and Compounds, 2010. **508**(1): p. 71-78.
61. Pollock, C. and H. Stadelmaier, *The eta carbides in the Fe–W–C and Co–W–C systems*. Metallurgical Transactions, 1970. **1**(4): p. 767-770.
62. Tracey, V.A., *Nickel in hardmetals*. International Journal of Refractory Metals and Hard Materials, 1992. **11**(3): p. 137-149.
63. Ishida, K. and T. Nishizawa, *The C-Co (carbon-cobalt) system*. Journal of phase equilibria, 1991. **12**(4): p. 417-424.
64. Singleton, M. and P. Nash, *The C-Ni (carbon-nickel) system*. Bulletin of Alloy Phase Diagrams, 1989. **10**(2): p. 121-126.
65. Ding, E.Y., *Study on Separation Method of Overlapped Peaks in Differential Thermal Analysis with Computer Simulation*. Journal of Thermal Analysis and Calorimetry - J THERM ANAL CALORIM, 2000. **63**: p. 517-523.
66. Gabriel, A., et al., *New experimental data in the C-Fe-W, C-Co-W, C-Ni-W, C-Fe-Ni-W and C-Co-Ni-W cemented carbides systems and their application to sintering conditions*. International journal of refractory & hard metals, 1986. **5**(4): p. 215-221.
67. Riley, D., *Lattice constant of diamond and the C–C single bond*. Nature, 1944. **153**(3889): p. 587-588.
68. Davey, W.P., *Precision Measurements of the Lattice Constants of Twelve Common Metals*. Physical Review, 1925. **25**(6): p. 753-761.
69. Vincent, F. and M. Figlarz, *Quelques precisions sur les parametres cristallins et lintensite des raies debye-scherrer du cobalt cubique et du cobalt hexagonal*. Comptes Rendus Hebdomadaires des Seances de L Academie des Sciences Serie C, 1967. **264**(15): p. 1270-&.
70. Chen, H.L., et al., *Thermodynamics of the Al₃Ni phase and revision of the Al–Ni system*. Thermochemica Acta, 2011. **512**(1-2): p. 189-195.

71. Bradley, A.J. and A. Taylor, *XCIX. The crystal structures of Ni₂Al₃ and NiAl₃*. The London, Edinburgh, and Dublin Philosophical Magazine and Journal of Science, 1937. **23**(158): p. 1049-1067.
72. Ellner, M., S. Kek, and B. Predel, *Zur Existenz einer Phase Co₃Al vom Cu₃Au-Strukturtyp*. Journal of Alloys and Compounds, 1992. **189**(2): p. 245-248.
73. Jia, C., K. Ishida, and T. Nishizawa, *Partition of alloying elements between γ (A1), γ' (L1 2), and β (B2) phases in Ni-Al base systems*. Metallurgical and Materials Transactions A, 1994. **25**(3): p. 473-485.
74. Kimura, Y., et al., *Compressive mechanical properties of multi-phase alloys based on B2 CoAl and E21 Co₃AlC*. Intermetallics, 2000. **8**(7): p. 749-757.
75. Kimura, Y., K. Sakai, and Y. Mishima, *Revolutionary microstructure control with phase diagram evaluation for the design of E21 Co₃AlC-based heat-resistant alloys*. Journal of Phase Equilibria and Diffusion, 2006. **27**(1): p. 14-21.